the STEEL centre

DESIGN OF AXIALLY-LOADED WIDE-FLANGE COLUMNS SUBJECTED TO TORSION THROUGH ONE FLANGE

Riley Quintin

Robert G. Driver

Logan Callele

UNIVERSITY OF ALBERTA   cisc icca

External Sponsor

Steel Centre Industry Partners

Design of Axially-loaded Wide-flange Columns Subjected to Torsion Through One Flange

by

Riley Quintin
Robert G. Driver
and
Logan Callele

Steel Centre Engineering Report No. 011

Department of Civil and Environmental Engineering
University of Alberta
Edmonton, Alberta, Canada

March 2018

Abstract:

It has become common for steel fabricators to find torsional loads included in the design documents of many industrial steel structures. These loads arise in wide-flange beam-to-column moment connections when the beam is subject to weak axis bending, which in turn, is transferred to the column as torsion applied to the adjoining flange. If the wide-flange column is unstiffened at the connection, localized distortion of the web can lead to additional rotation of the connected flange that are not accounted for in classical elastic torsion theory. Due to a lack of codified guidelines or relevant literature on how to design for this behaviour, designers routinely add full-depth web stiffeners at the connection to prevent localized distortion of the member, which is costly and time consuming. Previous research has revealed some information about how the torsional moment is shared between the column web in bending and flange in torsion, but no full-scale tests considered the presence of axial load. The current study performs parametric numerical analysis studies to consider the effects of cross-sectional geometry and the deleterious effects of axial load on the strength and stiffness of the wide-flange column. Fifteen full-scale tests have been conducted to verify the findings from numerical simulations and develop a design procedure for predicting the strength and stiffness of the member. Formulations have been provided to calculate the behavior of unstiffened axially-loaded wide-flange members subjected to torsion through one flange.

ACKNOWLEDGEMENTS

Table of Contents

List of Tables

List of Figures

List of Symbols

A	:	Area
b	:	Flange width
b_{eff}	:	Effective width of web in bending
bf,c,	:	Beam flange in compression (Gil et al. 2015)
bf,t,	:	Beam flange in tension (Gil et al. 2015)
C	:	Empirical constant based on stiffness ratio between flange and web (Milner 1977)
C_1, C_2, C_3	:	Torsional constants based on member end restraint
cf,b,c	:	Column flange in bending (compression) (Gil et al. 2015)
cf,b,t	:	Column flange in bending (tension) (Gil et al. 2015)
C_w	:	Warping torsion constant
cw,b	:	Column web in bending (Gil et al. 2015)
d	:	Section depth
E	:	Young's modulus of steel
ep,b,c	:	End plate in bending (compression) (Gil et al. 2015)
ep,b,t	:	End plate in bending (tension) (Gil et al. 2015)
F_y	:	Steel yield stress
G	:	Shear modulus of steel
h	:	Vertical distance between flanges of a wide-flange member
J	:	St. Venant torsional constant
K_b	:	Bending stiffness of bracing member
K_e	:	Effective brace stiffness
K_j	:	Stiffness of joint
K_s	:	Torsional stiffness of member using classical elastic torsion theory
K_u	:	Effective rotational stiffness of flange in an unstiffened member
K_w	:	Bending stiffness of web, local web distortion stiffness
L	:	Member length
M	:	Twisting moment
M_n	:	Nominal plastic moment capacity of an unstiffened web (Dowswell 2010)

M_y	:	Initial yield moment
M_z	:	Internal torque
N	:	Connection width
P	:	Axial load
P_y	:	Axial yield force
r	:	Stiffness ratio by Milner (1977)
r_1	:	Parametric ratio of torsional stiffness of flange to bending stiffness of web
t	:	Flange thickness
w	:	Web width
W_{eff}	:	Effective width (Dowswell 2010)
z	:	Distance from ends of member to transverse section under consideration
Z_{eff}	:	Plastic modulus of web (Dowswell 2010)
α	:	Angle of twist
β_{sec}	:	Localized bending stiffness of web
ε_{33}	:	Principal longitudinal strain based on cartesian coordinate system
θ	:	Angle of rotation
λ	:	Torsional constant
ν	:	Poisson's ratio of steel
σ_{xy}	:	Stress components in von Mises equation based on cartesian coordinate system
σ_{vm}	:	Von Mises stress
ψ	:	Section depth modifier

1 Introduction

1.1 Background

Industrial structures are commonly designed using structural steel to take advantage of its strength, versatility, adaptability, and ductility under complex and often unclear loading conditions. Load cases due to wind, hydraulic events, machine operation, future repurposing, and many other common industrial loading scenarios may occur during the life of a structure. To account for this, detailed load combinations are being included in the structural analysis, including torsional loads, that often appear in combination with significant flexural forces or axial compression/tension. Wide-flange sections are often selected to resist these load combinations due to their efficacy when resisting in-plane flexural loads and cost-effective connections when used as columns. As a result, stiffeners are often included in the design to resist the torsional loads due to a lack of codified guidelines or relevant literature that predicts the unstiffened column capacity, which adds considerable time and cost to fabricate the structure.

One example where the load combinations described above may be significant is a pipe rack structure (shown in Figure 1.1), where design hydraulic events in the pipe cause weak-axis bending in the supporting beam to be transferred to the column as torsion applied to the adjoining flange. Multi-tier pipe racks mean the wide-flange columns are likely carrying significant axial load, creating the load combination in Figure 1.2.
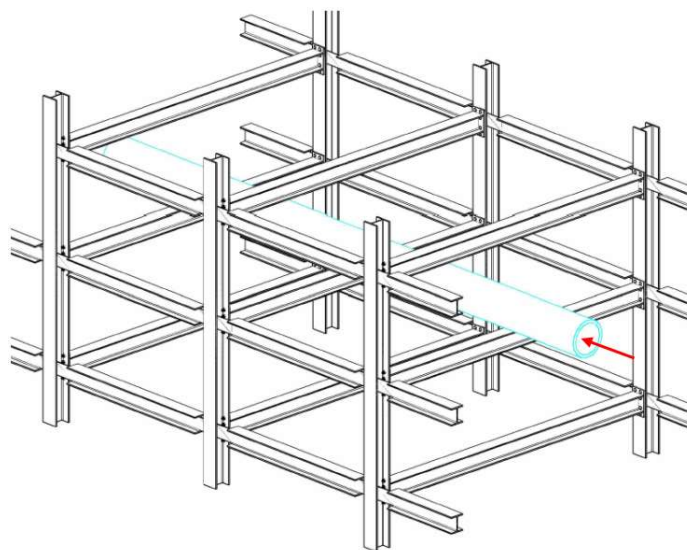
Figure 1.1: Pipe Rack Structure (Ahmad et al. 2018)
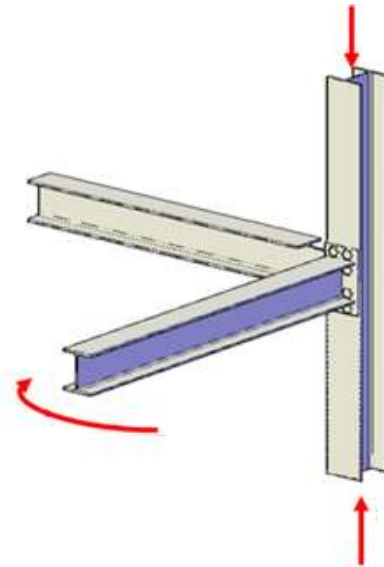
Figure 1.2: Load Combination in Pipe Rack (Adapted from Ahmad et al. (2016))

If the wide-flange column is unstiffened at the connection, localized distortion of the web can lead to additional rotations of the connected flange that are not accounted for in classical elastic torsion theory, shown in Figure 1.3. The addition of stiffeners to resist these loads ensures uniform rotation of the column and added torsional stiffness, which are not present in the unstiffened column. It is known that the unstiffened column has some capacity to resist torsional moment, but no complete design method is available for structural engineers faced with this kind of load combination.
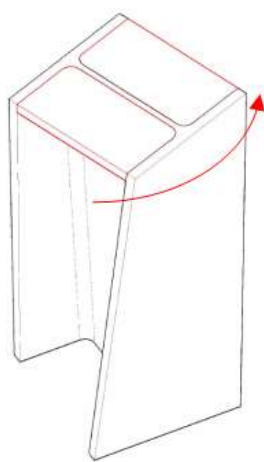
Torsion With Stiffeners
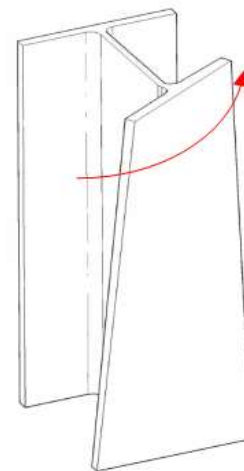
Torsion Without Stiffeners

Figure 1.3: Column Rotation With and Without Stiffeners (Ahmad et al. 2016)

1.2   Objectives and Scope

The main objective in the current research is to study the behaviour of unstiffened wide-flange members subjected to combined axial load and torsion applied through one flange. This includes providing reliable design equations that predict the strength and stiffness of the unstiffened connection, to help eliminate the use of unnecessary stiffeners in these types of loading scenarios. Recent research at the University of Alberta has revealed some information about how the torsional loads are shared between the flange (in torsion) and the web (in bending), but all tests were conducted with no axial force in the column. By studying the impact of different cross-sectional geometries and applied axial load, the current study aims to validate, and if necessary improve, the previously proposed design equations. This includes studying the effect of axial stresses on the capacity, flexibility, and load-sharing mechanism when resisting the torsional moment. A combination of frame–joint sub-assemblage tests and numerical frame simulations were conducted that include a variety of combinations of moment and axial force that represent a range of possible design scenarios encountered in industrial structures. The research considers the following principal geometric variables in the column: flange width and thickness, web thickness, and overall depth.

The scope of the current project is limited to studying the column response for the design scenario detailed in Figure 1.1. As such, the torsional moment is applied to the member through a bolted end-plate connection with dimensions shown in Figure 1.4. The variation in cross-sectional geometry is limited to a range of standard sections that are common in many industrial and commercial building applications. Nevertheless, the design procedures developed can easily be adapted to other cases where torsional moment is applied through one flange, such as edge beams supporting handrail/guards.
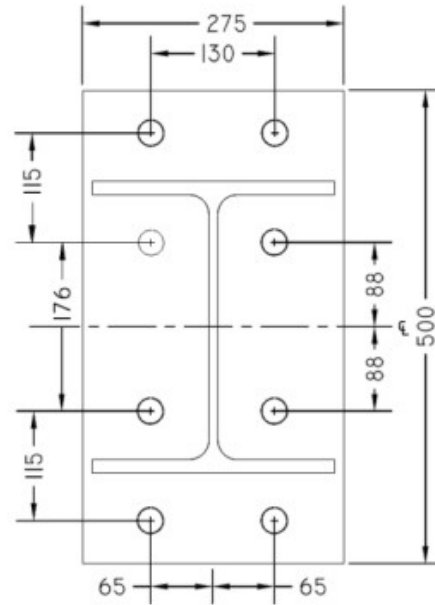
Figure 1.4: Bolted End-Plate Moment Connection (Ahmad et al. 2016)

Previous research showed how the torsional stiffness of the supporting member can impact the maximum torsional moment that can realistically develop. This is of interest to fabricators who often find fully fixed moment connections specified in the design documents, a situation that may not be attainable given the weak-axis bending capacity of the attached beam. To obtain a fully fixed moment connection according to the beam-line diagram shown in Figure 1.5, the connection must sustain 90% of the moment developed by the connected member. This, in turn, requires the joint to be very stiff. The current study focuses on the initial stiffness of unstiffened columns, tend to behave similarly to a simple connection when resisting weak-axis moment. This means that the connection resists no more than 20% of the connected beam's weak-axis moment capacity. Besides quantifying the torsional strength of the unstiffened joint, this research is intended to identify its torsional stiffness when axially-loaded wide-flange members are subjected to torsion applied through one flange.
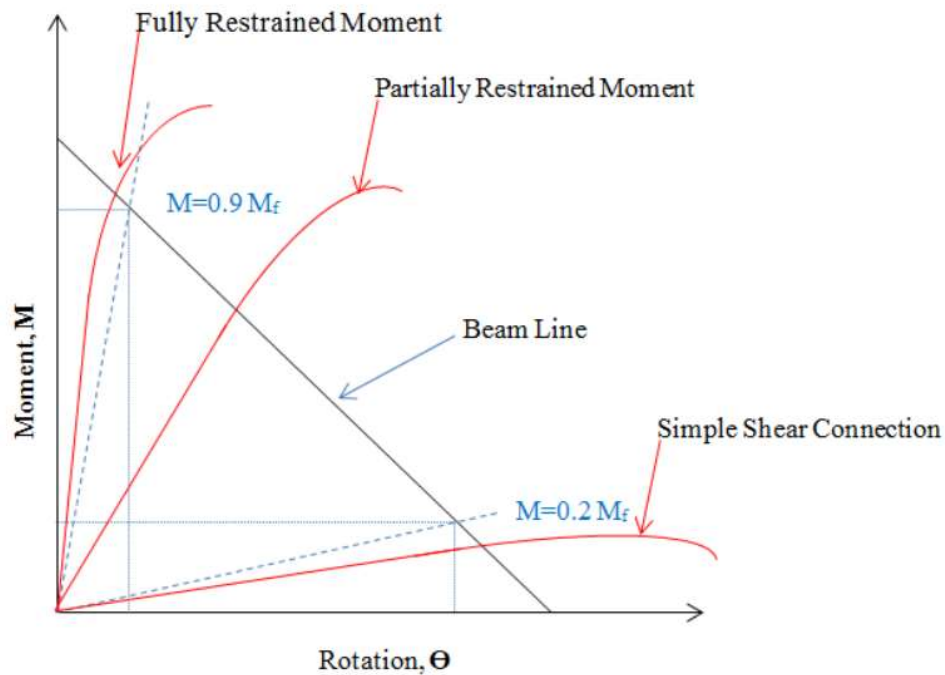
Figure 1.5: Beam Line Diagram with Connection Classifications (Ahmad et al. 2016)

Both steel fabricators and designers would benefit from a clear, simple, and widely applicable method for accurately determining the response of wide-flange members subjected to complex load combinations. A reliable model for predicting the strength and stiffness of beam-to-column weak-axis moment connections confers savings in both material and labour by eliminating the use of unnecessary stiffeners in these kinds of loading scenarios.

1.3 Report Anatomy

The report is divided into six chapters. Chapter 2 is a literature review that summarizes the relevant research that has been conducted prior to the current study. Chapter 3 summarizes the finite element analysis through discussions of modelling techniques, a parametric study, and numerical test results. Chapter 4 details the full-scale testing program, including test setup, test matrix, results, and parametric comparisons. Chapter 5 uses the results of Chapters 3 and 4 to support proposed design equations that predict the strength and stiffness of the unstiffened column. The final chapter summarizes the work done in the current research and provides recommendations for future studies. Supporting documents and additional results from the numerical analyses and full-scale testing program are provided in the appendices.

2   Literature Review

Few studies have been conducted to investigate the strength and stiffness of wide-flange sections subjected to torsion applied through one flange, and none in the presence of axial load. The relevant work done by previous researchers is summarized in this chapter.

2.1   Milner and Rao (1977 – 1979)

Studies relating to the torsional response of unstiffened wide-flange members go back to work done by Milner and Rao in the 1970s. They investigated the stiffness of lateral braces connected to the tension flange of simply-supported, wide-flange beams loaded with equal end moments about the strong axis of the member. The primary interest of the study was to investigate whether bracing connected to the tension flange could provide a "complete" bracing condition where both lateral and rotational movement of the beam are sufficiently restrained at the brace location to prevent lateral–torsional buckling. The tension-flange brace must provide both translational and rotational restraint to the critical compression flange. The lateral restraint is provided by the axial stiffness of the brace, relying on the ability of the joint to transfer the load, and the rotational restraint is provided by the bending stiffness of the brace. However, the bending stiffness of the brace may not be fully mobilized due to flexing in the joint and localized distortions in the web of the wide-flange beam. This suggests that the effective brace stiffness, K_e, is a combination of all components that contribute to rotational restraint, as follows:

$$\frac{1}{K_e} = \frac{1}{K_b} + \frac{1}{K_j} + \frac{1}{K_w}$$

2-1

where

K_b = bending stiffness of brace

K_j = joint stiffness

K_w = localized bending stiffness of the web

The parameter most relevant to the current study is the localized web stiffness, K_w, which was determined using a finite strip model and verified with a 1/10-scale laboratory experiment in which a torsional moment was applied to a single flange of a wide-flange section through a bolted purlin connection, as shown in Figure 2.1. Deformation of the flange under the torsional moment was measured relative to a series of mirrors placed a minimum of six times the beam depth away from

the connection, where the flange distortion was considered negligible. A second test, under the same torsional moment, was performed with heavy bars clamped across the outer edges of the flanges to prevent relative deformation of the flanges near the loading arm. The rotation caused by localized web distortion was then isolated by taking the difference in flange rotation between the test where flexing of the web was permitted and the test where heavy bar clamps prevented cross-sectional distortion. The testing program investigated different beam lengths as well as two and three-span configurations making a total of 45 buckling tests. The test setup shown in Figure 2.1 was designed such that the joint stiffness, K_j, was very large to ensure it had minimal effect on the effective brace stiffness, while a slender beam was selected to amplify the effects of local web distortion. It should be noted that web distortion due to a transverse shear force (from tension or compression in the brace) was incorporated into the finite strip model, but was considered negligible compared to the effects of the torsional load.
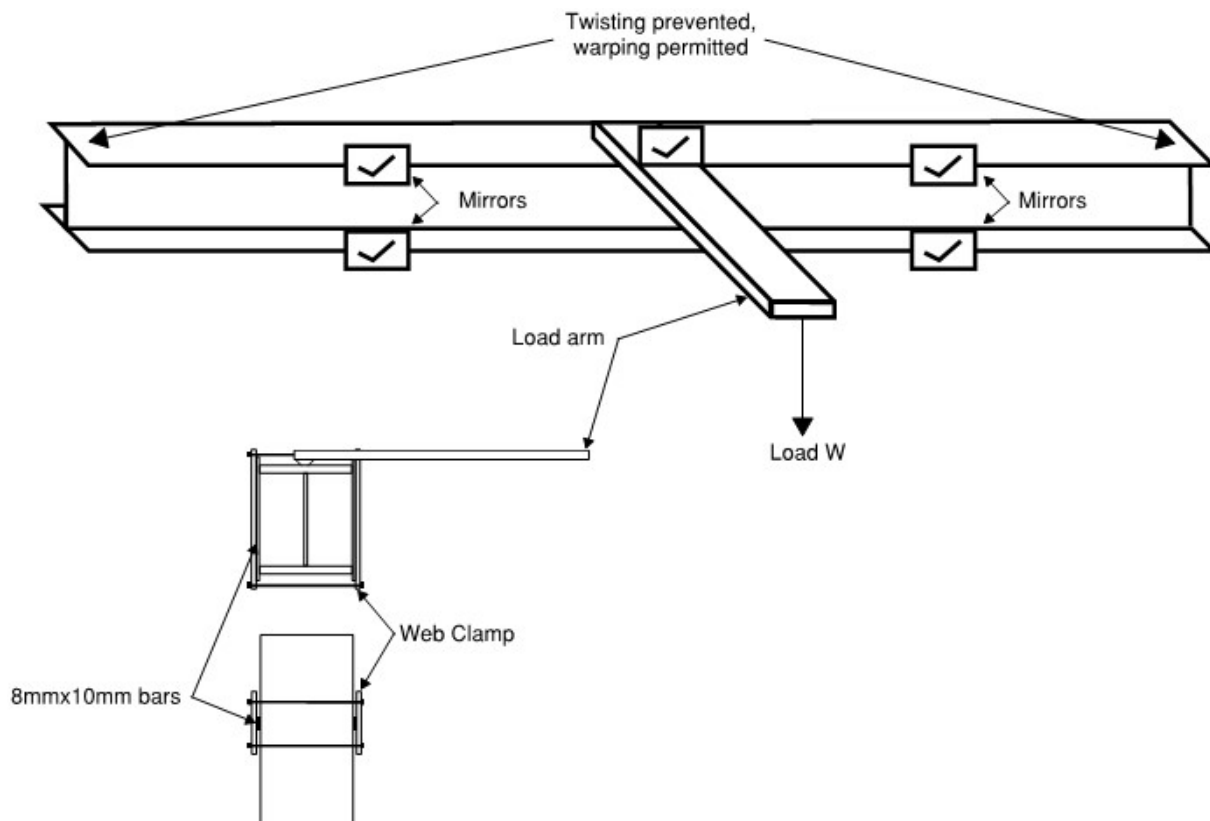
Figure 2.1:Localized Web Distortion Test Setup (Adapted from Milner (1977))

Milner and Rao (1977) derived Equation 2-2 using a beam analogy to describe the localized web stiffness, where E is Young's modulus, w is the nominal web thickness, and C is an empirical constant that is largely affected by the ratio of the torsional stiffness of the flange to the bending stiffness of the web.

$$K_w = CEw^3 \qquad \text{2-2}$$

Using results from the finite strip analysis, Equation 2-3 was obtained, which provides a value of C for varying cross-sectional geometries. Milner and Rao (1977) achieved close agreement between the theoretical and finite strip models and found that C was approximately equal to 0.67 for the sections under consideration; however, full-scale verification of the constant C was limited due to premature yielding and failure of the beam. This led the authors to suggest the value of C be conservatively taken as 0.5 until further tests could be conducted using more slender webs.

$$C = 1.3 - 160r - 0.8r^2 \qquad \text{2-3}$$

where the stiffness ratio, r, is defined as:

$$r = \frac{dw^3}{bt^3} \qquad \text{2-4}$$

where

d   = member depth

b   = flange width

t   = flange thickness

Milner and Rao (1978) also performed full-scale tests on equal-flange I-shaped members subjected to a torsional moment applied to one flange by light-gauge lipped channel purlins bolted to the top flange of the beam through a horizontal lap plate. This program was conducted primarily to determine the impact of local web distortions on the effective brace stiffness and the associated effects on the critical moment of beams subjected to lateral–torsional buckling failure. The test setup is shown in Figure 2.2.
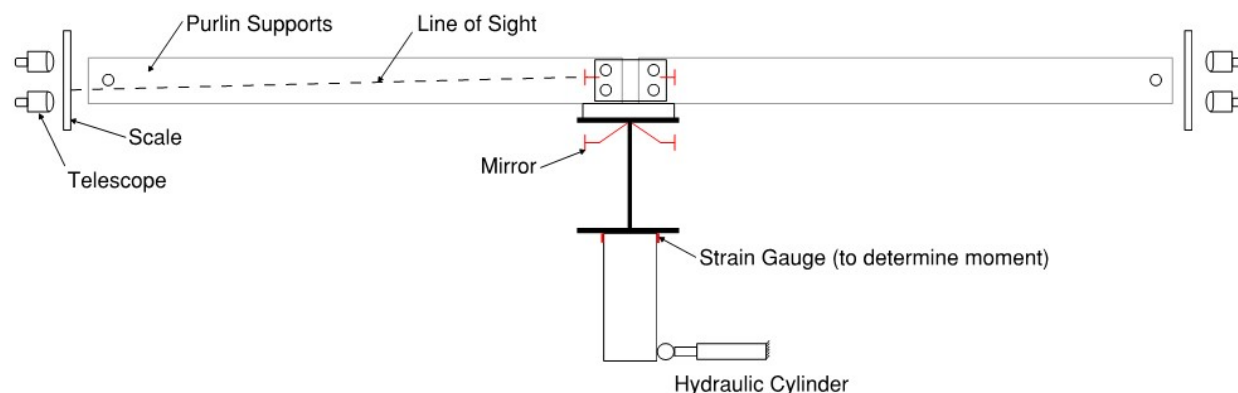
Figure 2.2: Test Setup for I-Shaped Members Braced by Lipped Chanel Purlins (Adapted from Milner and Rao (1978))

The results of these tests verified the theoretical predictions for web stiffness predicted by Equation 2-2. K_b was determined by conventional elastic bending theory, while K_j was determined through back calculation based on the measured test results. It should be noted that the purlin connection used in Milner and Rao's (1977; 1978) testing program was considerably more flexible than the weak-axis moment connections being analyzed in the current research.

2.2   Yura (2001)

Yura (2001) performed studies relating to the behaviour and design of torsional bracing using finite element modelling. Expanding on the work by Milner and Rao (1977; 1978), Yura suggested a revised web stiffness equation that includes potential for the presence of stiffeners and directly defines the width of web engaged to resist the applied torque. This effective width was embedded in the constant, C, from Equation 2-3 of Milner and Rao's research by assuming the connection dimension along the beam axis was zero in the original equation and the width of web that resists the applied torque is linearly related to section depth. The assumption of a negligible connection dimension is reasonable because the loads were applied through a thin vertical connection plate welded to the beam top flange in the full-scale testing program, suggesting the connection width was small in comparison to the influence region. Equation 2-5 is the localized web stiffness of an unstiffened wide-flange beam suggested by Yura, which is analogous to the K_w term defined by Milner and Rao.

$$\beta_{sec} = \frac{3.3E}{h}\left[\frac{(N+1.5h)w^3}{12}\right] \qquad\qquad 2\text{-}5$$

where N refers to connection width (along the beam axis) and h is the section depth, defined as the distance between the centroids of the flanges. Yura assumed the width of web effective in resisting local web distortion extended 0.75h beyond the connection, as depicted in Figure 2.3.
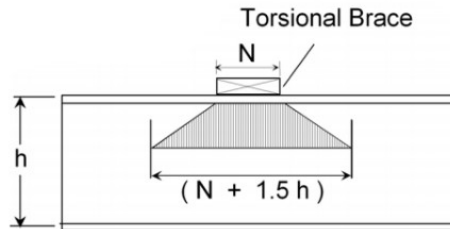
Figure 2.3: Effective Web Width (Yura 2001)

By setting the connection width equal to zero and rearranging to the form of Equation 2-2, it can be shown that Yura obtained a C-value of 0.41, slightly more conservative than what was suggested by Milner (1977). The stiffness parameter, β_{sec}, showed good agreement with the results of the finite element models.

2.3   Dowswell (2010)

Dowswell studied the effects of torsion applied to one flange of a wide-flange section. He created 32 elastic finite element models based on sections from the *Steel Construction Manual* (AISC 2005) to study the localized bending stress that develops in the web due to the applied torque. Extending work of Yura (2001) and Milner and Rao (1977; 1978), he combined Equation 2-2 (with C equal to 0.5) and Equation 2-5 to obtain an expression for the effective web width, W_{eff}, that is implied by Yura's localized web stiffness:

$$W_{eff} = 1.82h \qquad\qquad 2\text{-}6$$

By curve-fitting the results of the finite element analyses, Dowswell (2010) suggested an empirically derived equation for the effective width that could be used to obtain the nominal plastic moment capacity of the web. These expressions are given in Equations 2-7 to 2-9.

$$W_{eff} = N + 1.8\frac{t}{w}\sqrt{bd} \qquad\qquad\qquad 2\text{-}7$$

$$Z_{eff} = \frac{W_{eff}w^2}{4} \qquad\qquad\qquad 2\text{-}8$$

$$M_n = F_y Z_{eff} \qquad\qquad\qquad 2\text{-}9$$

2.4   Kaufmann et al. (2003)

Kaufmann et al. (2003) studied the effect of the manufacturing process on the material properties of wide-flange members within the area commonly known as the "K-region". The K-region is near the toe of the fillet where material properties can change drastically due to cold-straightening the member during manufacturing. This coincides with the initial yielding location on the wide-flange member subjected to torsion as identified by Ahmad et al. (2018), indicating that the material properties in this region are critical to identifying the initial yield moment of the member accurately.

Kaufmann et al. (2003) performed a series of tests to investigate the inelastic behaviour of A572 Grade 50, A913 Grade 50, and A36 rolled sections when subjected to different levels of pre-straining and cyclic loading. To study the impact of inelastic pre-strain, longitudinal specimens were cut from near the mid-depth of the web for each steel grade and subjected to a tensile pre-strain of either 2%, 8%, or 12% and then unloaded. They were then tested to failure in tension. Cyclic loading behaviour was determined in accordance with ASTM Standard E606. Test specimens cut from each material were subjected to four strain-range levels of ±2%, ±4%, ±6%, and ±8%, where each test consisted of 10 tension–compression cycles at a single strain range. Because there were no indications of fatigue cracking in any test specimens within ten loading cycles, three additional tests were conducted at strain ranges of ±2%, ±6%, and ±8% where loading cycles continued until initiation of fatigue cracking. The number of loading cycles needed to cause fatigue cracking varied between several hundred for the specimen at 2% strain range and 25 for the specimen at 8% strain range. Tension tests were also performed on coupons cut adjacent to the fillets of three W14×176 Grade ASTM A992 members from a single heat of steel. One of the members remained un-straightened for reference purposes and the other two were rotary or gag straightened. A summary of the coupon locations is shown in Figure 2.4.
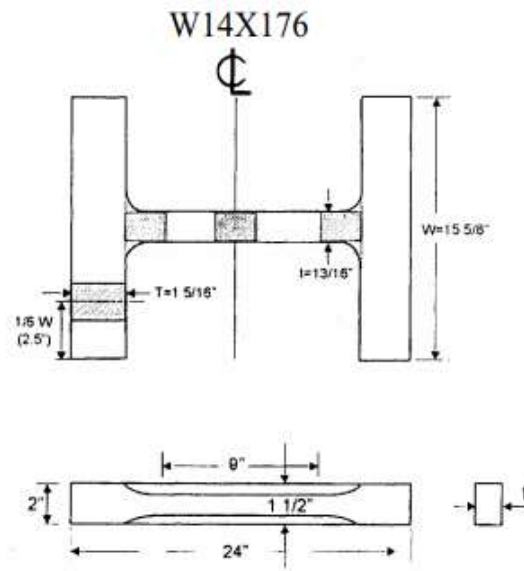
Figure 2.4: Tension Coupon Layout (Kaufmann et al. 2003)

The tensile properties of the four coupons within the K-regions of the straightened members showed considerably higher yield strengths (mean of 40% higher) and reductions in elongation (68%), when compared with the properties obtained from the un-straightened member. Kaufman noted that the steel within the K-region exhibits similar strength and ductility to tension tests performed on test specimens subjected to 8-12% pre-strain. This indicates that the critical region of the web is likely to have a higher yield strength and lower ductility than would be indicated by the mill test report if the member were straightened after rolling. This increased yield stress provides additional strength to the wide-flange member when subjected to a torsional moment applied to one flange, which has been ignored in previous attempts to predict the initial yield moment under this kind of loading scenario. It should be noted that coupons located in the K-region of the un-straightened member had similar material properties to those taken from mid-depth of the web. This indicates the increased yield stress in this region can only be expected when the member is cold straightened.

2.5   Gil et al. (2015)

Gil and Goñi (2015) and Gil et al. (2015) investigated the behaviour of bolted end plate beam-to-column connections when a T-stub (representing one-half of a wide-flange) is subjected to out-of-plane bending. The major objectives of this study was to perform full-scale tests and numerical

simulations to guide the development of a method for classifying these connections as rigid, flexible, or semi-rigid. The test results were used to create a design procedure based on the component method that can be used to predict the connection strength and stiffness. The components considered by Gil et al. (2015) were assembled into a model summarized in Figure 2.5. The overall connection behaviour can be predicted by combining the strengths and stiffnesses of the individual components.

bf,t   = beam flange in tension

bf,c   = beam flange in compression

ep,b,t = end plate in bending (tension)

ep,b,c = end plate in bending (compression)

cf,b,t = column flange in bending (tension)

cf,b,c = column flange in bending (compression)

cw,b = column web in bending
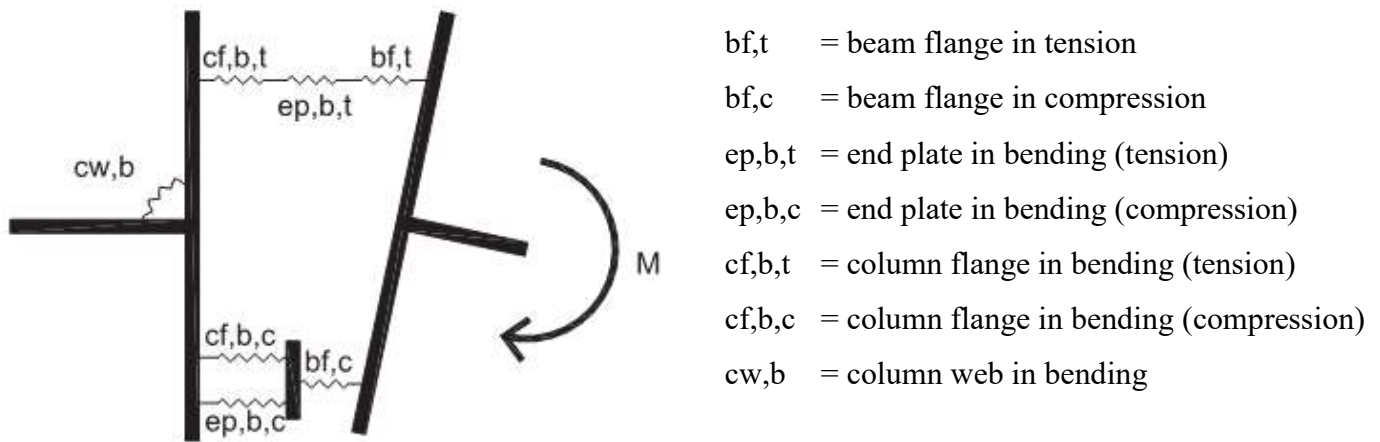
Figure 2.5: Component Model for T-Stub in Out-of-Plane Bending (Gil et al. 2015)

The full-scale testing program consisted of five tests that investigated changes in column cross-sectional geometry, the presence of stiffeners, and the effect of a welded connection versus a bolted end plate connection. A summary of the test configurations is provided in Table 2-1.

Table 2-1: Experimental Test Matrix Summary

Test	Column (L=1200mm)	Beam (L=500mm)	End Plate (mm)	Steel Grade	Joint Type
T-Stub01	HEB 160	IPE 300	10	S275	4 bolts Ø 16
T-Stub02	HEB 160 + Stiffeners	IPE 300	10	S275	4 bolts Ø 16
T-Stub03	HEM 160	IPE 300	10	S275	4 bolts Ø 16
T-Stub04	HEB 160	IPE 300	-	S275	Welded
T-Stub05	HEB 160 + Plates	IPE 300	10	S275	4 bolts Ø 16

Strain gauges were fitted at several locations on the connection to measure yielding of each component, and inclinometers were placed at three locations to measure the rotation of the column web, column flange, and loading beam. A summary of the instrumentation layout is shown in

Figure 2.6. It should be noted that strain gauges were not placed at the toe of the fillet of the column, which was the location of initial yielding for two tests. Joint rotation was calculated by taking the difference between the rotations obtained by the inclinometers placed on the loading beam flange and the column web.
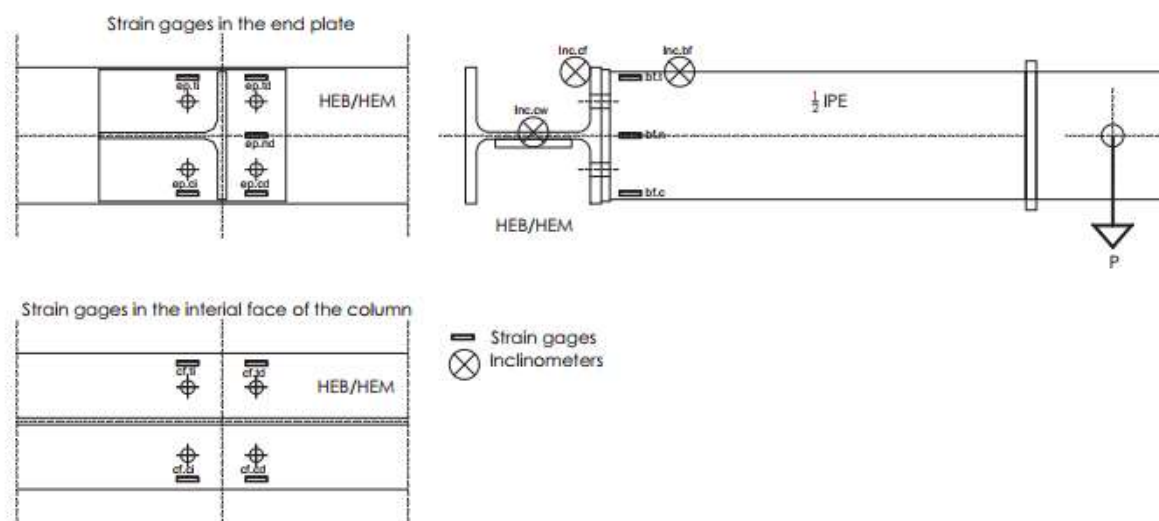
Figure 2.6: Instrumentation Layout (Gil et al. 2015)

Most relevant to the current study are T-Stub01, -03, and -04, which feature an unstiffened column with varying cross-sectional geometries and details. Tests T-stub01 and -04—differing only by the former incorporating a flexible bolted end plate at the joint and the latter having the beam welded directly to the column flange—showed yielding of the column initiating at the toe of the fillet, near the flange-to-web junction, followed by yielding of the column flange and finishing with yielding of the end plate (for T-Stub01 only). This indicates the column web in bending was the governing component in terms of connection strength if the limit state is taken at first yield of the connection elements. T-Stub03 had a much heavier column section that remained elastic, with the majority of yielding and rotation caused by plastic deformation of the end plate and beam flange. All tested joints were classified as semi-rigid according to guidelines set out by the Eurocode.

A numerical model was developed in ABAQUS using solid elements with reduced integration (C3D8R). The full beam-to-column connection was modelled with measured material properties. Torsionally fixed boundary conditions were used at both ends of the column by preventing rotation and displacement of the end nodes. The mesh was refined until good agreement between the full-

scale tests and numerical models was achieved. A parametric study with the calibrated model was then conducted to investigate the impact of column length, end plate thickness, and column size. These results were employed to model the strength and stiffness of each component described in Figure 2.5. Using guidelines set out by the Eurocode, individual components were combined to predict the overall strength and stiffness of the connection. Most relevant to the current research is the quantification of the components that model the response of the column subjected to a torsional moment through one flange, namely, the flange in torsion and web in bending.

The strength and stiffness of the column flange in torsion was modelled as an isolated rectangular element, clamped at both ends. The column web in bending was characterized by assuming it behaves as a beam spanning between flanges and restrained by a rotational spring at each end, whose stiffness is equal to the torsional stiffness of the flanges. Gil et al. (2015) noted the effective width, which refers to the width of web that is mobilized to resist the torsional moment, remained between 700 and 800 mm in all simulations. This matches the results of the parametric study well when set equal to twice the effective width of the column flange in bending, which in turn includes several empirical factors based on the results of the parametric study.

The procedure outlined by Gil et al. (2015) produces strengths and stiffnesses that match the results of the full-scale tests and numerical simulations. To apply the proposed design method, designers are required to quantify the strengths and stiffnesses of eight components and assemble them based on static equilibrium to establish an overall connection strength and stiffness for use in design.

2.6   Ahmad et al. (2016; 2018)

Ahmad et al. (2016; 2018) studied the behaviour of wide-flange members subject to torsion applied through one flange. The research was focussed on characterizing the strength and stiffness of an unstiffened beam-to-column weak-axis moment connection. Routine design procedure suggests adding web stiffeners to the column to avoid local cross-sectional distortion around the connection. By characterizing the strength and stiffness of the unstiffened connection, the research aimed to determine the necessity of stiffeners in these kinds of loading scenarios. First yield on the wide-flange member was selected for the limit of column strength to avoid excessive distortion around the connection and to ensure the column has considerable reserve capacity to deform and resist load if the design forces are exceeded.

An extensive finite element analysis investigation using ABAQUS was conducted to determine the major factors controlling the behaviour of these members. The initial yield moment on the cross-section and flange rotation were the main behavioural aspects of interest. The researchers considered changes in boundary condition, length, the presence of stiffeners, and cross-sectional geometry, including flange width, flange thickness, web thickness, and section depth. A summary of the impact of these parameters is as follows:

- Boundary Condition: The overall torsional stiffness of the connection was influenced by the boundary condition at the ends of the column despite the localized nature of the load. With warping permitted at the ends of the member, an appreciable decrease in stiffness was observed compared to a member with warping fully restrained at the ends. Conversely, the initial yield moment was insensitive to the column boundary condition.

- Length: There was a notable increase in flange rotation at first yield for an 8 m-long member compared to a 4 m-long member. The yield moment did not differ significantly for the two column lengths.

- Stiffeners: Columns with full-depth web stiffeners behaved similarly to the response obtained from conventional elastic torsion theory considering the whole cross-section, indicating that localized web distortions were fully restrained. This resulted in a marked increase in both strength and stiffness of the connection. When partial-depth stiffeners were used, the highly stressed region was located at the root of the stiffener, resulting in progressively less strength and stiffness as the stiffeners depth decreased.

- Flange Width: Increasing the flange width added both strength and stiffness to the connection, but this was considerably less influential than most of the other geometric variables.

- Flange thickness: Doubling the flange thickness improved both strength and stiffness of the connection, indicating it was an important factor when characterizing its strength.

- Web Thickness: The impact of web thickness was determined to be the most influential geometric factor to both strength and stiffness of the connection. Doubling the web thickness resulted in a marked increase in both the yield moment and torsional stiffness.

- Section Depth: This was determined to be the least influential geometric parameter regarding the yield moment and torsional stiffness.

Based on results from this parametric study, Ahmad et al. (2018) determined that first yield of an unstiffened wide-flange column was concentrated at the surface of the web near the toe of the fillet. The most influential geometric parameters were w^3 (coming from bending stiffness of the web) and bt^3 (from torsional stiffness of the flange). These were combined to produce a ratio of the major resisting components, shown in Equation 2-10. Section depth was eliminated from the stiffness ratio suggested by Milner and Rao (1977) due to its limited influence on the overall behaviour. Values of r_1 were calculated for a series of standard sections and appeared to capture variation in both moment capacity and elastic moment–rotation response well.

$$r_1 = \frac{bt^3}{w^3}$$
2-10

The full-scale testing program consisted of nine tests; all specimens were taken from the *Handbook of Steel Construction* (CISC 2010) and selected to fit within the geometric constraints of the parametric study. Test specimens were unstiffened aside from one with two sets of 25 mm stiffeners extending the full depth of the section at the loading location for comparison purposes. The boundary conditions were intended to be torsionally fixed by providing stiff end plates at the ends of the specimen, connected to stocky columns by pre-tensioned bolts. The torsional moment was applied by an actuator that created weak-axis bending in a cantilever W310×92 loading beam fastened to the flange of the test specimen at midspan with pre-tensioned bolts. The test setup is shown in Figure 2.7.
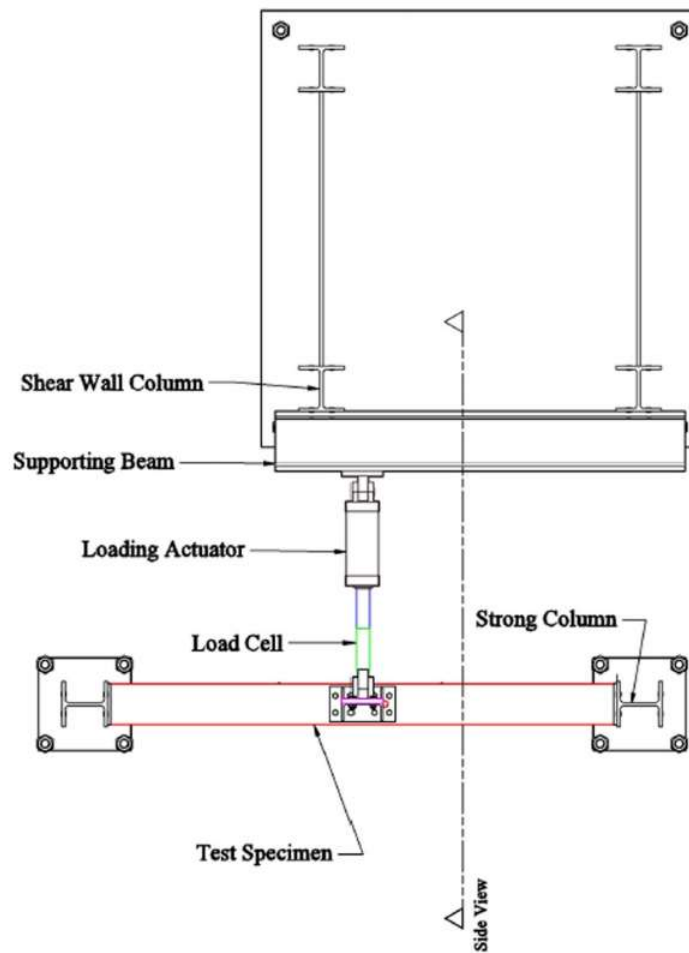
Figure 2.7: Full-Scale Test Setup (Ahmad et al. 2018)

Ahmad et al. (2016) found no significant twist at the ends of the specimen after each test, but did measure around 2 mm of warping displacements for nearly all cases. This indicated that complete torsional fixity was not maintained throughout the test, and in fact, the behaviour was closer to torsionally pinned. This is confirmed by the finite element models that employed measured material properties and nominal dimensions given in the *Handbook of Steel Construction* (CISC 2016). Figure 2.8 compares the moment–rotation response of a W310×129 member tested in the lab with numerical models assuming both torsionally fixed and torsionally pinned end restraints.
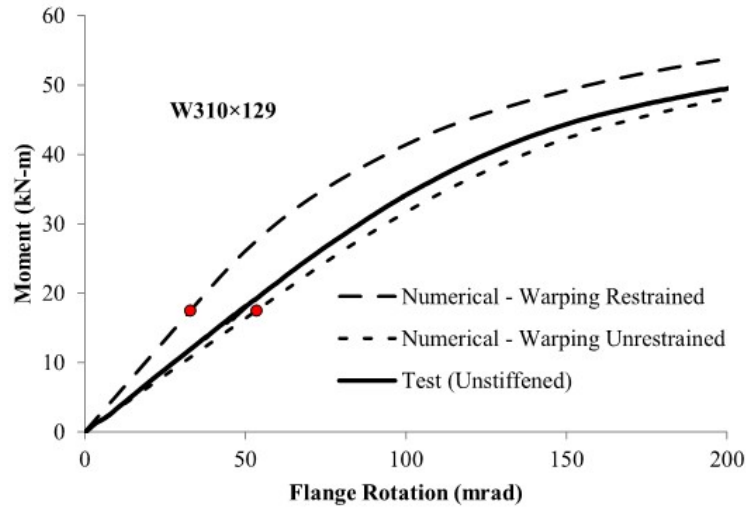
Figure 2.8: Moment–Rotation Comparison with Numerical Results (Ahmad et al. 2016)

Ahmad et al. (2018) noted the yield moment observed in the tests were, in most cases, slightly lower than what was predicted by the numerical models. Although small, it was suggested the difference is due to the presence of tensile residual stresses neglected in the numerical analysis. White washing the web around the connection was used to identify the initial yield moment in the first test; however, this was not reliable as the yielding location was highly localized and could not be accurately identified through white washing. All other tests utilized linear strain gauges at the yielding location to identify first yield.

Results from the parametric study and full-scale testing program were used to expand on the ideas of Milner and Rao (1977; 1978) by suggesting the elastic stiffness of the wide-flange section (K_u) was a combination of the localized web stiffness (K_w) and the overall torsional stiffness of the member (K_s):.

$$\frac{1}{K_u} = \frac{1}{K_s} + \frac{1}{K_w} \qquad\qquad 2\text{-}11$$

The localized web stiffness, K_w, was modified from that of Yura (2001) to adopt the effective width defined in Equation 2-12, where the stiffness ratio, r_1, was calibrated to the results of finite element models. Using the same beam analogy suggested by Milner (1977), shown in Figure 2.9, to model the behaviour of the unstiffened web, Ahmad et al. (2018) recommended Equations 2-13 and 2-14 for determining the localized web strength and stiffness. For simplicity of use for design,

these formulations are derived by considering the bending strength of the web only, where the additional resistance provided by the flange in torsion is embedded into the effective width through the ratio r_1.
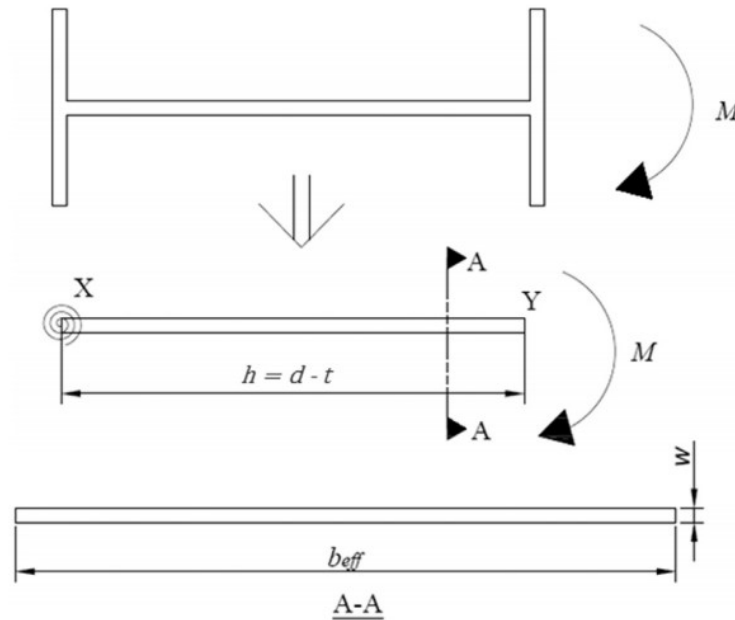
Figure 2.9: Design Analogy for Web Bending (Ahmad et al. 2018)

$$b_{eff} = N + r_1 \qquad\qquad 2\text{-}12$$

$$M_y = \frac{b_{eff}w^2 F_y}{6} \qquad\qquad 2\text{-}13$$

$$K_w = \frac{3.3E}{h}\left[(N + 1.5r_1)\left(\frac{w^3}{12}\right)\right] \qquad\qquad 2\text{-}14$$

Ahmad et al. (2018) studied the impact of length and boundary condition on the localized web strength and stiffness. They determined these factors have significant impact on the overall torsional stiffness of the member; however, the localized web stiffness and strength, which was determined through finite element analysis, did not change significantly by doubling the length or changing from torsionally fixed to torsionally pinned at the ends of the member.

The overall elastic torsional stiffness of the member (K_s) is obtained by solving the generalized equation for the angle of twist (α), assuming a concentrated torque applied at mid-length of the member, as shown in Equation 2–15.

$$\alpha = C_1 + C_2 \cosh(\lambda z) + C_3 \sinh(\lambda z) + \frac{M_z z}{\lambda^2 E C_w} \qquad \text{2-15}$$

$$\lambda = \sqrt{\frac{GJ}{E C_w}} \qquad \text{2-16}$$

where M_z refers to the internal torque, z is the distance from the end of the member to the transverse section being examined, and C_w is the warping torsional constant. Constants C_1 to C_3 are determined from the boundary conditions for the specific problem being investigated. Other elements of the equation are determined based on applied loads, material, and geometric properties of the column. Dividing the elastic yield moment by the angle of twist determines the elastic stiffness of the member.

Ahmad et al. (2016) considered the presence of axial load using numerical modelling only. They performed 96 numerical simulations to investigate the impact of length and cross-sectional geometry on the torsional response of wide-flange members under different levels of axial load. Each geometry and length was tested at 25%, 50%, and 75% of its axial yielding capacity to study the impact of axial load on the moment at first yield of the cross-section and elastic stiffness of the member. A general reduction in yield moment with increased levels of axial stress was noted. The results from one of these cases is shown in Figure 2.10 where the moment was measured at midspan of the member.
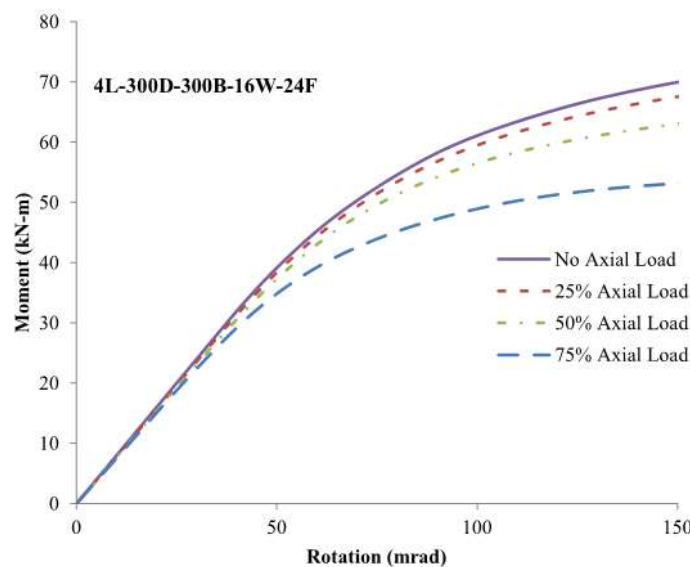
Figure 2.10: Moment–Rotation Response Under Varying Axial Load (Ahmad et al. 2016)

Figure 2.10 shows that the initial slope of the response curves is constant regardless of the compressive stress applied to the member, leading to the conclusion that the initial stiffness does not change based on the axial load. This suggests Equation 2-14 need not be modified to account for the presence of axial compression. Equation 2-17 is a modification of Equation 2-13 to account for the effect of axial load on moment capacity. The yield stress has been replaced by an expression that uses the von Mises yield criterion to reduce the amount of bending stress that can develop at the web surface prior to yielding based on the level of applied axial load. It is assumed the only non-zero stress components in the von Mises equation are the applied axial stress and the bending stress from the applied torque.

$$M = \left| \frac{\frac{P}{A} - \sqrt{4\,F_y{}^2 - 3\left(\frac{P}{A}\right)^2}}{2} \right| \frac{b_{eff}\,w^2}{6} \qquad \text{2-17}$$

Where P represents the applied compressive load and A represents the cross-sectional area. Ahmad et al. (2016) noted that Equation 2-17 under-predicts the yield moment given by the finite element analysis by increasing amounts as the axial stress increases. The results of the finite element analysis were used to suggest the interaction behaviour given in Equation 2-18, where P_y and M_y refer to the nominal compressive yield force and the yield moment predicted by Equation 2-17, respectively.

$$\left(\frac{P}{P_y}\right)^2 + \left(\frac{M}{M_y}\right)^2 = 0.8 \qquad \text{2-18}$$

The interaction allows the section to reach 80% of its axial or bending capacity, even when the other component is zero. Additionally, it does not consider the column buckling capacity, or residual stresses that may be present. The reduction in yield moment that occurred when the axial load increased varied greatly among the 96 models in the parametric study.

3   Finite Element Analysis

Numerical simulations provide a low cost and efficient way of establishing global relationships that impact the strength and stiffness of the wide-flange member. The behaviour of unstiffened wide-flange members subjected to combined axial load and torsion applied through one flange was investigated using ABAQUS general purpose finite element modelling software. Changes in cross-sectional geometry and applied axial load were considered to better understand their impact on the overall behaviour. The modelling and analysis techniques are summarised in this chapter.

3.1   Numerical Model

The model developed by Ahmad et al. (2018) was modified in the current study to include the presence of axial load. Under pure torsion applied through one flange, this model has been verified using results obtained from full-scale laboratory tests. The assembly of a typical wide-flange section is shown in Figure 3.1 where all models utilized 8-node solid elements with full Gaussian integration (C3D8). Ahmad et al. (2016) noted that neither shell elements nor solid elements with reduced integration could accurately capture the strength and stiffness in the web, which is considered the most significant geometric parameter that influences the resistance mechanism of the wide-flange member to a torsional moment. The cross-section of the wide-flange member was modelled in 2D and extruded through its length of 4 m.
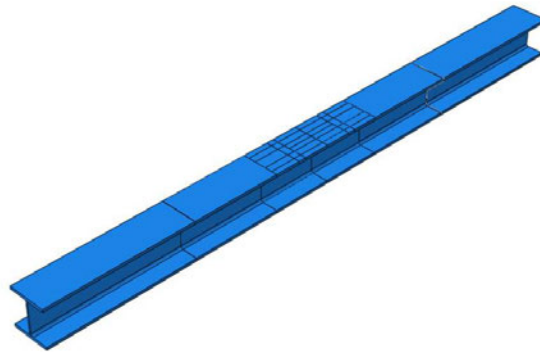

Figure 3.1: Wide-Flange Column Assembly in ABAQUS

3.1.1 Material Properties

The material model assumes isotropic elasto-plastic behaviour with a Young's modulus of 210,000 MPa and Poisson's ratio of 0.3. A yield stress of 350 MPa was specified with an ultimate

true stress of 700 MPa at a plastic strain of 29%. The instance of first yield on the web surface was identified using the equivalent plastic strain (PEEQ) function in ABAQUS, where a non-zero value indicates the presence of plastic strain.

3.1.2 Loading

The wide-flange column is loaded in two separate, static general steps. First, the axial load is applied in four iterations, where each iteration applies one-quarter of the total force. Compression is applied as a concentrated force to a reference point at the end of the wide-flange member in the longitudinal direction. To avoid localised distortion under the concentrated force, a rigid body tie constraint is applied to all nodes on the cross-section at the loaded end of the member. By tying these nodes to the reference point where the load was applied, the axial force is evenly applied over the entire cross-section.

The final loading step holds the axial force constant while applying increments of 0.5 kN·m of torsional moment to allow precise identification of first yield. The torsional moment is applied mid-span on the wide-flange section through four pressure loads, as shown in Figure 3.2. Applying the torsional moment through a series of pressure loads was compared to a full model assembly by Ahmad et al. (2016) that consisted of a complete weak-axis moment connection; where the response of the two models was virtually the same. By reversing the direction of the pressure load on either side of the web, a force couple is developed at the flange–web junction to simulate the torsional moment caused by weak-axis bending of an adjoining member. Pressure loads remain perpendicular to the surface to which they are applied, meaning that as the flange rotates, the pressure loads continue to apply pure moment as long as the flange remains straight. Each pressure is applied over a 50 mm × 50 mm square area to ensure the pressure load does not cause localised distortion of the flange. The distance between pressure loads acting in opposite directions was adjusted so the moment arm was equal to half the flange width of any given section. Each pair of pressure loads was spaced 400 mm apart to match the connection length of the model as-built pipe rack structure provided by the fabricator (shown in Chapter 1). To reduce computational time and effort, this method of applying the torsional moment has been adopted for all finite element models.
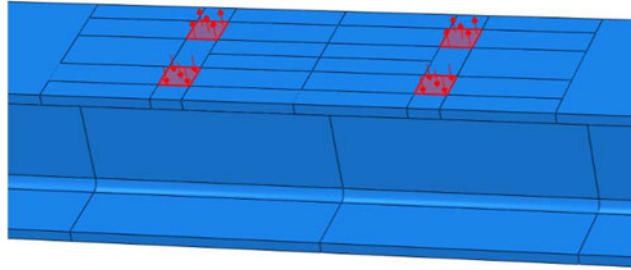
Figure 3.2: Simplified Torsional Loading

3.1.3 Boundary Conditions

The column end restraints were chosen to simulate torsionally fixed boundary conditions because it was considered unlikely that warping displacements would develop at the ends of the column given the large axial load. This was achieved in ABAQUS by restraining the nodes on the cross-section at both ends of the column from displacement and rotation in all directions. Longitudinal displacement of the cross-section was permitted at the end where the load was applied to transfer the axial force into the column; however, relative displacement of the nodes of the cross-section was prevented, meaning torsional fixity was maintained.

3.1.4 Mesh Optimization

The response of a wide-flange member subjected to a torsional moment applied to one flange is most sensitive to variations in web thickness. It was apparent through comparisons to laboratory test results that further mesh refinement was needed beyond what was used in previous research. Using results from the full-scale testing program performed by Ahmad et al. (2016), the number of elements through the web thickness was progressively increased until there was no notable change to the yield moment, as shown in Figure 3.3. The final mesh used in the current study utilized eight elements through the thickness of the web with full integration.
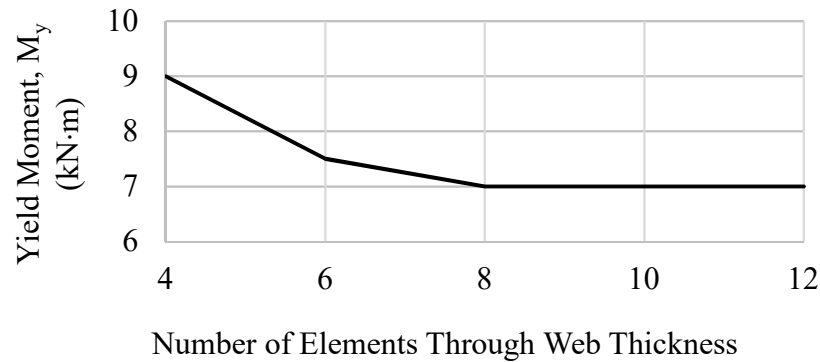
Figure 3.3: Mesh Convergence Strength Analysis for a W310×67

Table 3-1 shows the initial elastic stiffness at mid-span of the column flange. The stiffness remains constant once a minimum of six elements are provided through the thickness of the web, indicating the yield moment is more sensitive to the density of the mesh compared to elastic stiffness. An increase in both strength and stiffness is observed when the number of elements through the web thickness is reduced below six. Complex, localized loading in the web means a detailed analysis is needed in this region to capture the behaviour accurately.

Table 3-1: Mesh Convergence Stiffness Analysis for W310×67

# of Elements Through Web Thickness	Yield Moment (kN·m)	Rotation (rad)	Stiffness (kN·m/rad)
4	9	0.0478	188.4
6	7.5	0.0483	155.2
8	7	0.0451	155.4
10	7	0.0451	155.2
12	7	0.0449	155.9

3.2 Combined Axial Load and Torsion

3.2.1 Parametric Study

To pinpoint the major factor(s) causing inaccuracy between Equation 2-17 and the results of 96 numerical models analyzed under the presence of axial load by Ahmad et al. (2016), Equation 2-17 was separated into three distinct parts that were analyzed individually. Each component of the equation is described as follows:

1. Effective Width: Based solely on geometric properties of the wide-flange column and the connection length, this parameter defines the width of the effective stress block. The effective width is considered constant, regardless of the level of axial stress.

2. Bending Stress: The term bound in absolute values represents the maximum bending stress that develops at first yield. This value is affected by the material yield stress and applied axial stress; it assumes that only two components in the von Mises equation impact the bending stress at first yield and that it is constant over the effective width of web.

3. Stress Distribution: In the final term, $w^2/6$ comes from the assumption that the stress distribution is linear through the thickness of the web.

Ninety-six numerical models analyzed by Ahmad et al. (2018) investigated variations in member length and cross-sectional geometry under varying levels of axial load. Several cross-sectional geometries containing slender flanges (and all were 500 mm wide), showed a sharp decrease in initial yield moment as the axial load increased compared with other numerical tests containing stocky flanges. For this reason, five different cross-sectional geometries were modelled with flange widths ranging from 200 to 500 mm to identify its impact on the overall connection behaviour. Figure 3.4 shows the notation used to describe the geometry of the wide-flange columns considered. L, D, B, W, and F refer to column length, section depth, flange width, web thickness, and flange thickness, respectively. Additionally, five sections were modelled from the *Handbook of Steel Construction* (CISC 2016) that represent a large variation in effective width, b_{eff}, to obtain a wide range of behaviours.
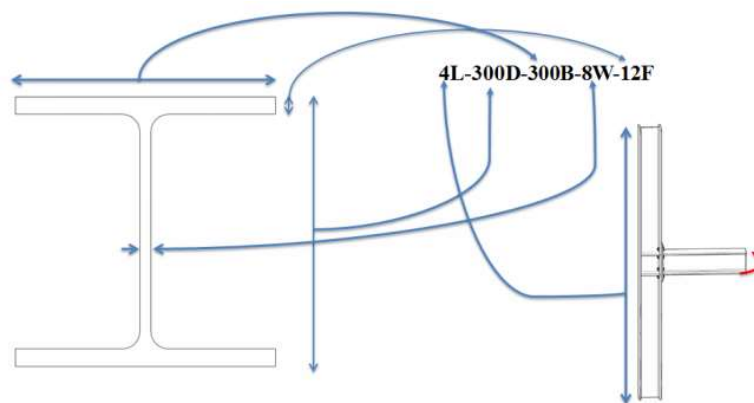
Figure 3.4: Notation Used for Wide-Flange Columns (Ahmad et al. 2018)

3.2.2 Results

The results of 42 finite element simulations are summarised in this section. Figure 3.5 details the moment–rotation response obtained from a W360×91 section with axial load ranging from 0 to 75% of the axial compressive yielding capacity of the member. As the axial load increases, the initial yield moment decreases and there is also a small reduction in elastic stiffness. Higher post-yielding rotations occur at a given moment with increasing axial load, which is most apparent between 50 and 75% axial load. This is expected because the column has less capacity to resist torsional moment when the material is highly stressed from the large compressive force.
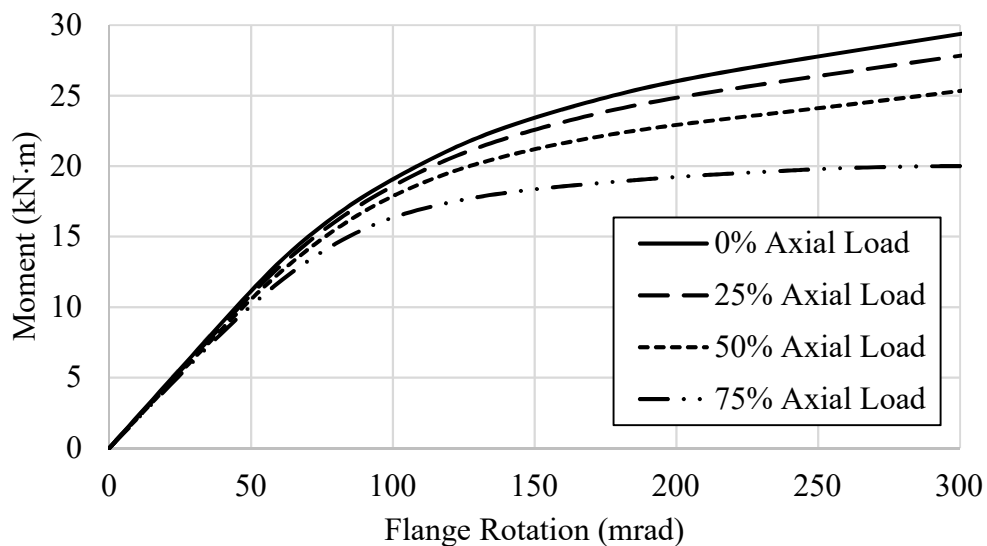
Figure 3.5: Numerical Moment–Rotation Response of W360×91 Under Varying Levels of Axial Load

Figure 3.6(a) and Figure 3.6(b) show the progression of plastic strain from the point of initial yielding up to 0.3 radians of flange rotation. In all numerical simulations, elastic behaviour was observed until yielding initiated at the surface of the web, below the pressure loads at the toe of the fillet. Yielding of the flange tips occurred shortly after and was expedited with increasing levels of axial load. As more torsional moment is applied, yielding of the bolted flange and web extend beyond the connection until full plastification of the column web occurs in the connection region.

Yielding

(a)

(b)
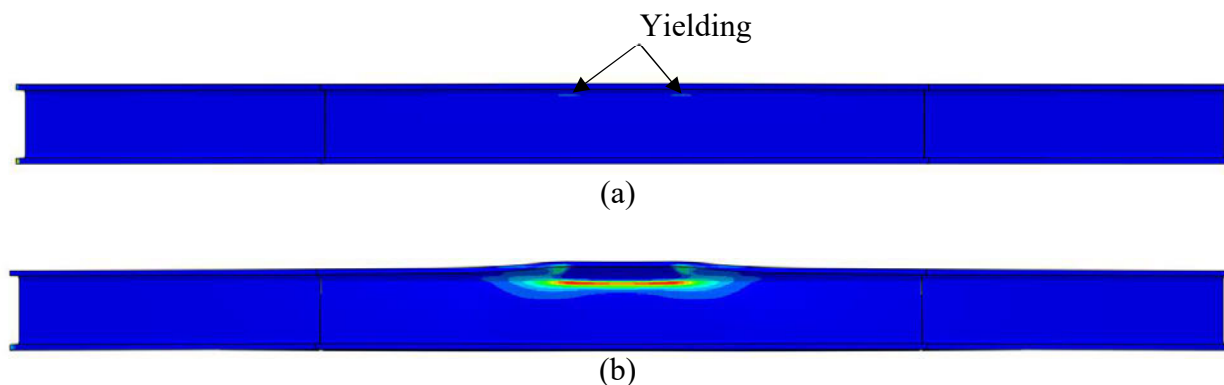
Figure 3.6: Yielding of Column Due to Axial Load and Torsional Moment:
(a) Initial Yield Moment and (b) 0.3 Rad of Flange Rotation

The initial yield moment, flange rotation, and elastic stiffness for 40 simulations were recorded for each section and are summarised in Table 3-2 to Table 3-4. An increase in flange width resulted in a modest increase in the initial yield moment, where Equation 2-17 continued to underestimate the initial yield moment in all numerical tests. The models used by Ahmad et al. (2018) utilized four elements through the thickness of the web, suggesting the overestimate in yield moment from Ahmad's models compared to Equation 2-17 may be caused, in part, by the coarse mesh that was used throughout the numerical testing program. It was also noted that several members with slender flanges far exceeded the design requirement for local buckling specified in CSA Standard S16. This is consistent with the sharp decrease in yield moment at high levels of axial load for many of these cross-sections, suggesting local buckling of the column flange may have been influential for some numerical tests with slender flanges; the loading was applied through a static general step not suitable for capturing local buckling of the column flange accurately. In a real column, local flange buckling would cause load shedding to other parts of the column, which can lead to premature yielding at the critical location or global buckling of the member. To avoid premature stability failures under the applied axial loads, the five wide-flange sections that were selected for modelling all satisfied S16 local and global buckling requirements up to 75% of their nominal axial yielding capacity.

Table 3-2: Initial Yield Moment Under Varying Levels of Axial Load

Section	Yield Moment (kN·m)			
Axial Load	0%	25%	50%	75%
4L-300D-200B-8W-12F	5.5	5	4.5	3.5
4L-300D-250B-8W-12F	6	5.5	4.5	3.5
4L-300D-300B-8W-12F	6	5.5	4.5	3.5
4L-300D-350B-8W-12F	6.5	5.5	4.5	3.5
4L-300D-500B-8W-12F	7.5	6	4.5	2.5
W250×89	10	9.0	8.0	6.0
W310×86	8.5	7.5	6.5	5.0
W310×129	16	14.5	12.50	10
W360×91	9.5	8.5	7.5	5.5
W360×162	21	19	15.5	12

Table 3-3: Flange Rotation at First Yield Under Varying Levels of Axial Load

Section	Flange Rotation (mrad)			
Axial Load	0%	25%	50%	75%
4L-300D-200B-8W-12F	53	50	47	38
4L-300D-250B-8W-12F	47	44	37	30
4L-300D-300B-8W-12F	41	39	34	27
4L-300D-350B-8W-12F	41	37	32	27
4L-300D-500B-8W-12F	40	37	33	28
W250×89	39	36	33	25
W310×86	41	37	33	26
W310×129	36	34	30	20
W360×91	42	39	35	26
W360×162	28	27	23	18

Table 3-4: Elastic Stiffness Under Varying Levels of Axial Load

Section	Elastic Stiffness (kN·m/rad)			
Axial Load	0%	25%	50%	75%
4L-300D-200B-8W-12F	104	100	96	92
4L-300D-250B-8W-12F	128	125	122	117
4L-300D-300B-8W-12F	146	141	132	130
4L-300D-350B-8W-12F	159	149	141	130
4L-300D-500B-8W-12F	188	162	136	89
W250×89	256	250	242	240
W310×86	207	203	197	192
W310×129	444	426	417	500
W360×91	226	218	214	212
W360×162	750	704	674	667

There is a consistent reduction in initial stiffness for all models with increasing levels of axial load. This effect is quite small in the numerical simulations, but may be more significant in full-scale tests where residual stresses are present in the column. It should be noted that at high levels of axial load, ABAQUS terminated the analysis due to convergence issues when applying extremely small increments of torsional moment. This could indicate stability failure considering the analysis terminates once the peak load has been reached.

3.2.3   Stress Distribution

With no axial load applied to the cross-section, it was observed that yielding occurred simultaneously on both sides of the web. However, when the member is subject to significant axial compression, the tension side of the web yields prior to the compression side. This effect is amplified at high levels of axial load and is explained by the stress states shown in Figure 3.7.
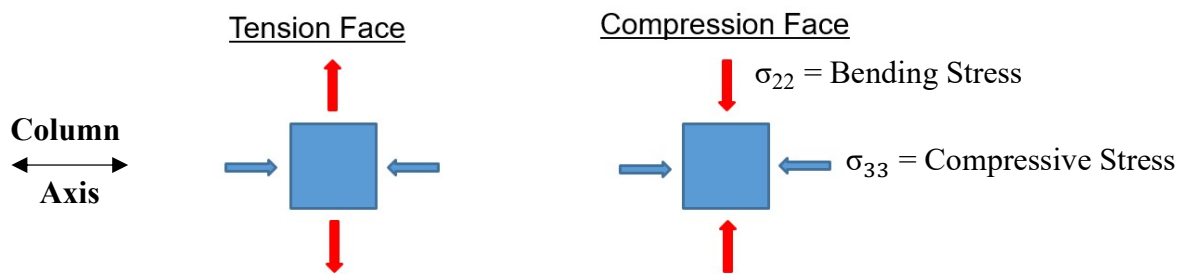

Figure 3.7: Web Surface Stress States

The stress combination on the tension face of the web results in a higher von Mises stress compared to the force combination on the compression face. Therefore, a higher applied moment is required to yield the material on the compression face of the wide-flange column web.

Bending stress measurements were taken from the integration points at the yielding location and plotted through the thickness of the web. All eight integration points in the selected elements showed an effectively linear distribution through the web thickness up to first yield, which is consistent with the assumptions of Equation 2-17. The yield location is highly localised beneath the pressure loads and is accompanied by high stress gradients in both the longitudinal and through-thickness directions. This results in a notable difference between the values at the element integration points and those at the associated nodes. Given that ABAQUS calculates stress and

strain at the integration points and averages them to the surrounding nodes, all values were taken from the integration points rather than the nodes.

3.2.4 Effective Width

The effective width defined by Equation 2-14 has been shown to predict the width of web that is mobilized to resist the localized torque when no axial load is present. However, the addition of axial load decreases the bending stress required to cause yielding, creating a need for further research to see how axial stress impacts the bending stress distribution around the connection region. The effective width is readily visualized in Figure 3.8, which plots the bending stress of a W250×89 member at first yield with axial loads ranging from 0 to 75% of its nominal compressive yield capacity. The stress is plotted along the full length of the member at the web surface near the flange–web junction where initial yielding takes place. The effective width refers to the region around midspan of the member where the majority of bending stress develops on the web to resist the applied torque.

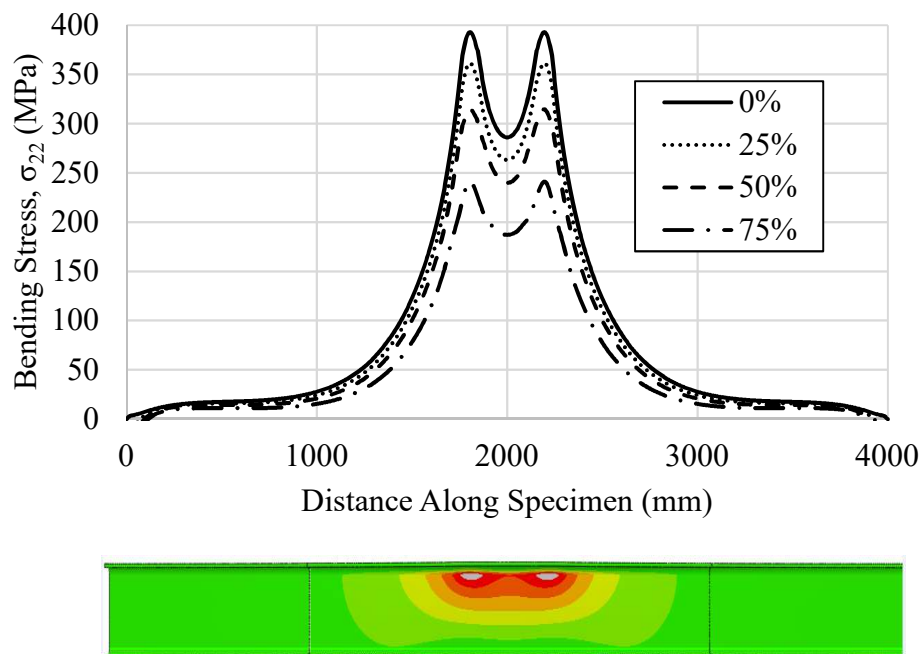Figure 3.8: Web Surface Bending Stress at First Yield Under Varying Axial Load (Surface Stress Contour Plot Inset)

A consistent reduction in maximum bending stress can be observed in Figure 3.8 as the axial stress in the member increases. This is accompanied by a small reduction in effective width, which is most apparent between 50% and 75% axial load. This indicates the effective width is not a strong

function of axial load, and does not account for the nearly 20% under-prediction of the yield moment obtained when Equation 2-17 is compared to the numerical results of Ahmad et al. (2016). The contour plot and bending stress distribution show that the localized nature of the web restraint is consistent with the predictions of Equation 2-14. This suggests the length of the member does not impact connection strength unless the effect of the end restraints encroaches on the highly stressed region around the torsional load.

3.2.5 Bending Stress

Table 3-5 shows a comparison of the bending stress predicted by Equation 2-17 and the maximum tension-surface bending stress obtained at the yielding location from ABAQUS. The reported values were obtained from the integration points at the yield location.

Table 3-5: Bending Stress Comparison

Section	Axial Load (% of Nominal Yield Capacity)	ABAQUS (MPa)	Based on Equation 2-17 (MPa)	Equation 2-17 Error (%)
W250×89	25	348	298	-14.4
	50	302	228	-24.8
	75	225	135	-40.0
W360×91	25	349	298	-14.6
	50	293	228	-22.2
	75	223	135	-39.5
W360×162	25	352	298	-15.3
	50	290	228	-21.4
	75	225	135	-40.0

Equation 2-17 consistently under-predicts the bending stress mobilized on the tension side of the web at first yield. The difference between the ABAQUS output and predicted values increases with increasing levels of axial load. This discrepancy can be partially explained by investigating the major stress components of a W250×89 member derived from the finite element analysis at first yield under 0% axial load, shown in Figure 3.9.
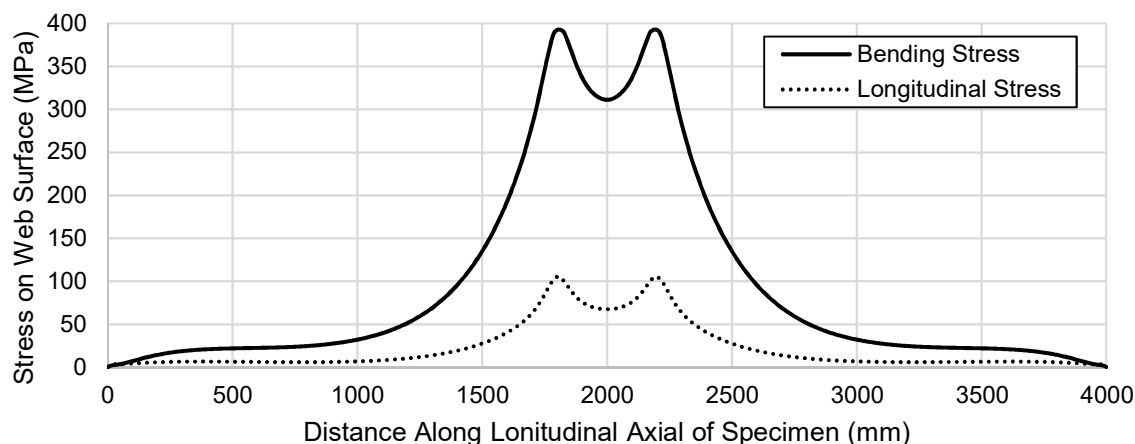
Figure 3.9:W250×89 Stress Components Under Zero Applied Axial Load

As seen in Figure 3.9, the bending stress exceeds the yield stress of the material (350 MPa) by an appreciable amount and the longitudinal stress that can develop is over 100 MPa without any applied axial load. The axial stress is tensile on the tension face of the web, which opposes the bending stress in the von Mises equation, thus allowing more bending stress to develop before yielding occurs. This longitudinal stress develops due to Poisson's ratio interactions. As the torsional moment is applied, the elements on the flexural tension face of the web would elongate in the y-direction (Figure 3.10), causing contraction in the other two principal directions if unrestrained. However, continuity of the web restrains deformation in the z-direction (Figure 3.10), causing a longitudinal tensile stress to develop on the critical side of the web.

The longitudinal stress on the opposite side of the web is compressive due to the reversed bending stress. Considering these forces add to the applied axial load on the compressive side of the web and oppose the axial load on the tensile side, it was questioned whether yielding could initiate on the compression side of the web at low levels of axial load. This was investigated with two additional models by analyzing the yield location of a W250×89 member subject to 5% and 10% of its nominal axial yielding capacity. In all numerical tests, yield initiated on the tension side of the web, indicating the stress developed from Poisson's ratio was not enough to offset the effect of the different stress states in Figure 3.7.

To validate the assumption regarding the longitudinal stress, generalized Hooke's law, given in Equation 3-1, was evaluated for three models. Individual stress components were taken from the integration points of elements at the yielding location and used to calculate the longitudinal stress,

σ33, that would develop due to Poisson's ratio. These values were compared to the ABAQUS outputs and are summarised in Table 3-6. The subscripts associated with the principal stresses and strains in Equation 3-1 correspond to the axes shown in Figure 3.10, and ν represents Poisson's ratio.

$$\varepsilon_{33} = \frac{\sigma_{33}}{E} - \frac{\sigma_{22}\nu}{E} - \frac{\sigma_{11}\nu}{E}$$

3-1

Table 3-6: Longitudinal Stress (σ_{33}) Comparison

Model	ABAQUS (MPa)	Hooke's Law (MPa)	% Difference
W250×89	115.7	118.9	2.75
W360×91	123.6	121.6	1.66
W360×162	116.9	116.2	0.58

The good correlation between the manual calculations and numerical results implies that the main source of the longitudinal stress has been identified. Worth noting is that the longitudinal strain (ε_{33}) and through-thickness stress (σ_{11}) are both small and therefore the magnitude of σ_{33} is largely dependent on the applied bending stress, σ_{22}.

3.3 Parametric Comparisons

The parametric study showed the effective width is not a strong function of axial load and does not account for the large underestimate in strength that is obtained by using Equation 2-17. The main source of error between Equation 2-17 proposed by Ahmad et al. (2016) and numerical simulations is rooted in the bending stress prediction, where due to Poisson's ratio interactions a significant axial stress develops at the yielding location that is not accounted for in previous research. This effect can be incorporated in the design equation by solving for the initial yield moment based on a von Mises stress interaction where the axial load is a combination of the applied compressive stress and an additional stress caused by the torsional moment, as shown in Figure 3.10, where the axial force P is positive in compression to match the direction of the axial load investigated in the current study, but stress is positive in tension. The assumed stress interaction shown in Figure 3.10 eliminates through-thickness stresses (σ_{11}) from the definition of the axial stress (σ_{33}) because it had virtually no impact on the overall longitudinal stress that develops from the torsional moment and simplifies the equation considerably.

$$\sigma_{22} = \frac{6M}{b_{eff}w^2}$$

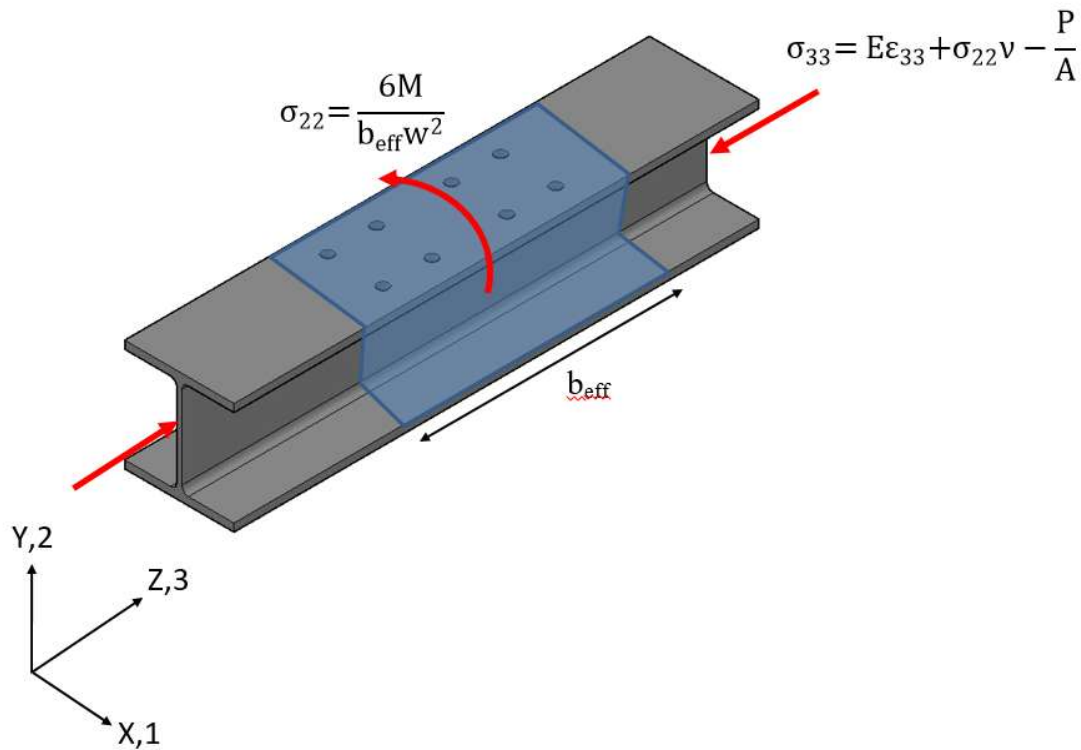$$\sigma_{33} = E\varepsilon_{33} + \sigma_{22}v - \frac{P}{A}$$

Figure 3.10: Assumed Von Mises Stress Interaction

By taking the general von Mises equation shown in Equation 3-2 and assuming the only non-zero components are the bending stress (σ_{22}) and axial stress (σ_{33}), and setting the von Mises stress equal to the yield strength of the material, F_y, Equation 3-3 is obtained by utilizing the additional relationships given in Figure 3.10.

$$\sigma_{vm} = \sqrt{\frac{(\sigma_{11} - \sigma_{22})^2 + (\sigma_{22} - \sigma_{33})^2 + (\sigma_{33} - \sigma_{11})^2 + 6(\sigma_{12}^2 + \sigma_{23}^2 + \sigma_{31}^2)}{2}} \qquad \text{3-2}$$

$$M = \frac{b_{eff}P(-1+2v)w^2 + A\left(b_{eff}E\varepsilon_{33}(1-2v)w^2 + \sqrt{\frac{b_{eff}^2(6AE\varepsilon_{33}P - 3P^2 + A^2(-3E^2\varepsilon_{33}^2 + 4F_y^2(1+(-1+v)v))w^4}{A^2}}\right)}{12A(1+(-1+v)v)} \qquad \text{3-3}$$

Equation 3-3 has several drawbacks when considering it as a design equation to predict the initial yield moment. The equation is complex, and the longitudinal strain (ε_{33}) that develops due to Poisson ratio interactions when a torsional moment is applied is difficult to determine in a design scenario. The magnitude of the longitudinal strain is a function of member geometry and end restraint. Continuity of the web does not perfectly restrain deformations in the longitudinal

direction, meaning small longitudinal strains can develop that decrease the axial stress that develops from the torsional moment. By assuming the longitudinal strain (ε_{33}) is zero, Equation 3-4 is obtained, which assumes a Poisson's ratio of 0.3 and Young's modulus of 200,000 MPa. All numerical simulations found the longitudinal strain to be very small and the difference in the moment prediction based on the actual strain and zero strain is less than 5% for the numerical tests shown in Table 3-7 where Equation 3-4 results in a lower initial yield moment in all cases.

$$M_y = \left| \frac{0.4\frac{P}{A} - \sqrt{3.16F_y^2 - 3\left(\frac{P}{A}\right)^2}}{1.58} \right| \frac{b_{eff}w^2}{6} \qquad 3\text{-}4$$

Equation 3-4 is less complex compared to Equation 3-3 and only contains variables that are easily obtained in a design scenario. The expression bound in absolute value symbols represents the bending stress that develops at first yield. This is compared with the bending stress predicted by Equation 3-3 and numerical analysis results for three standard sections in Table 3-7. The bending stress and longitudinal strain taken from ABAQUS were obtained from the integration points at the yielding location.

Table 3-7: Bending Stress Comparison with Poisson's Ratio Effects

Section	Axial Load (% of Nominal Yield Capacity)	ABAQUS (MPa)	Based on Equation 3-3 (MPa)	Based on Equation 3-4 (MPa)	Based on Equation 2-17 (MPa)
W250×89	25	348	361	360	298
	50	302	302	300	228
	75	225	207	202	135
W360×91	25	349	363	360	298
	50	293	305	300	228
	75	223	211	202	135
W360×162	25	352	361	360	298
	50	290	302	300	228
	75	225	207	202	135

Strain values used to calculate the bending stress predictions of Equation 3-3 shown in Table 3-7 were obtained by taking the longitudinal strain at the yielding location for numerical simulations where the member is subjected to 0% axial load with a torsionally fixed boundary condition. This was done to isolate the strain caused by the torsional moment and avoid influence from the applied compressive stress. This isn't perfectly accurate as it does not consider the additional restraint that

is provided by the axial load when the torsional moment is applied; however, the additional restraint from the axial load would only decrease the longitudinal strain which would lead to values closer to what is obtained in Equation 3-4. Both equations agree with the results of numerical simulations; however, Equation 3-4 does not require quantification of the longitudinal strain, which is difficult to do in a design situation. It also provides a lower initial yield moment compared to Equation 3-3, which is conservative when considering the connection strength.

Overall, the bending stress predictions of Equation 3-3 and Equation 3-4 are very similar, where both equations fit the results obtained from numerical simulations quite well. Notably, Equation 3-4 does not exhibit the large underestimate of bending stress at high levels of axial load that was found in predictions using Equation 2-17. This gives confidence that the assumptions leading to Equation 3-4 better capture the true strength of the column under the given loading scenario. Full-scale testing is required to confirm this.

4 Full-Scale Testing

Full-scale testing was needed to validate the results obtained from numerical simulations and evaluate the effectiveness of the proposed strength and stiffness equations. The beam-to-column weak–axis moment connection tested in the lab was designed in accordance with as-built pipe rack structures to ensure the laboratory setup accurately represented framing systems used in industry. To develop a robust design equation that is applicable for a wide range of standard sections, both cross-sectional geometry and applied axial load were varied throughout the testing program.

4.1 Test Matrix

The primary focus was to select a range of wide flange members that capture the behaviour of most standard sections commonly selected to resist this kind of loading scenario. Based on the findings of Ahmad et al. (2018), the most influential geometric factor that affects the torsional response of the wide-flange column is the ratio of the torsional stiffness of the flange to the bending stiffness of the web. Other factors such as lab space, load frame capacity, and safety concerns were also considered when selecting geometries for testing.

Each wide-flange section was tested at 25, 50, and 75% of its nominal axial yielding capacity to include both light and heavily loaded members. To study the intended loading scenario, it was critical to avoid column buckling during the application of axial load; as a result, all sections were selected to satisfy both local and global buckling limits up to 75% of the nominal axial yielding capacity of the member.

Table 4-1 shows the maximum and minimum stiffness ratio for a range of depth groups commonly used in these kind of loading scenarios. Some sections corresponding to the minimum stiffness ratio were replaced because they did not meet local and/or global buckling limits described above. In these cases, the section with the next closest stiffness ratio that satisfies all buckling limits was selected as a replacement. A W310×129 was also added to the testing program because it is commonly used for this type of loading scenario by the industry sponsor. Deeper sections were eliminated from the testing program because previous research showed section depth has little impact on the strength and stiffness of the column. Moreover, deep sections are more likely to be selected when in-plane flexural loads are significant rather than axial compression unless they are quite stocky, in which case load frame capacity would become a limiting factor.

Table 4-1: Stiffness Ratios for Depth Groups W250 to W360

Section	Normalized Stiffness Ratio
W250×80	0.71
W250×89	0.66
W310×79	0.71
W310×86	0.89
W310×129	0.73
W360×91	0.8
W360×162	1

The five geometries highlighted in Table 4-1 were selected for testing. The normalized stiffness ratio is obtained by dividing r_1 (Equation 2-10) for each section by the largest r_1 in Table 4-1. This parameter varies from 0.66 to 1.0, which corresponds to more than a 50% increase in this parameter over the course of the full-scale testing program. A summary of the test matrix is given in Table 4-2.

Table 4-2: Test Matrix

Test Designation	Axial Load (%)	Section
SP1-1	25	W250×89
SP1-2	50	W250×89
SP1-3	75	W250×89
SP2-1	2	W310×86
SP2-2	50	W310×86
SP2-3	75	W310×86
SP3-1	25	W310×129
SP3-2	50	W310×129
SP3-3	75	W310×129
SP4-1	25	W360×91
SP4-2	50	W360×91
SP4-3	75	W360×91
SP5-1	25	W360×162
SP5-2	50	W360×162
SP5-3	75	W360×162

4.2   Test Setup

The test setup was designed to facilitate a range of wide-flange columns and applied loads, while accurately representing the loading scenarios encountered in a pipe rack structure. This was done by ensuring adequate support reactions and load paths for all applied forces and cross-sectional geometries selected for laboratory testing. Obtaining the moment–rotation response and

identifying the initial elastic yield moment at the surface of the web was considered the primary objective for each test.

Loading was applied in two steps. In the first stage, axial compression was applied to the test specimen through the MTS 6000 load frame up to the desired level. Using force control to hold the axial stress constant, torsional moment was applied to the column through weak axis bending in a bolted beam-to-column moment connection located at midspan of the test specimen. Weak-axis moment is supplied by a horizontal jack (actuator) that reacts off a stiff reaction frame, as shown in Figure 4.1. The actuator applies compression to the free end of the loading beam, creating weak-axis bending in the member which, in turn, is transferred to the test specimen as torsion applied to the connected flange. Torsional moment was applied to the test specimen until a minimum flange rotation of 0.3 radians was achieved, or until the maximum load capacity of the horizontal actuator was reached. This was selected as the ultimate failure because once the bolted flange undergoes 0.3 radians of rotation, the column web and loaded flange have fully plastified in the connection region and any usable purpose for the member is lost. This level of flange rotation corresponds to over 300 mm of movement at the connection between the actuator and loading beam, which would far exceed out-of-plane deflection criteria for the connected member in most design scenarios.
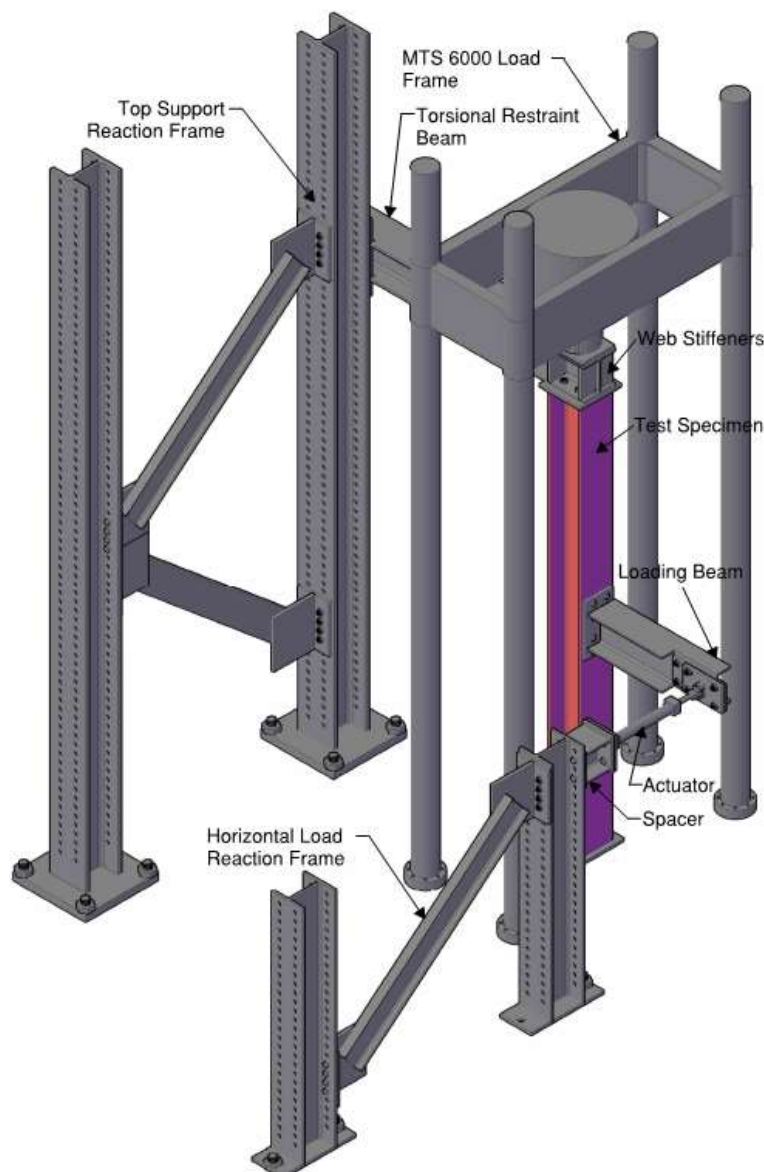
Figure 4.1: Test Setup - Isometric View

The W310×86 loading beam from Ahmad et al. (2016) was utilized in the current testing program. The beam provides adequate weak-axis bending strength to transfer the loads without excessive distortion and the relatively short span allows for significant rotation of the column flange while minimizing the impact of shear on the connection behaviour.

Figure 4.1 to Figure 4.3 detail the full laboratory test–setup. To prevent the actuator of the MTS 6000 (which applies the axial force to the test specimen) from twisting during the application of torsional moment, a W310×129 section was bolted to the MTS actuator on the top flange and

bolted to the test specimen on the bottom flange; this beam is shown as the torsional restraint beam in Figure 4.1. Four 1-inch-thick web stiffeners were fitted to the torsional restraint beam at the loading location to transfer the axial load to the test specimen without compromising the web. The member extends out from the MTS and is clamped to a stiff reaction frame comprising two wide-flange columns connected with single channel braces.
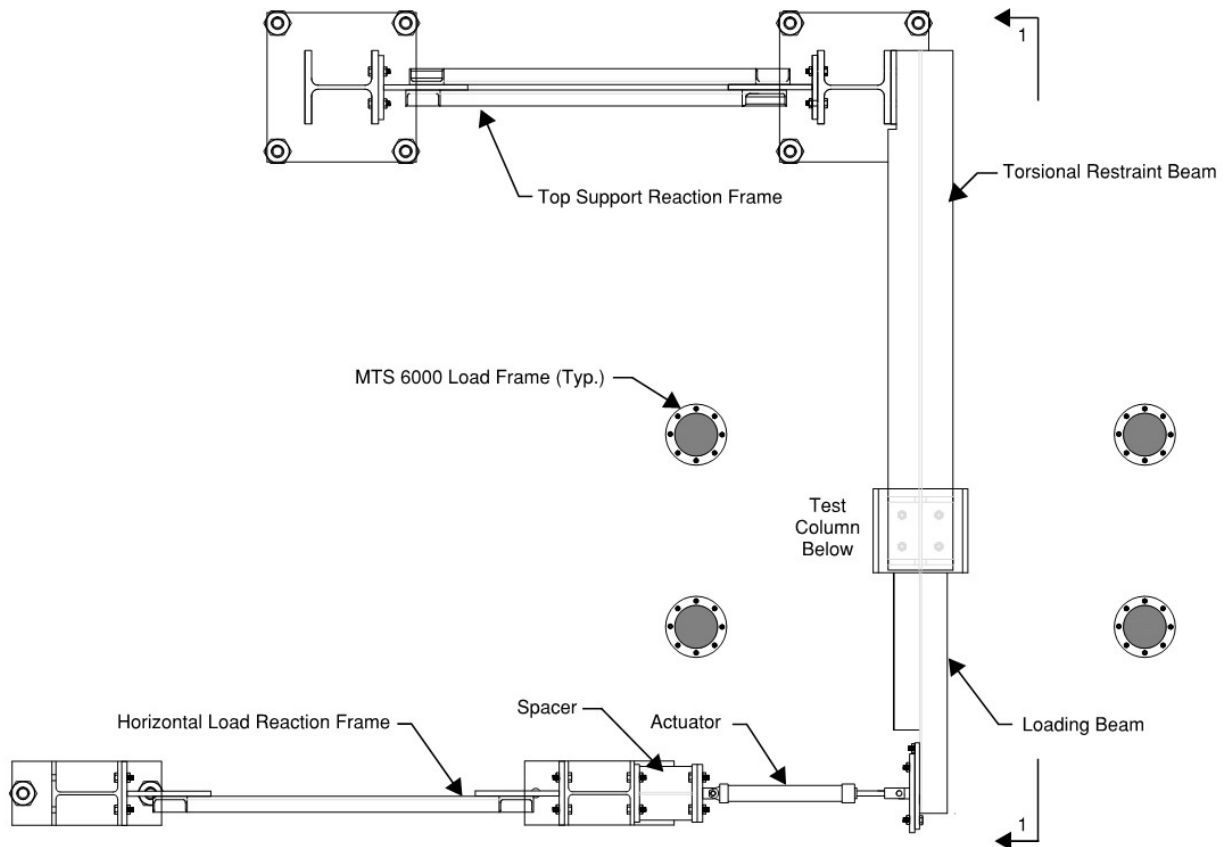
Figure 4.2: Test Setup - Plan View

The actuator is bolted to a spacer connected to the horizontal reaction frame comprising two strong columns connected by a single channel brace. All bolts in the reaction frames were snug tight and checked for movement multiple times throughout the testing program. Similarly, horizontal slotted holes were provided at the connection between the actuator and loading beam to allow adjustments in the actuator until a 90° angle between the loading beam and actuator was achieved. All strong columns were anchored to the strong floor with pre-tensioned rods.
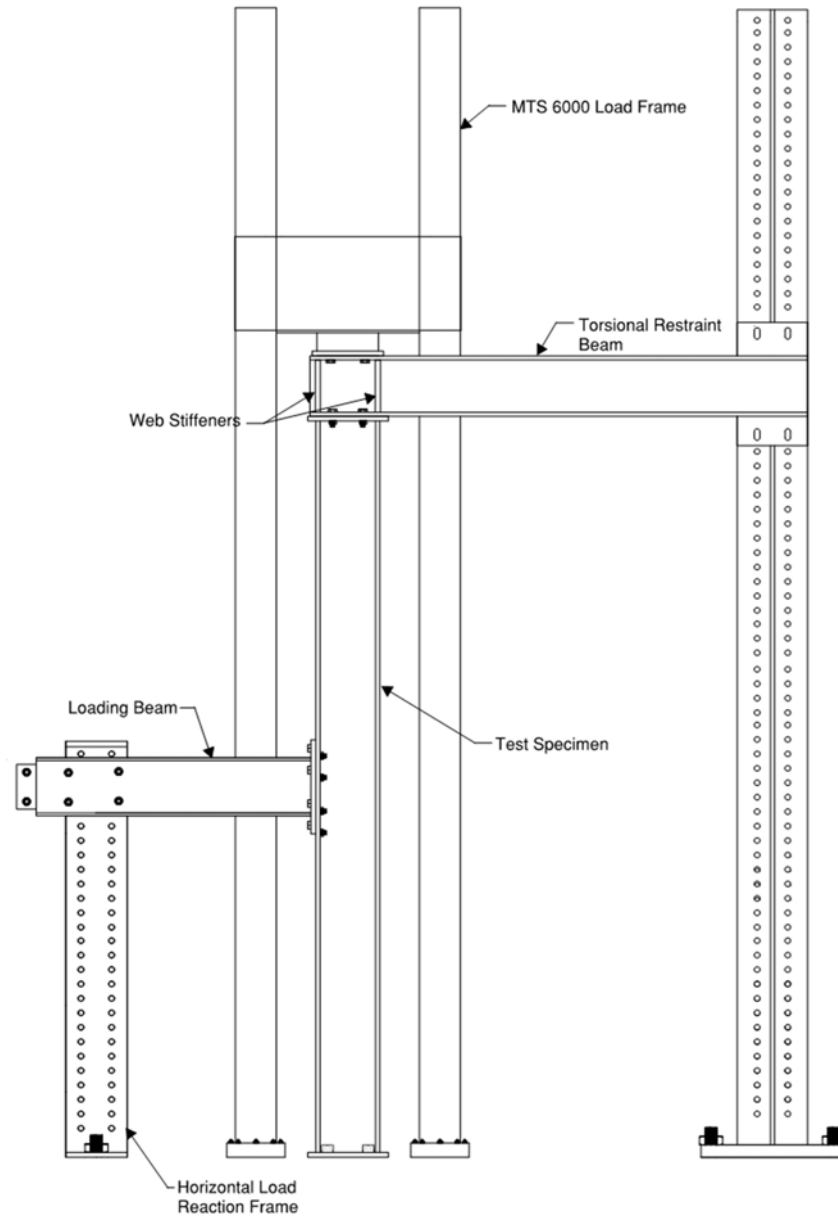
Figure 4.3: Section 1-1 (Fig. 4-2) Elevation View

The process of swapping test specimens is outlined below:

1. Once a test was completed and all horizontal and axial loads were released, the pin connecting the actuator to the loading beam was removed and the actuator was swung clear of the testing area.

2. The loading beam was unbolted from the test specimen and moved away from the column with the aid of chain hoists.

3. The bolts at the top and bottom of the test specimen were removed, and the actuator of the MTS was lifted approximately 25 mm.

4. Using a combination of chain hoists and the 10-tonne crane, the specimen was removed from the MTS load frame and switched with the next specimen.

5. Bolts were placed at the top and bottom of the test specimen to ensure proper alignment before tightening.

6. The MTS cross head was lowered until first contact was made with the baseplate. In all cases, the actuator of the MTS made first contact with the same corner of the baseplate. Shims were then placed on the other three corners of the baseplate to ensure an even distribution of axial load.

7. An axial load of 100 – 300 kN was applied to the test specimen and held constant while the bolts were tightened until snug fit. Once the bolts were tightened, the pre-load was released.

8. The loading beam was then lifted in place using chain hoists and bolted to the test specimen at the midspan. Bolts connecting the actuator to the loading beam and the loading beam to the test specimen were all pre-tensioned using the turn-of-nut method (one-third turn).

9. The actuator was adjusted to make a 90-degree angle with the loading beam and then bolted in place after the axial load was applied to avoid unintended load transfer to the actuator caused by axial deformation of the test specimen.

10. While holding the axial load constant, the actuator was pinned to the loading beam and torsional moment was applied at a rate of 3 mm/min in the elastic region and increased to 6 mm/min once significant yielding of the test specimen had occurred.

4.3 Test Specimens

All test specimens used identical bolt patterns, bolt holes, end plate size and thickness, member length, and weld size. A typical fabrication drawing of a W360×91 specimen is shown in Figure 4.4, details of all specimens can be found in Appendix A. Each member is 3.87 m long with 25 mm thick end plates to allow a direct comparison to the results of the tests by Ahmad et al. (2018).
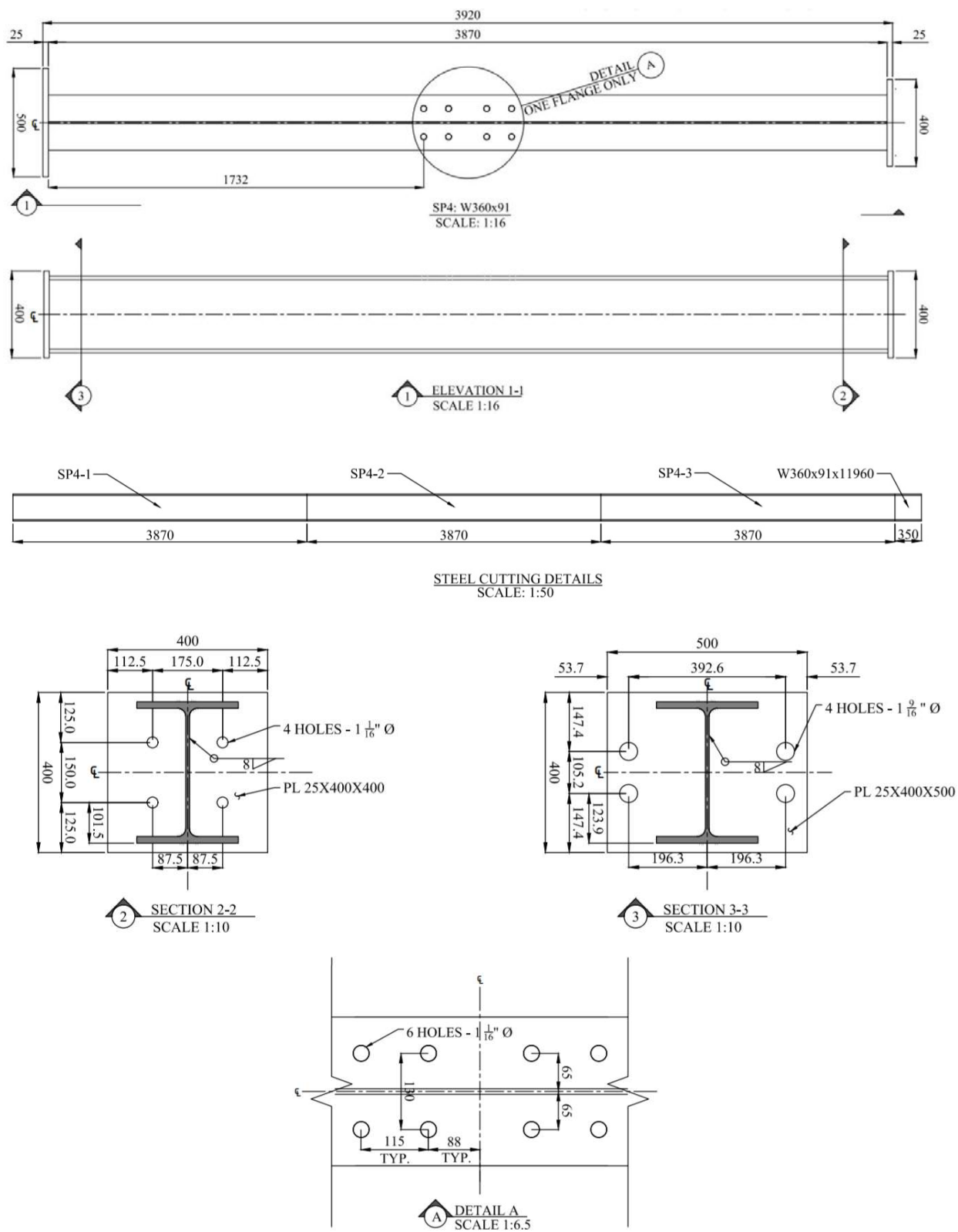
Figure 4.4: Fabrication Drawing of Test Specimen SP4

Each specimen was welded to the end plates with 6 mm fillets all around the section at both ends. At the base of the specimen, four bolts of 1 ¾ inch diameter were selected to match the bolt hole detail at the base of the MTS 6000 load frame. The top of the test specimen was fastened to the torsional restraint beam using four 1-inch bolts (spaced at 175mm × 150mm) positioned to accommodate all test specimens with a single bolt pattern.

The bolt holes at midspan of each test specimen were selected to match the loading beam used by Ahmad et al. (2018). The opposite end of the loading beam was blocked flush with the web to facilitate the connection with the actuator, as shown in Figure 4.1. Geometric constraints caused by hole spacing in the strong floor required that a ¾-inch extension plate needed to be bolted to the web of the loading beam, which effectively lengthened the member allowing the actuator to be bolted to the web of the loading beam.

4.4   Instrumentation

Instrumentation was used to collect data relating to the initial yield moment and bolted flange rotation. Several secondary measurements were taken for verification of primary data and to ensure the testing apparatus behaved as intended.

The applied moment is equal to the net effect of the force components shown in Figure 4.5. The actuator force is resolved into two components acting parallel and perpendicular to the loading beam. The applied force, P, is measured through a calibrated load cell mounted on the piston of the actuator which has a force capacity of approximately 65 kN. The actuator angle was determined by using a cable transducer (CT1) to measure lateral movement of the actuator, as shown in Figure 4.6, which was converted to an angle by hand calculation.

$$M = H*(P_{v,\perp} - P_{h,\perp}) + V*(P_{v,\parallel} + P_{h,\parallel})$$

$$P_{h,\perp} = P_h*COS(\theta_b)$$

$$P_{h,\parallel} = Ph*SIN(\theta_b)$$

$$P_{v,\parallel} = P_v*COS(\theta_b)$$

$$P_{v,\perp} = P_v*SIN(\theta_b)$$

$$P_h = P*COS(\theta_a)$$

$$P_v = P*SIN(\theta_a)$$

Actuator Force, P
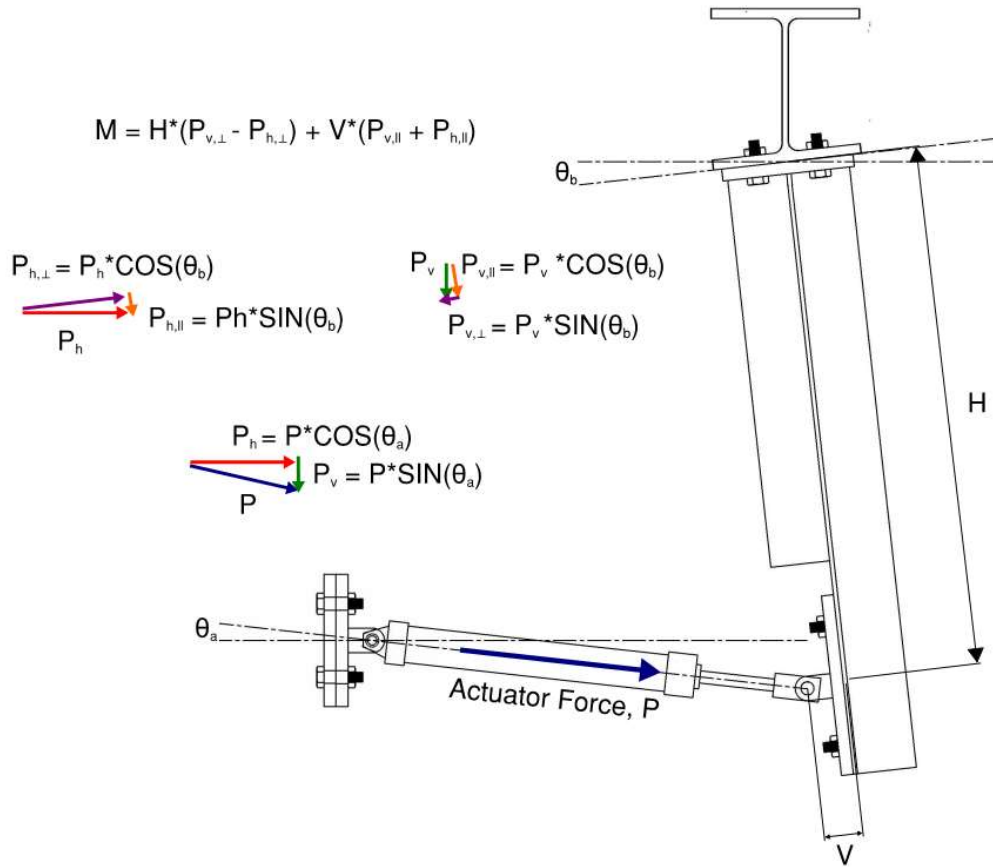
Figure 4.5: Applied Moment Force Breakdown (Adapted from Ahmad et al. 2016)
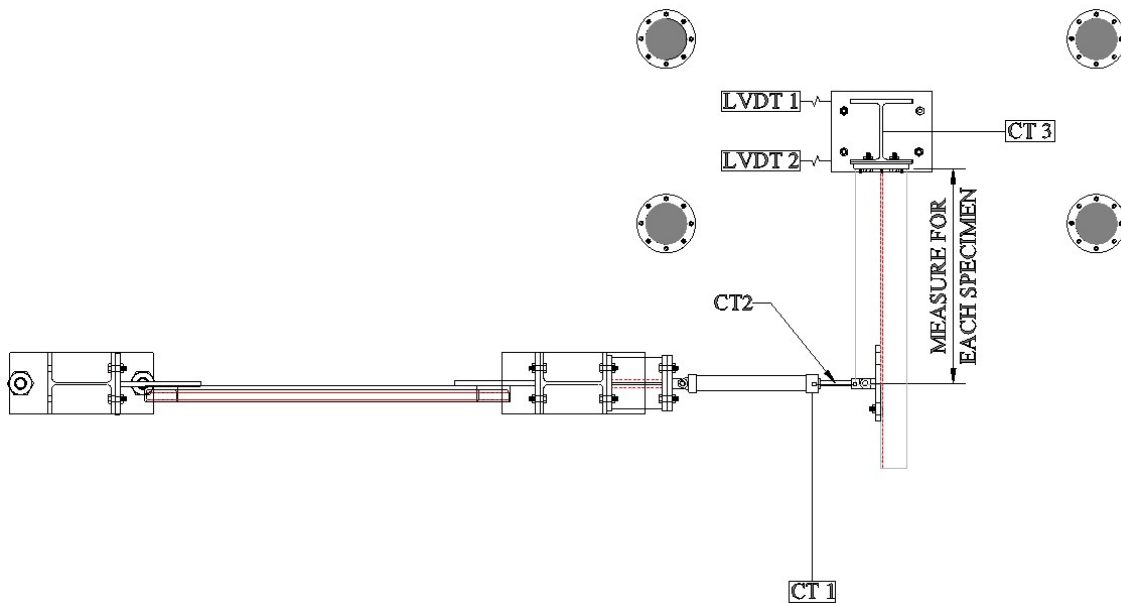
Figure 4.6: Instrumentation Layout

Rotations of the bolted flange of the test specimen were measured directly using digital image correlation (DIC) software. The mill scale on the interior side of the bolted flange was removed on both sides of the web where two camera systems were used to record the rotation of the bolted flange on both sides of the web. The flange rotation obtained with the DIC camera systems were essentially the same regardless of which side of the web was used for calculation, indicating the bolted flange remained straight throughout the test. To optimize test data and reduce preparatory work for each specimen, the bolted flange rotation in the last eight tests was calculated based on one side of the web only with the assumption the flange remained straight.

Linear variable differential transmitters (LVDT) were placed on the baseplate at the top and bottom of the test specimen to measure horizontal movement at the ends of the test specimen during load application, shown in Figure 4.6. A cable transducer located on the torsional restraint beam and additional LVDT (LVDT 2) fitted to the baseplate at the top of the test specimen were added after the first test to determine if the displacement at the top of the test specimen was due to twisting of the member or bolt slip. Figure 4.7 is a photo taken prior to one of the tests, which shows all instrumentation that was utilized in each test.
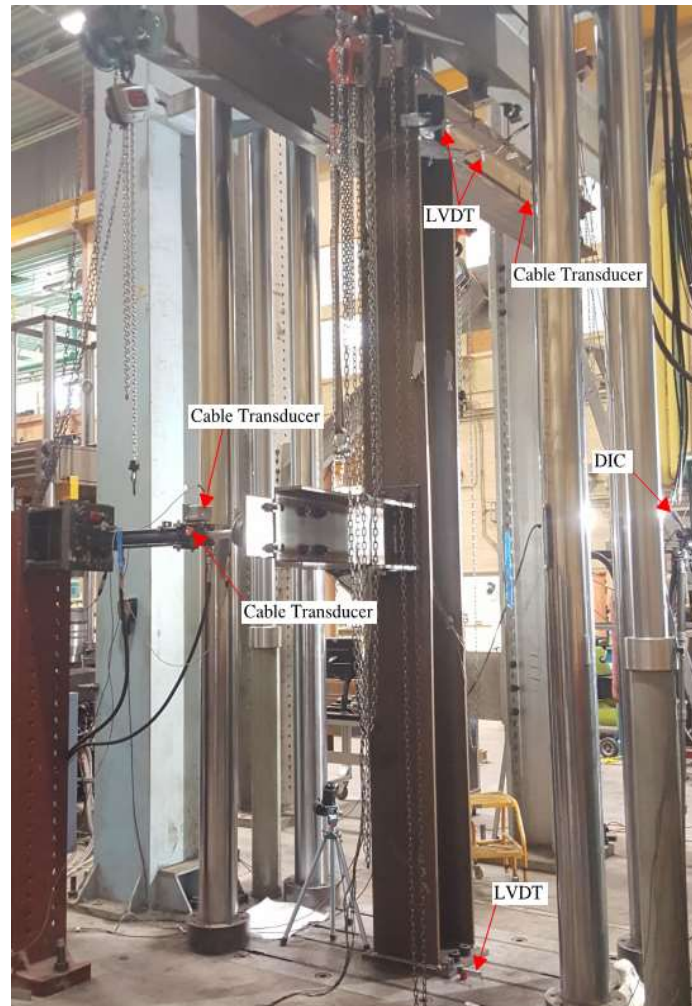
Figure 4.7: Instrumentation Details

The initial yield moment at the surface of the web was measured using strain gauge rosettes placed at the toe of the fillet that connects the web to the bolted flange. Rosettes were placed under the outer bolts, on both sides of the web, making a total of four strain gauge rosettes per specimen, as shown in Figure 4.8.
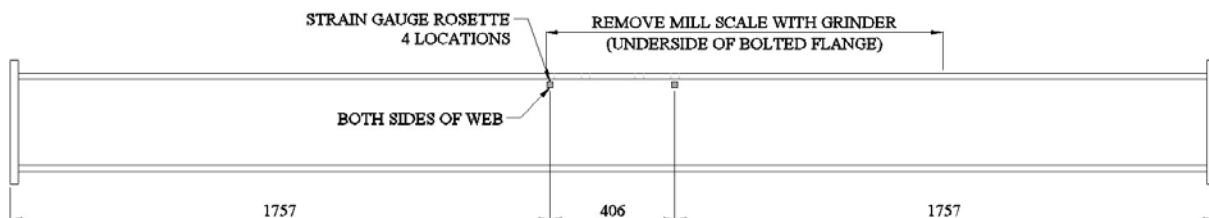
Figure 4.8: Strain Gauge Rosette Details

4.5   Ancillary Tests

Tension tests were carried out in the MTS 1000 to obtain material properties of the test specimens. All steel was specified as CSA G40.21 grade 350W. Columns of the same geometry were cut from a single piece of steel as shown in Figure 4.4 to ensure uniform properties among test specimen. The additional 350 mm long piece of column provided by the fabricator was used to cut tension coupons.

Coupon dimensions conform to general requirements of ASTM A370 "sheet-type" coupons apart from certain coupons taken from the flange of heavier sections, which slightly exceed the 25 mm maximum given in the standard. The coupon dimensions and locations is shown in Figure 4.9 and Figure 4.10. Two coupons were cut in the lateral and longitudinal directions in the web; this location is the site of initial yielding, which means an accurate estimate of material properties in both directions is important given the bi-axial nature of the loading. Due to the difficulty of obtaining the lateral material behaviour in the K-region, an assumption is made that the properties are isotropic when applied to the numerical model. Two coupons were also taken from either side of the bolted flange of the test specimen.
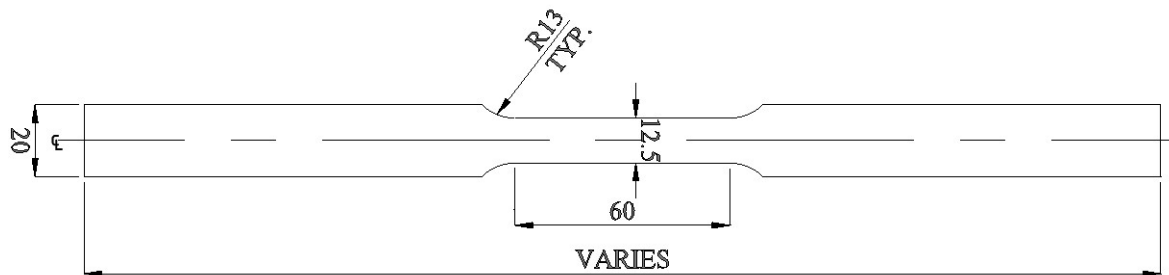
Figure 4.9: Tension Coupon Details
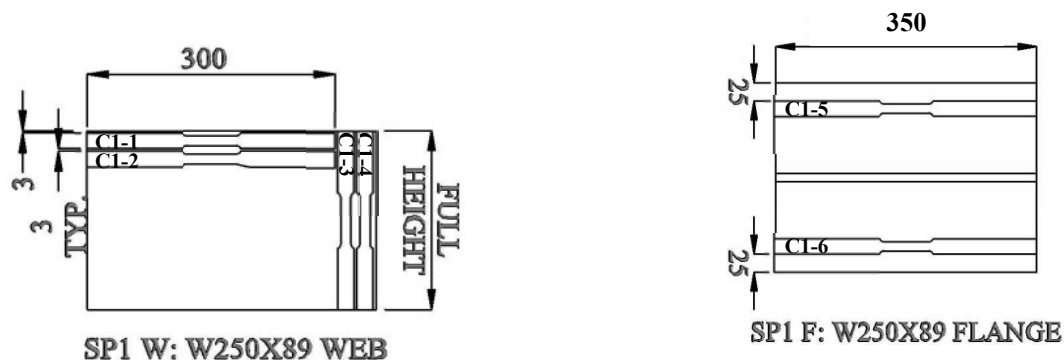
Figure 4.10: Tension Coupon Locations

The loading rate was considerably slower than the maximum values set out by ASTM A370. Displacement control was used to maintain a loading rate of 0.2 mm/min until the onset of strain hardening where the loading rate was increased to 2 mm/min until fracture of the coupon. A minimum of three static points was used to capture the yield plateau with an additional static point taken at the ultimate stress. The first number in the coupon designation (e.g., C1-1) shown in Figure 4.10 refers to a coupon taken from column SP1 and the second numerical defines the location where the coupon was cut.

4.6   Results

Instrumentation used for secondary measurements indicated the test setup behaved as intended. The LVDT at the base of the specimen did not register any significant displacement for any of the tests, indicating that twisting was completely prevented at the base of the column. All tests experienced some bolt slip and twisting at the top of the column, which never exceeded a rotation of 4.5 mrad at the maximum moment and 1.5 mrad at the elastic limit. Measurements of the bolted flange rotation using the DIC software matched well with the results of hand calculations based on the as-built dimension of the test setup.

The readings from the two strain gauge rosettes placed on the same side of the web were generally similar throughout the testing program, indicating that the expected symmetry was obtained. The behaviour was similar during the moment application step and most discrepancies between strain gauges placed on the same side of the web occurred while the compressive stress was applied. Figure 4.11 shows typical rosette readings that were obtained under each level of axial load. The individual strain gauge readings were converted to a von Mises stress by assuming a Poisson's ratio of 0.3 and Young's modulus of 200,000 MPa.
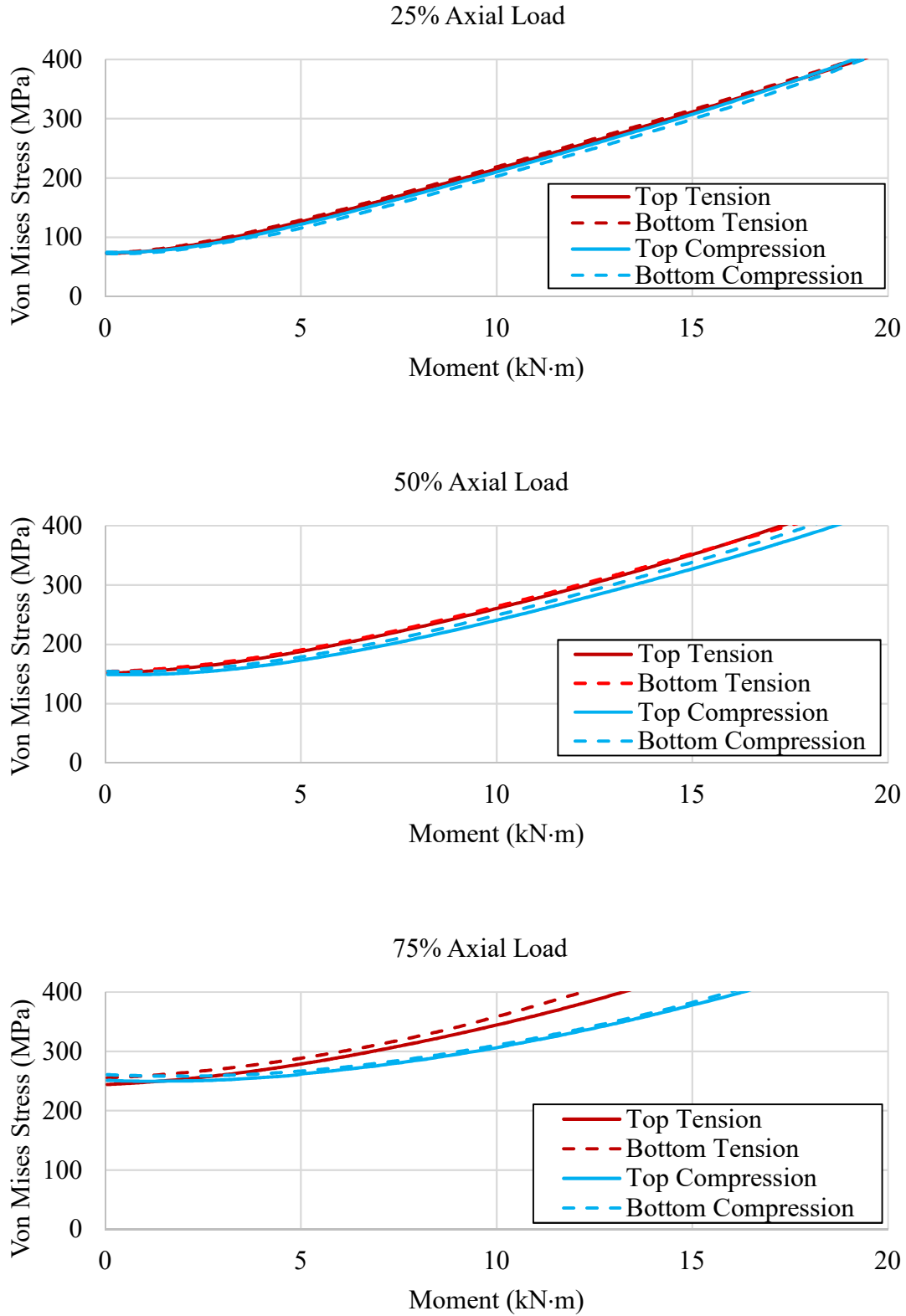
Figure 4.11: W360×162 Von Mises Stress Under Different Levels of Axial Load

Under 75% axial load the rosettes on the south side (tension face) of the web measured a higher von Mises stress than those on the north side (compression face) of the web due to the stress interaction discussed in Chapter 3. Poisson's ratio interactions cause additional axial compression on the compression side of the web and axial tension on the tension side of the web during torsional moment application. This results in opposing axial forces on the tension side of the web and additive forces on the compression side, meaning the net compressive force is larger on the compressive side of the web. At low levels of axial load, this effect compensates for the stress interaction on the tension face of the web (discussed in Chapter 3; Figure 3.7) resulting in similar von Mises stress from all rosettes at any given applied moment. Appendix B contains the strain gauge rosette readings from the other 12 tests. The initial yield moment obtained from the strain gauge rosettes corresponds to a von Mises stress of 350 MPa, which is not the true yield stress of the material. This was done to allow a direct comparison between the design yield moment predicted using Equation 3-4 and the actual moment that develops a von Mises stress of 350 MPa on the cross-section. Assuming linearity until first yield, the design equation should be equally accurate at predicting the applied moment that corresponds to any von Mises stress that is below the yield stress of the material. A summary of the initial yield moment obtained for each test is shown in Table 4-3.

Table 4-3: Initial Yield Moment from Full-Scale Tests

Test Designation	Axial Load (%)	Yield Moment (kN·m)
SP1-1	25	9.75
SP1-2	50	8.74
SP1-3	75	5.49
SP2-1	25	7.67
SP2-2	50	6.95
SP2-3	75	4.88
SP3-1	25	15.01
SP3-2	50	13.84
SP3-3	75	8.93
SP4-1	25	8.31
SP4-2	50	7.12
SP4-3	75	3.29
SP5-1	25	17.25
SP5-2	50	15.16
SP5-3	75	9.47

The results obtained in Table 4-3 conform with expected trends: A clear reduction in yield moment is observed as the axial load increases. The drop in yield moment from test SP4-2 to SP4-3 is notably larger than what is observed for other cross-sections that were tested under the same conditions. Further investigation showed the two rosettes placed on the tension face of the web reported notably different von Mises stresses than obtained in other tests, as shown in Appendix B. This discrepancy may have been caused by inadequate adhesion between the test specimen and strain gauge, considering the same testing procedure was used in other tests that showed close agreement between strains on the same side of the web. The axial stress in SP4-3 was also notably higher than other tests at 75% of the nominal yielding capacity. The strain gauges are expected to report a von Mises stress of 262.5 MPa at 75% of the nominal yielding capacity of the member if the cross-sectional area exactly matches nominal values. In reality, test SP4-3 showed a von Mises stress around 278 MPa prior to the application of torsional moment, which is closer to 80% of the nominal yielding capacity of the member. This explains the sharp reduction in yield moment compared to SP4-2 that showed a compressive stress of 167 MPa, which is less than the theoretical stress (175 MPa) expected at 50% of the nominal axial yielding capacity.

Tension coupon test results are summarised in average values of the yield stress, tensile stress, and Young's modulus are provided for two coupons in the web (Cx-3, Cx-4) and flange (Cx-5, Cx-6) in Table 4-4. The two coupons near the K-region of the web were treated independently due to the change in material property in this region. It was noted in all specimens that coupons near the initial yield location (or "K-region") showed a higher yield stress accompanied by lower ductility. These coupons did not have a defined yield plateau, so the 0.2% offset method was used for identifying the static yield stress. As the coupons moved away from the K-region, a more defined yield point was observed and the specimen reached the strength and ductility that would be expected for the specified steel grade. This is consistent with studies by Kaufmann et al. (2003) where material properties change within the "K-region" of wide flange members due to cold straightening of the member during the manufacturing process. Stress–strain curves for all coupons can be found in Appendix B.

Table 4-4: Tension Coupon Results Summary

Specimen	Coupon Location	Coupon Designation	Yield Stress (MPa)		Tensile Stress (MPa)		Young's Modulus (MPa)	
			Individual	Mean	Individual	Mean	Individual	Mean
SP1 W250×89	Web	C1-1	466.0	-	530.2	-	195,374	-
		C1-2	382.6	-	473.9	-	192,404	-
		C1-3	373.0	367.2	466.0	464.0	233,276	231,005
		C1-4	361.5		462.0		228,733	
	Flange	C1-5	348.9	354.5	458.1	460.8	205,748	204,601
		C1-6	360.1		463.6		203,454	
SP2 W310×86	Web	C2-1	483.0	-	577.3	-	192,443	-
		C2-2	438.5	-	558.1	-	198,412	-
		C2-3	388.6	390.2	539.7	539.8	199,672	200,285
		C2-4	391.8		539.9		200,897	
	Flange	C2-5	402.0	392.9	538.2	537.6	199,380	197,732
		C2-6	383.8		537.0		196,083	
SP3 W310×129	Web	C3-1	462.0	-	559.7	-	198,387	-
		C3-2	380.8	-	517.1	-	194,187	-
		C3-3	352.0	354.9	500.3	501.8	198,959	198,320
		C3-4	357.7		503.4		197,681	
	Flange	C3-5	365.0	383.4	515.0	522.5	211,699	210,063
		C3-6	401.8		530.0		208,426	
SP4 W360×91	Web	C4-1	434.0	-	506.8	-	201,141	-
		C4-2	367.7	-	459.4	-	194,199	-
		C4-3	372.9	374.1	456.2	457.7	206,699	204,987
		C4-4	375.3		459.2		203,275	
	Flange	C4-5	345.8	349.6	444.9	449.3	208,685	204,884
		C4-6	353.4		453.7		201,082	
SP5 W360×162	Web	C5-1	528.0	-	594.9	-	212,042	-
		C5-2	398.0	-	532.8	-	208,709	-
		C5-3	343.7	341.5	508.1	505.6	208,166	203,372
		C5-4	339.3		503.0		198,578	
	Flange	C5-5	357.1	354.0	507.7	508.5	201,651	203,735
		C5-6	350.9		509.3		205,819	

The moment–rotation response was recorded for each test and the relationships are shown in Figure 4.12 to Figure 4.16. The moment–rotation response is consistent across the 15 tests, aside from test SP5-1, shown as the 25% curve in Figure 4.16, where there is notable scatter around 0.2 radians of bolted flange rotation. At this point in test SP5-1, the pressure in the actuator was too low to apply enough force to maintain the loading rate that was specified at the start of the test.

Once the actuator could not apply additional force, the laboratory technicians increased the pump that supplies hydraulic pressure to the horizontal actuator to the maximum rated load capacity associated with the actuator. This resulted in a sudden increase in force as the controller tried to match the actuator displacement with the loading rate. A slow response from the controller meant that the system took several minutes to regulate before typical behaviour was observed around 0.22 rad of rotation.
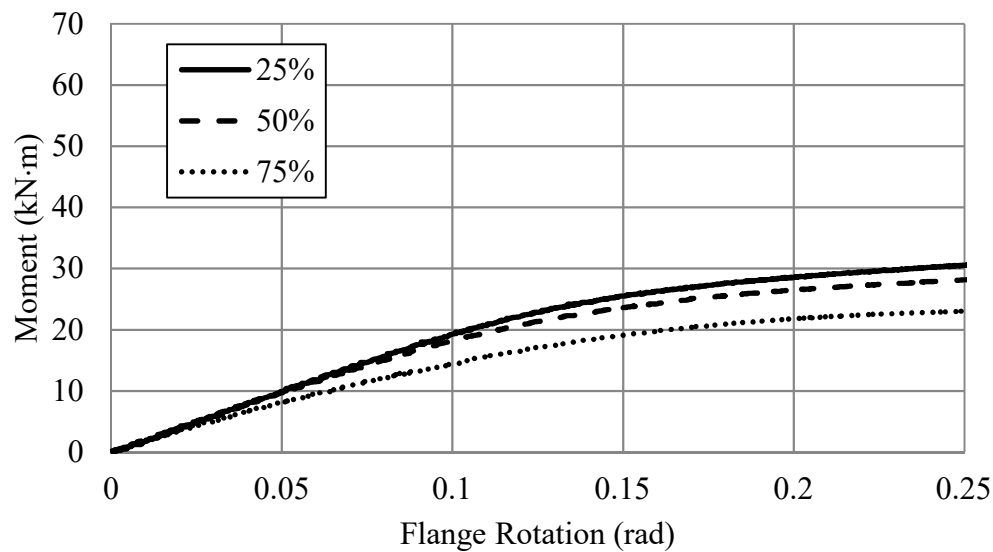
Figure 4.12: SP1-W250×89 Moment–Rotation Response
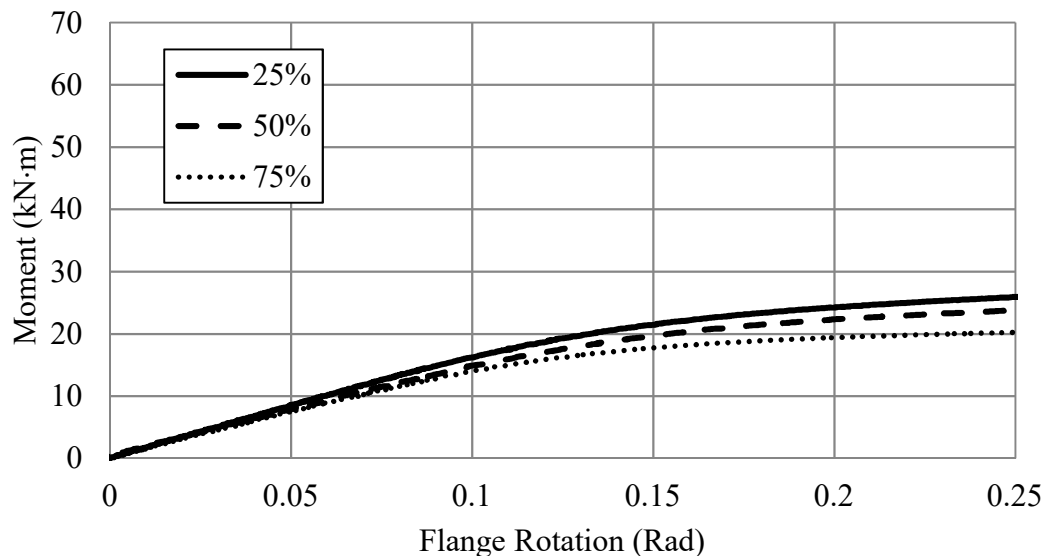
Figure 4.13: SP2-W310×86 Moment–Rotation Response
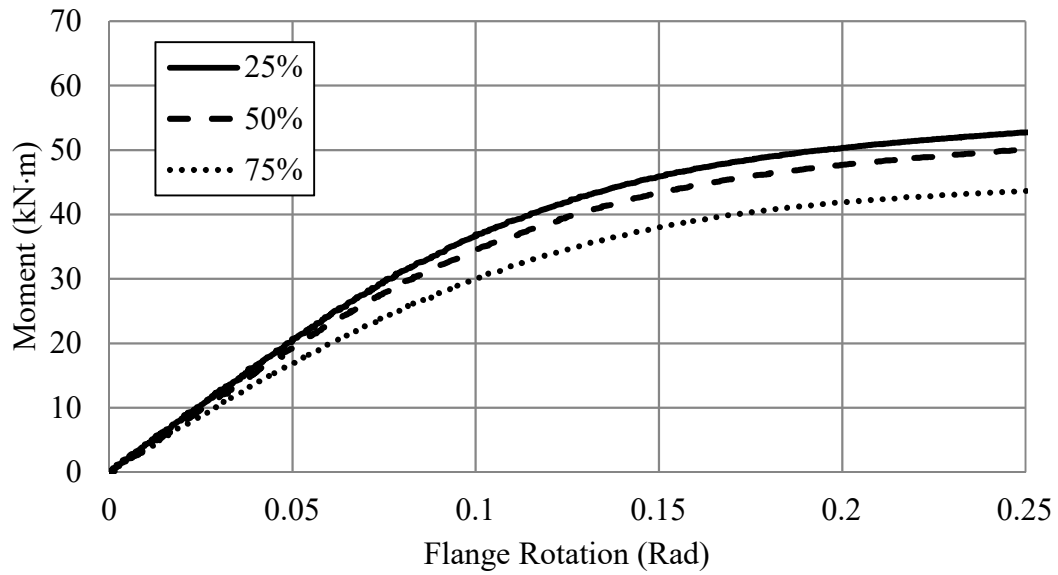
Figure 4.14: SP3-W310×129 Moment–Rotation Response
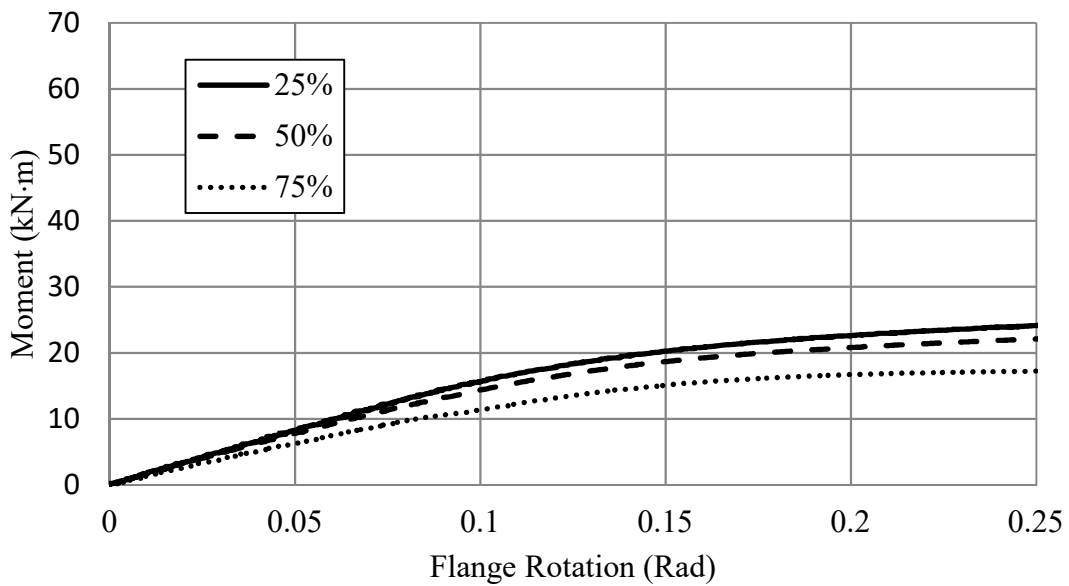
Figure 4.15: SP4-W360×91 Moment–Rotation Response
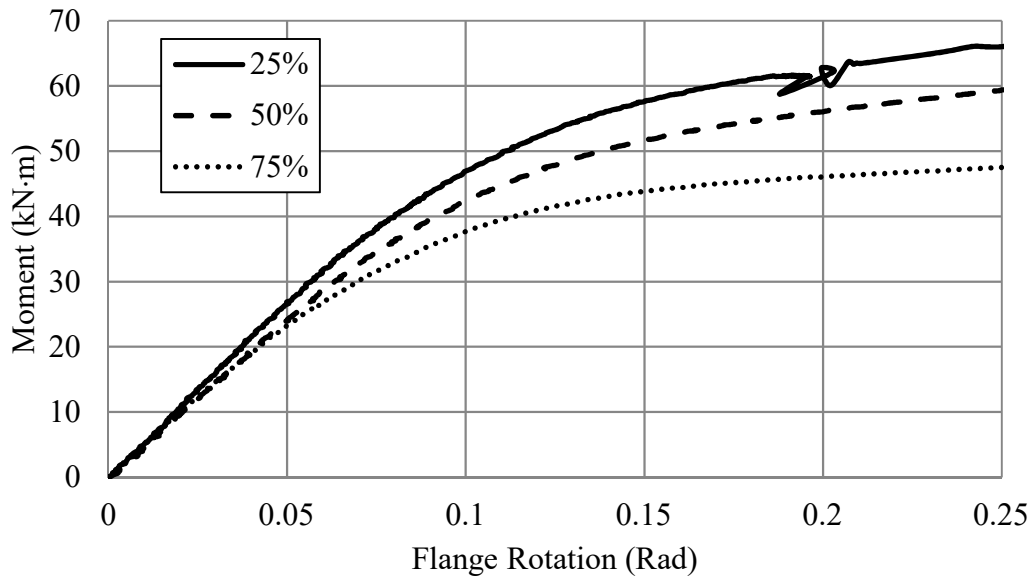
Figure 4.16: SP5-W360×162 Moment–Rotation Response

As the applied axial load increased, a reduction in initial stiffness and initial yield moment was observed in all tests. It was noted throughout the testing program that yielding of the column around the connection region was more severe as the axial load increases. Particularly in the case of 75% axial load, notable yielding of the non-bolted column flange was observed at the end of the test, as shown in Figure 4.17. Yielding in this region is caused by load shedding from the bolted flange, which places additional demand on other parts of the column. This led to nearly complete yielding of the cross-section at the ultimate torsional moment when the column was under 75% of the nominal axial yielding capacity, indicating the testing program pushed the limits of the column strength at the maximum applied torsional moment.

Figure 4.17: Yielding of the Non-Bolted Flange at 75% Axial Load

The reduction in initial stiffness as the axial load goes up is related to a change in boundary condition of the bolted flange. It was noted that as the compressive stress was increased, yielding of the bolted flange near the end of the test specimen was observed by flaking of the mill scale, as shown in Figure 4.18. Yielding in this region decreases the torsional stiffness at the ends of the member leading to the reduction in initial stiffness, which is illustrated in Figure 4.12 to Figure 4.16. This indicates that torsionally fixed boundary conditions are very difficult to obtain when there is significant axial load.

Figure 4.18: Yielding of the Bolted Flange at the Ends of the Test Specimen

Column stability did not govern the behaviour in any tests. Strict displacement limits were placed on the MTS actuator, which used force control to maintain the axial load as the torsional moment was applied. Although small axial deformations occurred during the application of torsional moment, the column maintained its full compressive stress up to the maximum flange rotation in all tests. Some test specimens were 90% utilized when assuming an effective length of 0.5 and over 120% utilized when assuming an effective length of 1.0 according to their factored design capacity (CSA 2014). This suggests it is unlikely column buckling would occur prior to initial yielding due to a torsional moment for any level of axial load that does not exceed the S16 design capacity.

4.7   Numerical Comparisons

4.7.1   Model Verification

Following the full-scale testing program, several modifications were made to the finite element model to better represent the conditions experienced in the laboratory tests. The boundary condition at the loaded end of the member was changed such that rotations about the z-axis (see Figure 4.19 for coordinate axes) were restrained by a linear spring whose stiffness was selected to give the same rotation experienced in the full-scale test at the initial yield moment. Previously models assumed rotations in this direction were fully restrained, which would lead to a higher stiffness than what was experienced in the test.

The material properties were modified to match the results of the tension coupon tests. Because of the notable difference in material properties between the web, flange, and K-region near the root of the fillet, separate material models were developed for each section where average values of static yield stress and modulus of elasticity were used whenever multiple coupons were tested in each region. An isotropic elasto-plastic material model was maintained where a minimum of six points were used to represent the stress–strain curves discussed in Section 4.5. Figure 4.19 shows the region where each material property was used; the K-region extends 36 mm below the root of the fillet, which represents the distance to the centre of coupon C1-2 in Figure 4.10. This is a simplified estimate of the K-region influence as it was noted that the increased strength in this region tended to dissipate rapidly as the coupons were further from the flange–web junction, meaning the maximum benefit from K-region material properties is captured in the model.
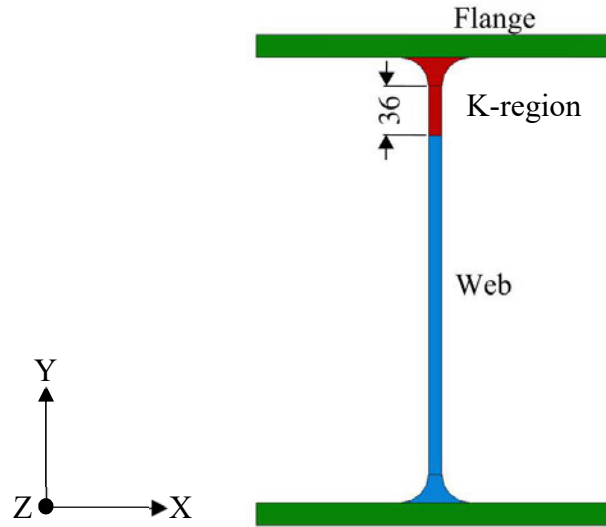
Figure 4.19: Measured Material Property Model Layout

Different boundary conditions were also considered to identify the amount of torsional fixity that was obtained in the laboratory tests. To simulate a torsionally pinned boundary condition, changes to the end restraints and axial load application were needed in the finite element model to facilitate free warping of the column flanges, while ensuring the axial load was applied evenly over the cross-section. This means the rigid body tie connection is no longer appropriate because it forces each node to adopt the same boundary condition as the reference point, meaning that the cross-section deforms uniformly. The torsionally pinned boundary condition was obtained by restraining displacements in the X- and Y-directions for all nodes along the centreline of the member, while allowing free movement in the Z–direction at both ends of the member as shown in Figure 4.20. The axial compressive stress was applied as a pressure load at both ends of the member. In order to ensure stability in ABAQUS during the axial load application, nodes along the web were restrained from moving in the Z–direction at midspan of the member. This method of axial load application is not perfect, as the direction of the axial load changes when the cross-section distorts at the ends of the member. In all tests this distortion was small and was considered acceptable for the purposes of representing the general behaviour that is obtained from a torsionally pinned boundary condition.
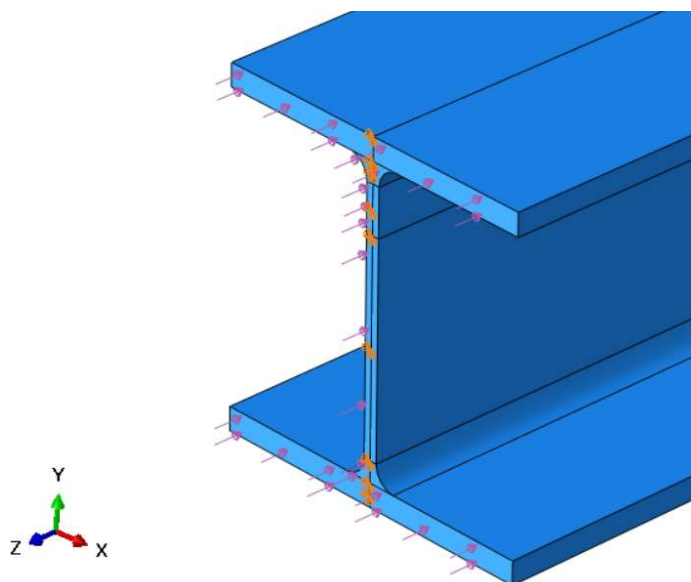
Figure 4.20: Numerical Model Loading and Boundary Condition Changes

4.7.2 Results

The moment–rotation response for the five cross-sections tested in the lab at 25% of their nominal axial yielding capacity are compared to results of numerical simulations in Figure 4.21 to Figure 4.25. The numerical models included measured material properties, nominal cross-sectional dimensions, and both torsionally fixed and torsionally pinned boundary conditions. The remaining laboratory tests were compared to models assuming torsionally fixed boundary conditions which are included in Appendix C.
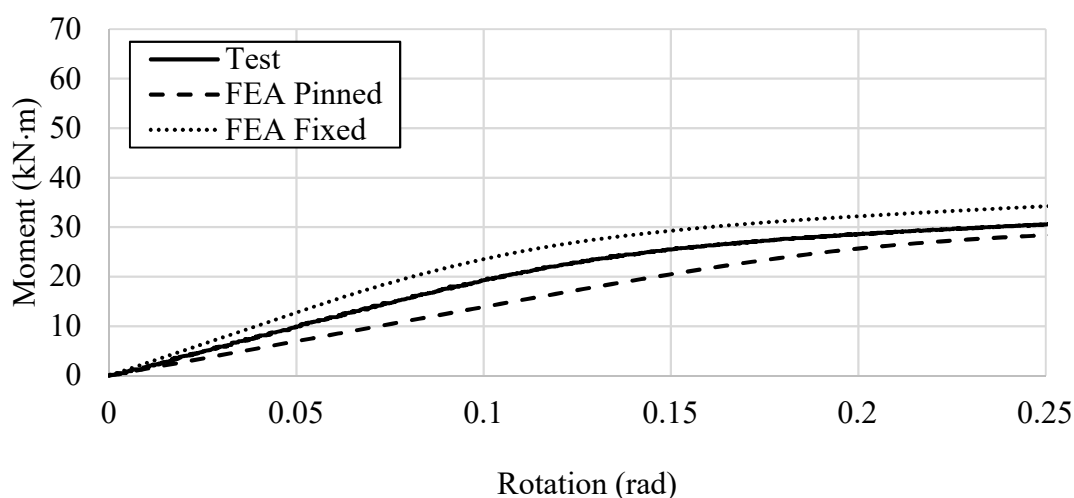
Figure 4.21:Moment-Rotation Comparison of W310x89 Under 25% Axial Load
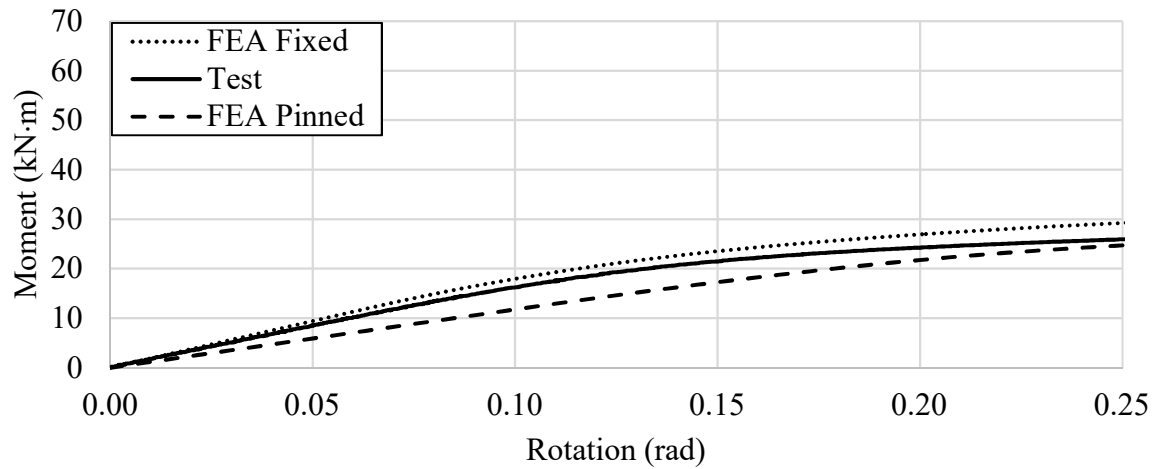
Figure 4.22:Moment–Rotation Comparison of W310×86 under 25% Axial Load
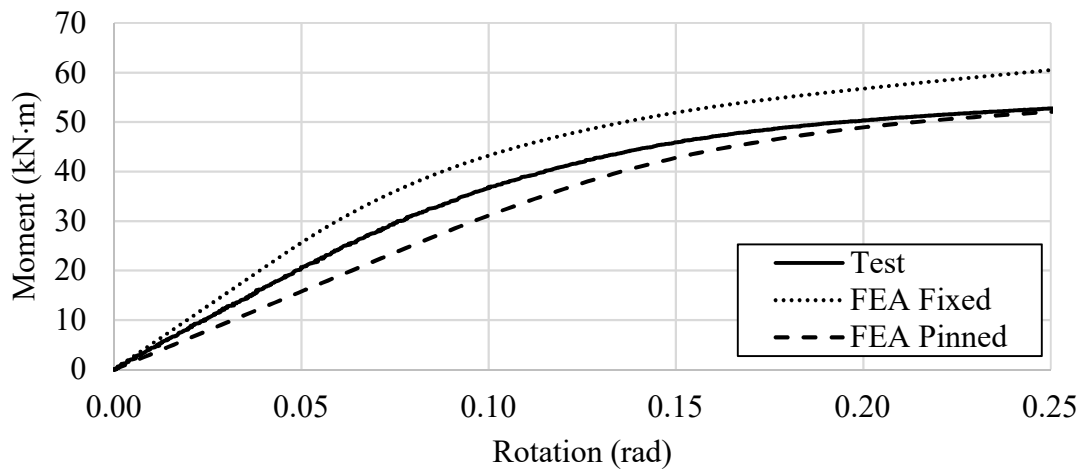
Figure 4.23:Moment–Rotation Comparison of W310×129 under 25% Axial Load
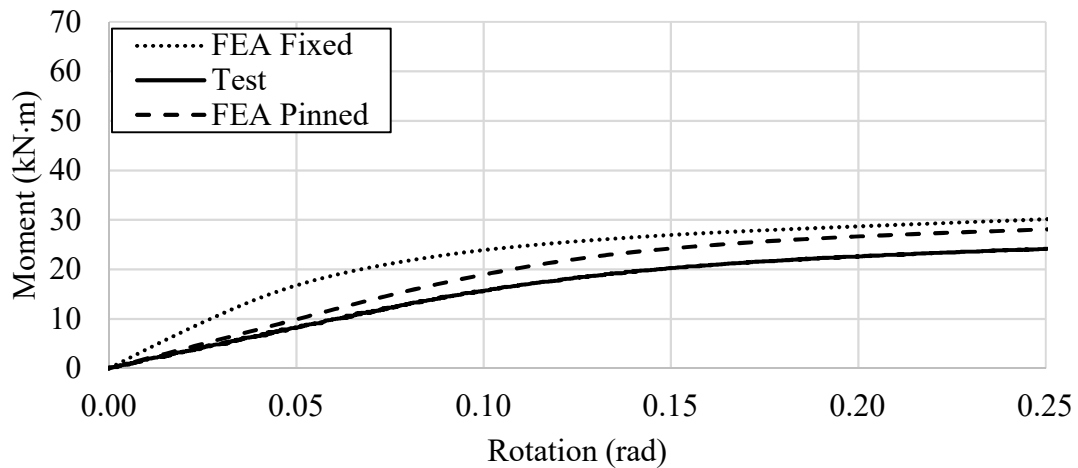
Figure 4.24:Moment–Rotation Comparison of W360×91 under 25% Axial Load
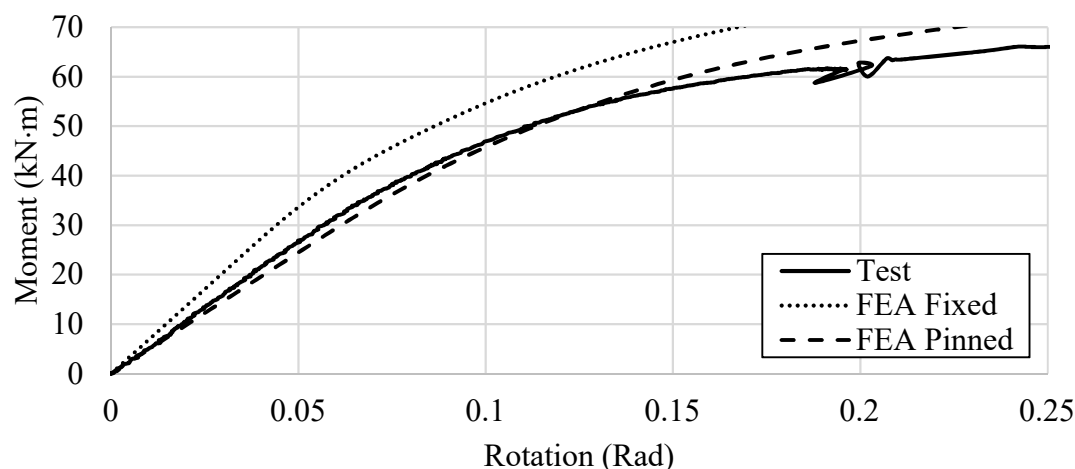
Figure 4.25:Moment–Rotation Comparison of W360×162 under 25% Axial Load

Comparisons between laboratory tests and numerical models suggest semi-rigid end restraints were obtained during the full-scale testing program. As section depth increases, the moment–rotation curves in Figure 4.21 to Figure 4.25 are closer to those of the numerical simulations assuming torsionally pinned boundary conditions. Warping restraint, which defines the level of torsional fixity at the ends of the test specimen, is provided by a combination of the applied axial load and details of the bolted connection at the ends of the test specimen. Since little warping needs to occur to obtain torsionally pinned behaviour, in all cases the restraint was closer to pinned.

The only exception to the results discussed above is the W360×91 under 25% axial load, where near the end of the test the moment–rotation response obtained was more flexible than the numerical analysis assuming torsionally pinned boundary conditions. All laboratory tests for this section resulted in a lower strength and stiffness compared to predicted values. Considering all test specimens for this geometry were cut from a single piece of steel, it is possible the residual stresses in these members was unusually high. This may be caused by significant differential cooling or cold straightening of the member during the manufacturing process. The presence of residual stress explains why all tests showed a small reduction in initial stiffness as the axial load increased that was not captured in numerical simulations.

5 Strength and Stiffness Prediction

Design philosophy and methods for predicting the strength and stiffness of an unstiffened wide-flange member subjected to combined axial load and torsion are discussed in this chapter. Using the results from the numerical analysis and full-scale tests, formulations from previous studies have been adapted to better capture the true connection behaviour under combined loading.

5.1 Maximum Elastic Moment Capacity

The design procedure adopted in the current study is a simplified procedure by Ahmad et al. (2018) who suggested the major resisting mechanism of a wide-flange member subjected to torsion through one flange comes from a combination of localized bending in the web and torsion of the flange. Exact quantification of all components involved in the connection is complex, so the methodology instead predicts the initial yield moment based on the bending strength of the web only.

The resisting moment in the web is assumed to develop a constant bending stress that acts along the length of web, deemed the effective width, defined in Equation 2-12. The additional restraint provided by the flange in torsion is embedded in the definition of the effective width, which is based on the connection length and the ratio of the torsional stiffness of the flange to the bending stiffness of the web (as defined in Equation 2-14). Numerical simulations showed the bending stress that develops in the web is highly localized around the connection and, thus, torsional end restraint has minimal effect on the connection strength unless the member is quite short.

The effect of axial load is incorporated into the yield moment prediction using a von Mises stress interaction to predict the bending stress that develops in the web at first yield given the level of axial load, as described in Chapter 4. Results from the parametric study determined the axial load has limited impact on the effective width. However, Poisson's ratio interactions caused by the torsional moment caused an axial stress to develop at the web surface that was not considered in previous research. Neglecting the longitudinal stress resulted in an underestimate of the connection strength that became more significant as the axial load increased. These stresses were included into the design equation by re-defining the axial stress to be a combination of the applied compressive stress and the axial stress caused by the effect of Poisson's ratio when resisting the

torsional moment. Table 5-1 compares the test-to predicted ratios for Equation 2-17 and Equation 3-4, where the latter equation include the effect of Poisson's ratio interactions.

Table 5-1: Test-to-Predicted Ratio Comparison of Initial Yield Moment

Section	Axial Load (%)	Equation 2-17	Equation 3-4
W250×89	25	1.26	0.96
W250×89	50	1.36	1.03
W250×89	75	1.50	0.96
W360×91	25	1.11	0.90
W360×91	50	1.24	0.93
W360×91	75	1.18	0.63
W310×86	25	1.05	0.83
W310×86	50	1.20	0.90
W310×86	75	1.42	0.94
W310×129	25	1.07	0.91
W310×129	50	1.19	1.01
W310×129	75	1.42	0.97
W360×162	25	0.93	0.80
W360×162	50	1.09	0.84
W360×162	75	1.18	0.78
Mean		1.21	0.89
Coefficient of Variation		0.13	0.11

The yield moments from the laboratory tests in Table 5-1 correspond to the moment at which the strain gauge rosettes showed a von Mises stress of 350 MPa. The true yield stress of the material in the critical region was considerably higher for all sections, as shown by the tension tests described in Chapter 4. However, assuming a yield stress of 350 MPa corresponds to the yield moment that would be predicted in a design scenario given the members were CSA G40.21 350W grade steel. Regardless of the assumed stress, the equation functions the same assuming material linearity is maintained. This means predicting the applied moment corresponding to a von Mises stress of 350 MPa should be equally accurate to predicting the moment associated with a von Mises stress equal to the true material yield stress (which is larger). Another advantage of this type of comparison is that it eliminates the need to consider the changes in yield stress near the yielding location due to manufacturing processes. Based on tension coupon results, the yield stress changes

drastically near the toe of the fillet, meaning that identification of the true yield stress at the yielding location is difficult.

By considering the impact of Poisson's ratio interactions, an overall mean test-to-predicted ratio is obtained that is closer to 1.0 than that obtained using Equation 2-17 suggested by Ahmad et al. (2016). The yield moment predicted by Equation 3-4 does not experience large variations in test-to-predicted ratio at high levels of axial load, which explains the reduced coefficient of variation. However, Equation 3-4 over-predicts the yield moment by an average of 10% which is non-conservative when considering connection strength. Ahmad et al. (2016) noted a limit where the proposed stiffness ratio, r_1, could not effectively predict the length of web mobilized to resist the applied torque. This led to an upper limit on the assumed torsional stiffness of the flange (bt^3) of 3.5×10^6 mm^4. This is consistent with the fact the over-estimate of initial yield moment for the W360×162 is more significant than for other cross-sections in Table 5-1. By applying this limit, the test-to-predicted ratios for the W60×162 in Table 5-1 would change to 0.86, 0.91, 0.84 in order of increasing axial load.

To improve the mean test-to-predicted ratio of Equation 3-4, several geometric variables and combinations of variables were plotted against the test-to-predicted ratio for each test to identify possible trends. The one geometric variable that stood out as most influential was section depth, shown in Figure 5.1. A clear reduction in test-to-predicted ratio is observed as the depth of the section increases. This is supported by the observation that effective widths based on the numerical analyses were slightly smaller for deeper sections. The linear modification factor, ψ, shown in Equation 5-1 is proposed to compensate for this depth effect.
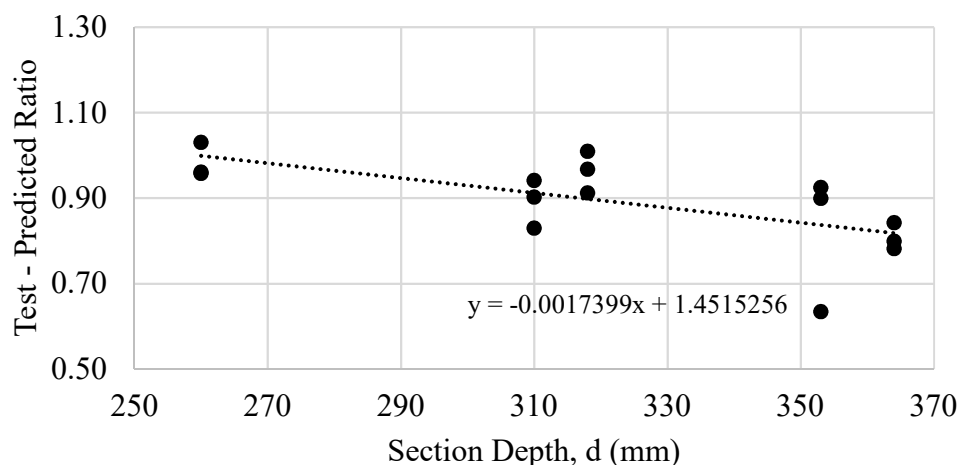
Figure 5.1: Effect of Section Depth on Test-to-Predicted Ratios of Equation 3-4

$$\psi = -0.002d + 1.5 \leq 1.0 \qquad\qquad 5\text{-}1$$

The trendline equation fitted to the data of Figure 5.1 was rounded for simplicity in design and to ensure a slightly more conservative modification factor compared to what is obtained from the trendline in the figure. The upper limit ensures there is no added strength for extremely shallow sections, which have not been studied.

The modification factor, ψ, was applied to the stiffness ratio, r_1, of Equation 2-12 to obtain Equation 5-2. Initial derivations of the stiffness ratio by Ahmad et al. (2018) included section depth, but it was removed due to its minimal impact on the results of the parametric study. This suggests section depth has some impact on the member behaviour, making it a reasonable factor upon which to base the empirical modification suggested in Equation 5-1. Even by applying an empirical factor to the effective width, which itself is also empirical, the overall formulation for the yield moment remains fundamentally based on mechanics. The new test-to-predicted ratios obtained from Equation 5-3, with the effective width determined using Equation 5-2 are given in Table 5-2.

$$b_{eff} = N + \psi r_1 \qquad\qquad 5\text{-}2$$

$$M_y = \left| \frac{0.4\frac{P}{A} - \sqrt{3.16F_y^2 - 3\left(\frac{P}{A}\right)^2}}{1.58} \right| \frac{b_{eff}w^2}{6} \qquad\begin{array}{c} 5\text{-}3 \\ [\text{Eq. 3-4 Repeated}] \end{array}$$

Table 5-2: Test-to-Predicted Ratio Including Section Depth Modifier

Section	Axial Load (%)	Equation 5-3
W250×89	25	0.97
W250×89	50	1.05
W250×89	75	0.98
W360×91	25	1.07
W360×91	50	1.10
W360×91	75	0.75
W310×86	25	0.92
W310×86	50	1.00
W310×86	75	1.04
W310×129	25	1.02
W310×129	50	1.12
W310×129	75	1.08
W360×162	25	0.98
W360×162	50	1.03
W360×162	75	0.96
Mean		1.00
Coefficient of Variation		0.09

The section depth modification factor leads to a notable reduction in the coefficient of variation, which supports the choice of section depth as the variable of influence. Given the positive correlation between test results and predicted values, Equation 5-3 is suggested for predicting the initial yield moment under varying levels of axial load. It provides a conservative strength prediction at first yield, with considerable reserve strength and rotational capacity under a wide range of axial loads. The seven tests conducted by Ahmad et al. (2018) were not used in the development of Equation 5-3. This is because the strain gauges used to identify the initial yield moment were uniaxial, meaning the effect of Poisson's ratio interactions were ignored in the reported initial yield moment. As a form of verification, Table 5-3 summarises the test-to-predicted ratio of Equation 5-3 when it is compared with the results from Ahmad et al. (2018) testing program. If Poisson's ratio interactions had been reflected in the test results, the test-to-predicted ratios would be expected to increase. It should be noted that in cases where the torsional moment is applied near the ends of the column, the effective width may not extend beyond the ends of the column. In the case of an extremely deep connected beam, where the weak axis moment may not be fully transferred in the region between the two flanges, the effective width should be limited to $\psi r_1/2$ on each side of the bolt groups at each flange

Table 5-3: Test-to-Predicted Ratio for Ahmad et al. (2016) Testing Program

Section	Equation 5-3
W310×86	0.88
W410×100	1.14
W250×80	0.82
W360×72	1.12
W310×67	1.06
W410×67	1.12
W310×129	0.96
Mean	1.01
Coefficient of Variation	0.13

The mean test-to-predicted ratio of 1.01 obtained using Equation 5-3 is more conservative than that reported by Ahmad et al. (2018), who obtained a mean test-to-predicted ratio of 0.96 when using Equation 2-13 to predict the initial yield moment. However, the coefficient of variation is notably higher (0.13 instead of 0.04) when using Equation 5-3. Poisson's ratio interactions have minimal impact on the coefficient of variation because no compressive stress was applied in these tests, meaning the yield stress is multiplied by the same constant in all tests to account for the additional strength caused by the 2D stress interaction. This implies the additional scatter is caused by the empirical section depth modifier (ψ) applied to the stiffness ratio in Equation 5-2. Although this indicates the section depth modifier does not perfectly capture the true connection behaviour, it leads to a more conservative yield moment prediction than if it were ignored. The section depth modification factor works well when significant axial load is present and is somewhat conservative without axial load. This aligns with one of the major goals in the current research, which is to develop a unified design procedure that is applicable over a wide range of loading scenarios.

One aspect that was not investigated in the current study is global buckling of the column, potentially induced by the application of the torsional moment. Previous full-scale testing programs did not consider significant axial load in the column, so global buckling was not a concern. However, the torsional moment causes distortion of the column cross-section and could lead to a stability failure prior to reaching its design capacity, which does not consider buckling under combined axial load and torsion applied through one flange. The full-scale testing program in the current study did not observe buckling during any tests. Even after significant yielding and

distortion occurred in the connection region, the column maintained its axial load-carrying capacity until a minimum of 0.3 radians of flange rotation. This suggests the S16 column design provisions are robust enough to account for the small cross-sectional distortion that occurs at first yield. The flange rotation at first yield in the full-scale testing program was similar to the maximum rotation permitted according to standard mill practice defined in ASTM standard A6, which states that the flange rotation for W310 sections and smaller shall not exceed 20 mrad for 300 mm wide flanges and 60 mrad for 100 mm wide flanges. For sections larger than W310, 20 mrad is permitted for 400 mm wide flanges and 40 mrad for 200 mm wide flange. Flange rotations at first yield obtained in the full-scale tests varied from 20 mrad up to 50 mrad.

The presence of residual stresses in the column have not been addressed explicitly in the design equations discussed in this section. These stresses are likely tensile at the initial yielding location and therefore oppose the applied compressive stress in the member, indicating that ignoring these stresses is conservative when considering column strength.

5.2   Stiffness Prediction

The elastic stiffness of a wide-flange member subjected to torsion applied to one flange was originally studied by Milner and Rao (1978) and modified by Yura (2001) and Ahmad et al (2018) to better suit the application being studied in the current research. Equation 5-4 describes the elastic stiffness of the column (K_u) as a combination of the localized web stiffness (K_w) and the overall torsional stiffness of the member assuming localized distortion is prevented (K_s). When full-depth stiffeners are provided at the connection location (i.e., localized distortion is prevented), the web stiffness becomes very large and the column response is controlled by the overall torsional stiffness of the column, K_s. Conversely, when the column is unstiffened, the column response is a combination of full cross-sectional stiffness and local web stiffness.

$$\frac{1}{K_u} = \frac{1}{K_s} + \frac{1}{K_w} \qquad\qquad 5\text{-}4$$

Quantification of K_s is readily obtained using well established elastic torsion theory, discussed in Chapter 2. Formulation of the localized web stiffness developed by Ahmad et al. (2018) is shown in Equation 5-5, where the width of web engaged to resist the applied torque has been calibrated to match the results obtained from numerical simulations. The test-to-predicted ratios comparing

the elastic stiffness of the wide-flange section, K_u, obtained using Equation 5-4 are shown in Table 5-4 for all tests conducted by Ahmad et al. (2018) and the current study, with predicted values based on both torsionally fixed and pinned boundary conditions. The initial stiffness was obtained for each test by dividing the initial yield moment by the corresponding bolted flange rotation.

$$K_w = \frac{3.3E}{h}\left[(N+1.5r_1)\left(\frac{w^3}{12}\right)\right] \qquad 5\text{-}5$$

Table 5-4: Equation 5-4 Experimental Test-to-Predicted Ratio

Section (Axial Load %)	K_u	
Boundary Condition	Fixed	Pinned
W250×89 (25)	0.68	1.25
W250×89 (50)	0.68	1.26
W250×89 (75)	0.59	1.09
W360×91 (25)	0.66	1.05
W360×91 (50)	0.62	0.99
W360×91 (75)	0.52	0.83
W310×86 (25)	0.69	1.17
W310×86 (50)	0.64	1.09
W310×86 (75)	0.63	1.08
W310×129 (25)	0.68	1.17
W310×129 (50)	0.70	1.20
W310×129 (75)	0.63	1.09
W360×162 (25)	0.61	0.94
W360×162 (50)	0.54	0.84
W360×162 (75)	0.64	0.95
Ahmad et al. (2016)		
W310×86 (0)	0.65	1.10
W410×100 (0)	0.73	1.07
W250×80 (0)	0.62	1.15
W360×72 (0)	0.72	1.19
W310×67 (0)	0.75	1.31
W410×67 (0)	0.78	1.23
W310×129 (0)	0.6	1.04
Mean	0.65	1.09
Coefficient of Variation	0.10	0.12

The 22 test results show an experimental stiffness that is between torsionally fixed and pinned, but closer to torsionally pinned in almost all cases. The results exemplify the difficulty in obtaining torsional fixity in real design scenarios. Ahmad et al. (2016) reported around 3 mm of warping displacements for models in his numerical study that were given torsionally pinned end restraints. To prevent this in his laboratory tests, thick end plates and pre-tensioned bolts at the ends of the column were selected, but up to 2 mm of warping displacements were still observed.

No gap at the ends of the member was observed in any tests conducted in the current study; however, significant shimming at the top of the member due to warping of the endplate and torsional restraint beam led to small gaps that exist in parts of the cross-section. At high levels of axial load, the MTS actuator moved nearly 3 mm in the axial direction during the application of torsional moment, which was likely due to warping of the column, which caused the actuator to move in order to maintain a constant axial load. Because of the difficulty associated with obtaining torsional fixity in real structures, it is recommended that designers assume torsionally pinned end restraints to avoid an over-estimate of the elastic column stiffness. It should be noted that this assumption would be slightly unconservative when calculating the design moment transferred from the beam to the unstiffened column.

To better understand the impact of axial load on the initial stiffness, two cross-sectional geometries common to the programs of Ahmad et al. (2018) and the current research were studied. These tests facilitate a comparison of the initial stiffness with axial loads ranging from 0 to 75% of their nominal yielding capacity, as shown in Figure 5.2 and Figure 5.3.
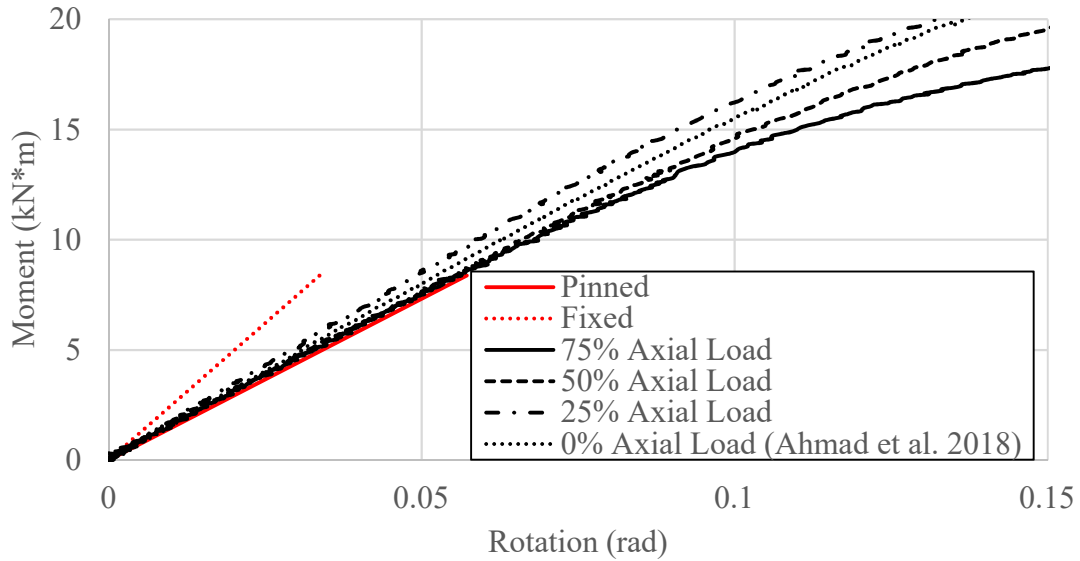
Figure 5.2: W310×86 Moment–Rotation Comparison
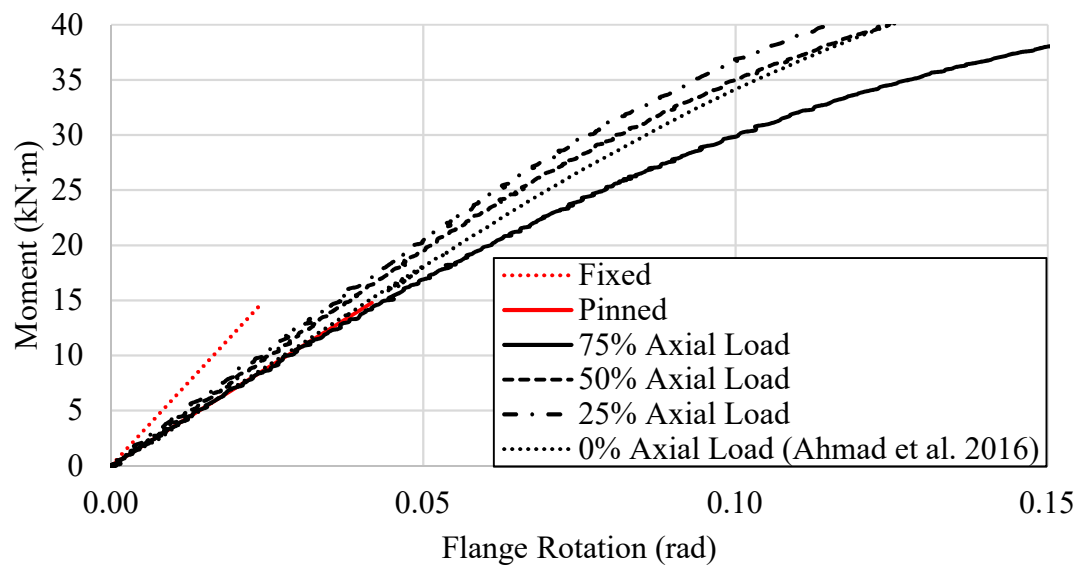
Figure 5.3: W310×129 Moment–Rotation Comparison

For both cross-sectional geometries, the tests with 25% axial load resulted in a higher initial stiffness than the test performed with zero axial load. This is because the applied compressive stress provides additional restraint from warping when the torsional moment is applied, giving end restraints that behave closer to torsionally fixed. At 50% axial load, one member shows a slightly stiffer response than what Ahmad et al (2016) obtained, while the other is slightly more flexible. Both columns show a more flexible response compared to the ones of Ahmad et al. (2016) once the axial load reaches 75%. This trend appears to go against the concept that the compressive stress

helps provide torsional fixity at the ends of the member, but the reduction in stiffness is due to yielding of the bolted flange that was discussed in Chapter 4. Compressive residual stresses in the flange tips may be as high as 30% of the steel yield stress and, coupled with torsional stresses from the applied moment, can result in premature yielding of parts of the cross-section leading to a more flexible moment–rotation response. For cases with high axial load and a low yield strength (e.g., W360×91 at 75% axial load), residual stress could lead to yielding of the flange tips prior to application of any torsional moment, which explains the consistent drop in initial stiffness that is noted for columns under high axial load. This suggests the application of axial load can increase the initial stiffness by restraining warping displacements until it becomes large enough to cause premature yielding on parts of the cross-section due to the presence of residual stresses.

To better capture the impact of axial load on the initial stiffness, Figure 5.4 plots the test-to-predicted ratio of the column elastic stiffness prediction, K_u, calculated using Equation 5-4 against the applied axial load. K_w was determined using Equation 5-5 and K_s was obtained using classical elastic torsion theory. For all tests, the predicted values were calculated assuming torsionally pinned end restraints and nominal cross-sectional dimensions.
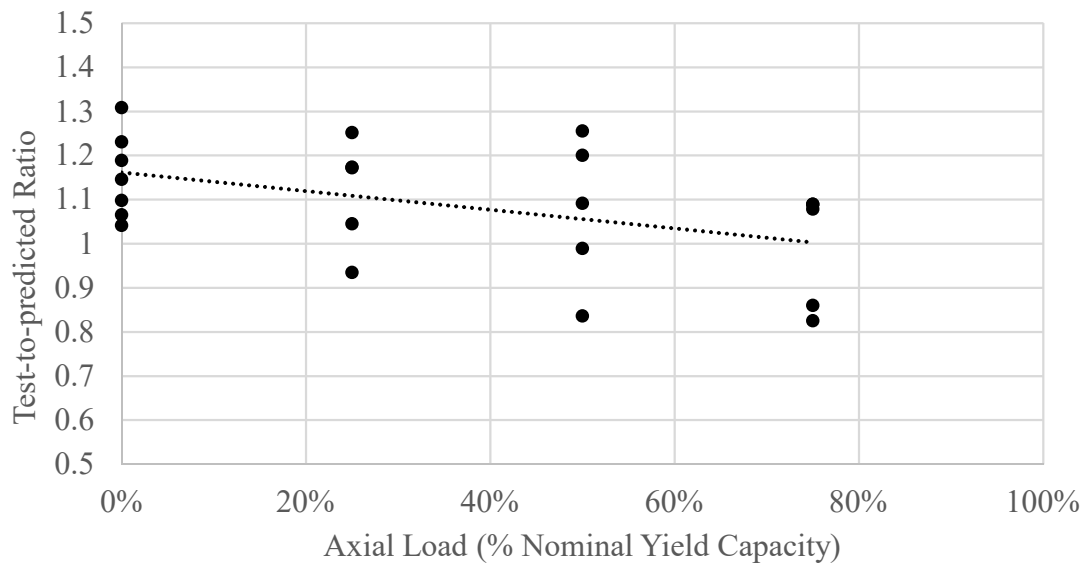
Figure 5.4: Effect of Axial Load on Test-to-Predicted Ratio (Torsionally Pinned)

All tests that fall below a test-to-predicted ratio of 1.0 correspond to an over-prediction of elastic stiffness, which is un-conservative in most design scenarios. The trendline shown by the dotted line indicates a steady reduction in test-to-predicted ratio as the axial load increases; however,

almost all data points are greater than 1.0 until the axial load is quite large. Considering the axial load needs to be even higher than what was tested in this program before the trendline extends below 1.0, it is suggested that Equation 5-5 is appropriate for all but the highest levels of cross-sectional utilization under axial load. This would capture most typical design scenarios as the designer is unlikely to fully utilize the columns axial capacity if significant torsional moments are expected. For members where the applied axial load is greater than 50% of its nominal yielding capacity (which corresponds to approximately 70% of the members S16 design capacity), it is suggested the empirical factor, $1.5r_1$, that describes the effective width be replaced by $1.2r_1$ to account for the reduction in initial stiffness that may occur due to residual stresses in the column. Table 5-5 shows the impact of this modification on the mean test-to-predicted ratio for all 15 tests when the effective width is reduced for the five members subjected to 75% axial load. The predicted values were calculated assuming torsionally pinned boundary conditions.

Table 5-5: Effect of Axial Load Modifier on Elastic Stiffness Prediction (75% Axial Load)

	K_u Without Load Modifier	K_u With Load Modifier
Mean Test-to-Predicted Ratio	1.09	1.11
Coefficient of Variation	0.12	0.11

By including the axial load modification factor into Equation 5-5 for the cases with 75% axial load, the elastic stiffness prediction is more conservative with a slight reduction to the coefficient of variation over the 22 full-scale test results. The $1.2r_1$ was obtained by multiplying the original factor of 1.5 by the lower bound of 0.8 that was selected based on Figure 5.4 to conservatively account for the four test results that fall below a test-to-predicted ratio of 1.0. The moment–rotation response of all full-scale tests in the current study are compared to the elastic stiffness prediction using Equation 5-4. The elastic stiffness of the column has been calculated assuming both torsionally fixed and torsionally pinned boundary conditions in Figure 5.5 to Figure 5.19. For nearly all tests, the predicted behaviour shows better correlation with the full-scale tests when assuming a torsionally pinned boundary condition.
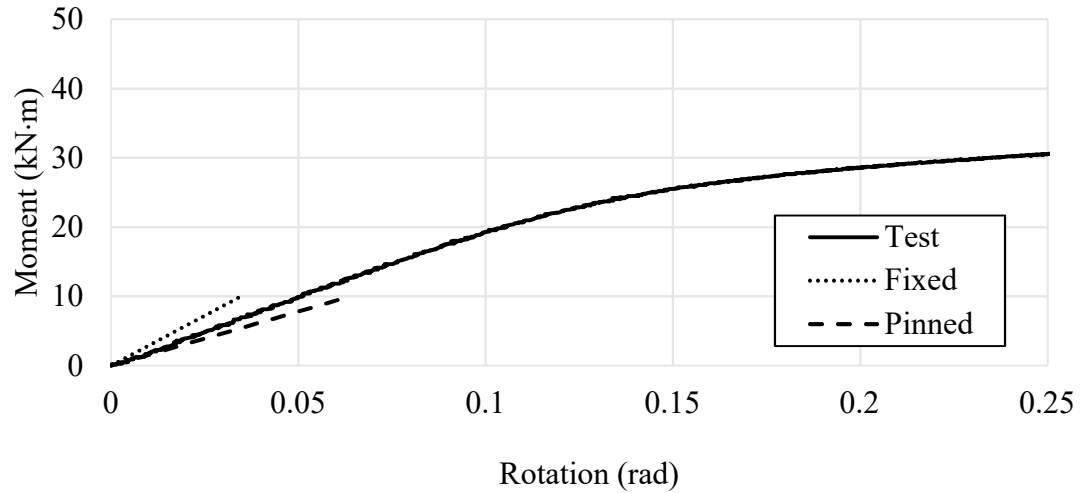
Figure 5.5: Evaluation of Torsional Boundary Conditions for W250×89 (25% Axial Load)
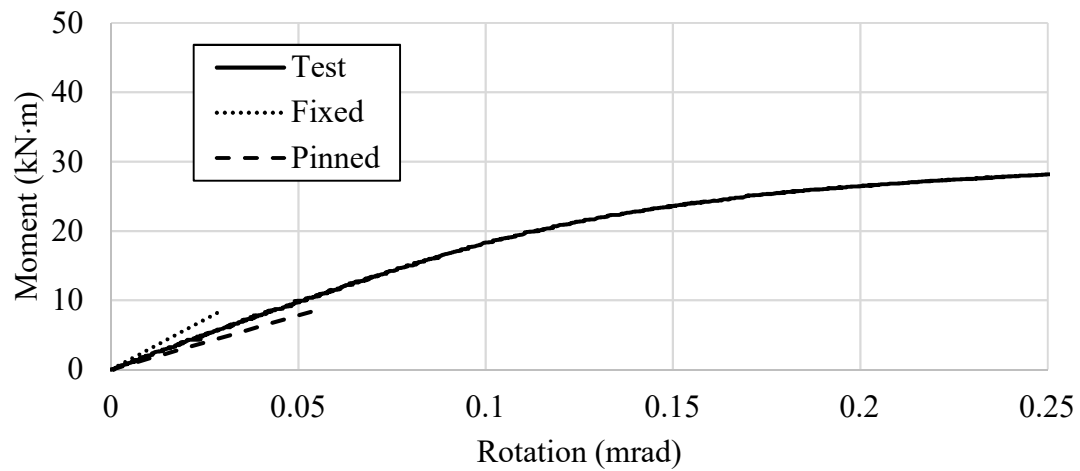
Figure 5.6: Evaluation of Torsional Boundary Conditions for W250×89 (50% Axial Load)
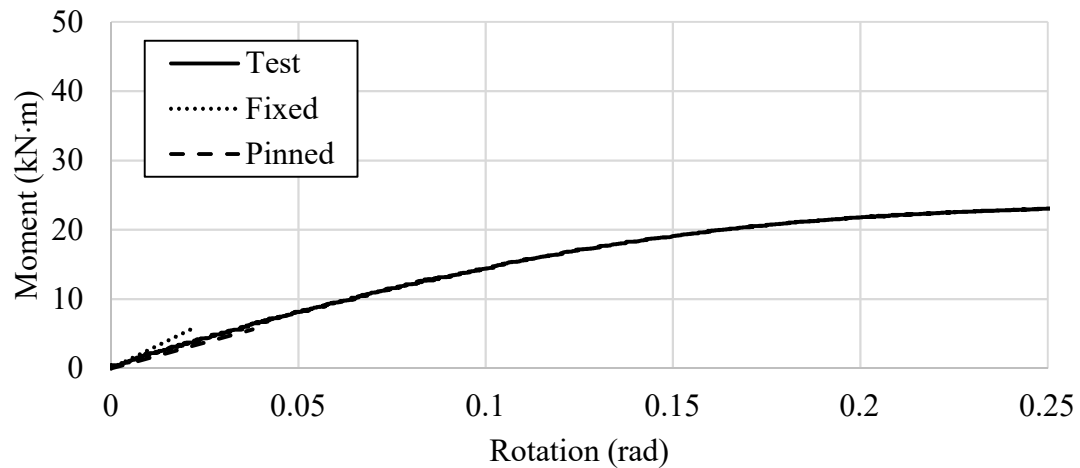
Figure 5.7: Evaluation of Torsional Boundary Conditions for W250×89 (75% Axial Load)
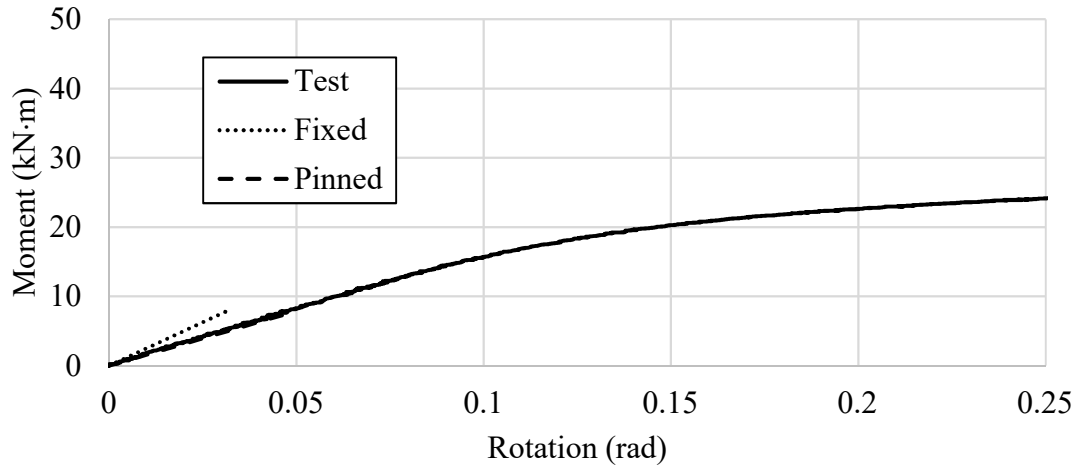
Figure 5.8: Evaluation of Torsional Boundary Conditions for W360×91 (25% Axial Load)
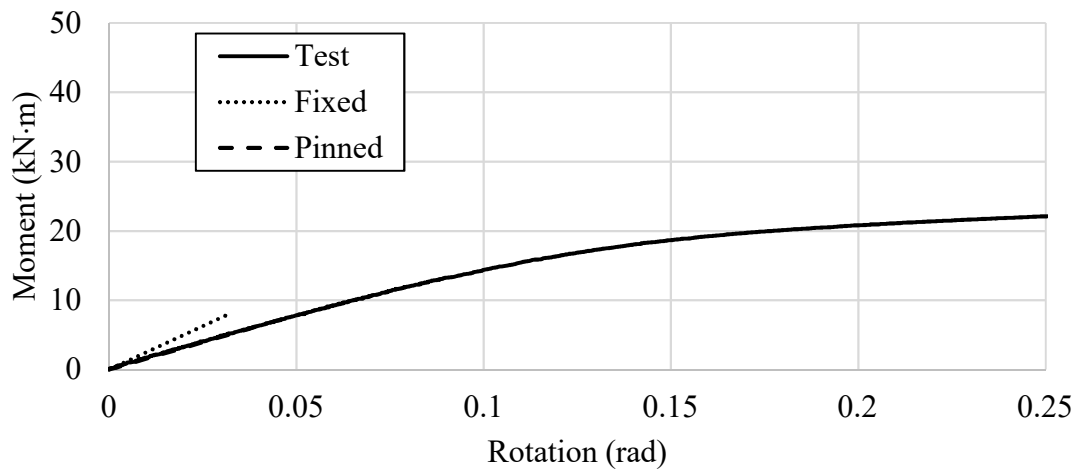
Figure 5.9: Evaluation of Torsional Boundary Conditions for W360×91 (50% Axial Load)
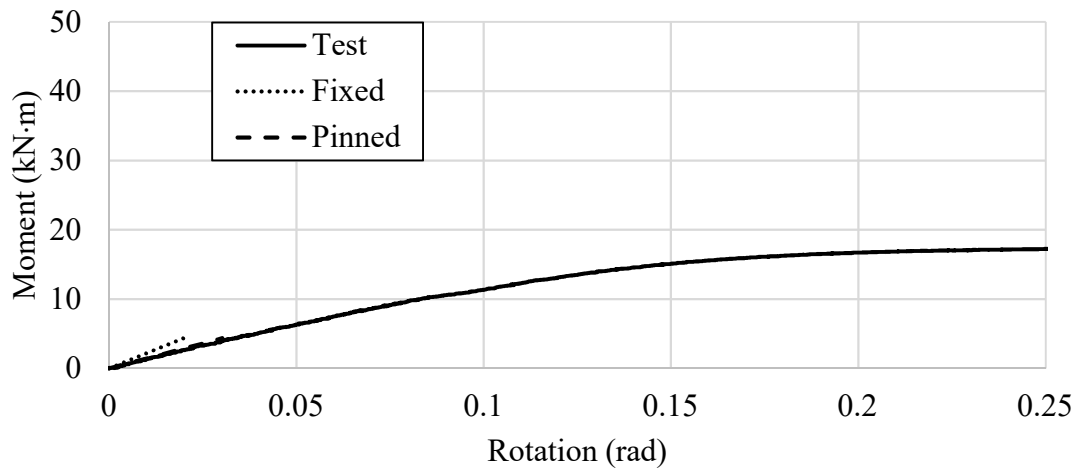
Figure 5.10: Evaluation of Torsional Boundary Conditions for W360×91 (75% Axial Load)
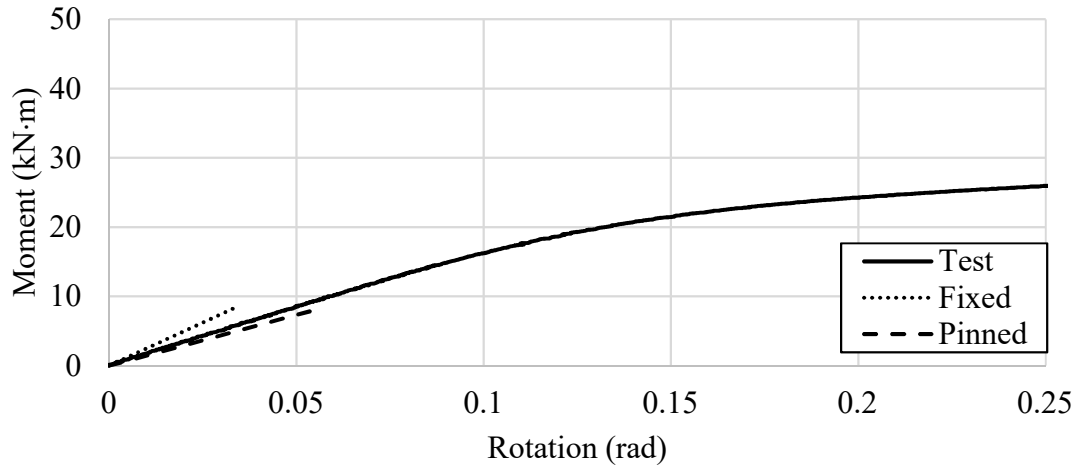
Figure 5.11: Evaluation of Torsional Boundary Conditions for W310×86 (25% Axial Load)
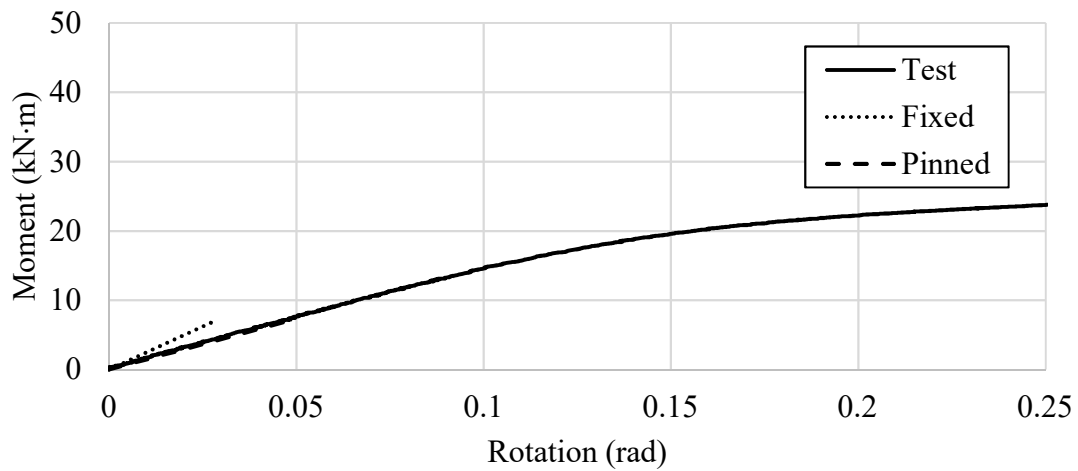
Figure 5.12: Evaluation of Torsional Boundary Conditions for W310×86 (50% Axial Load)
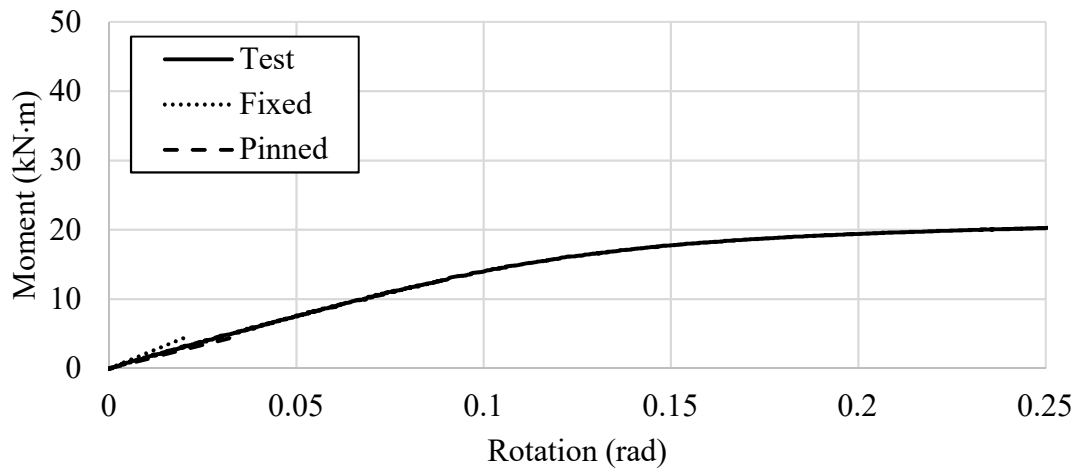
Figure 5.13: Evaluation of Torsional Boundary Conditions for W310×86 (75% Axial Load)
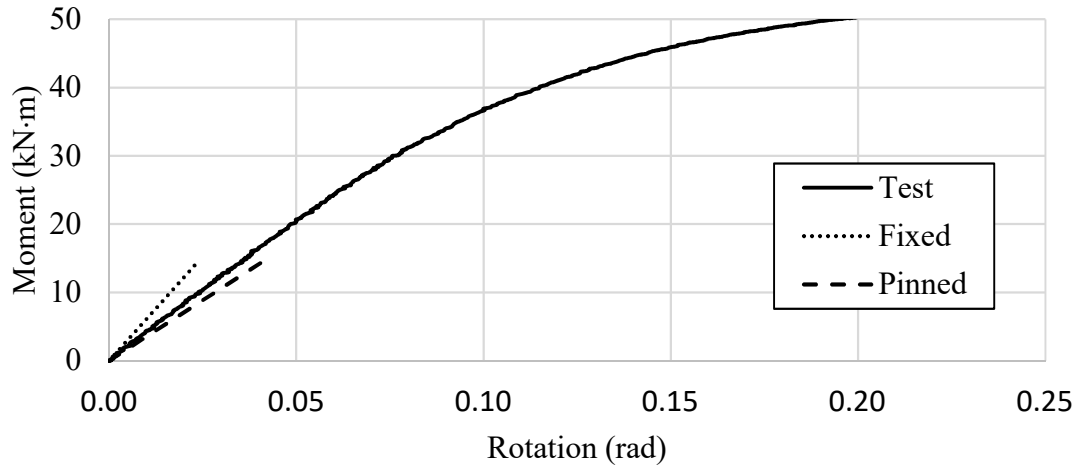
Figure 5.14: Evaluation of Torsional Boundary Conditions for W310×129 (25% Axial Load)
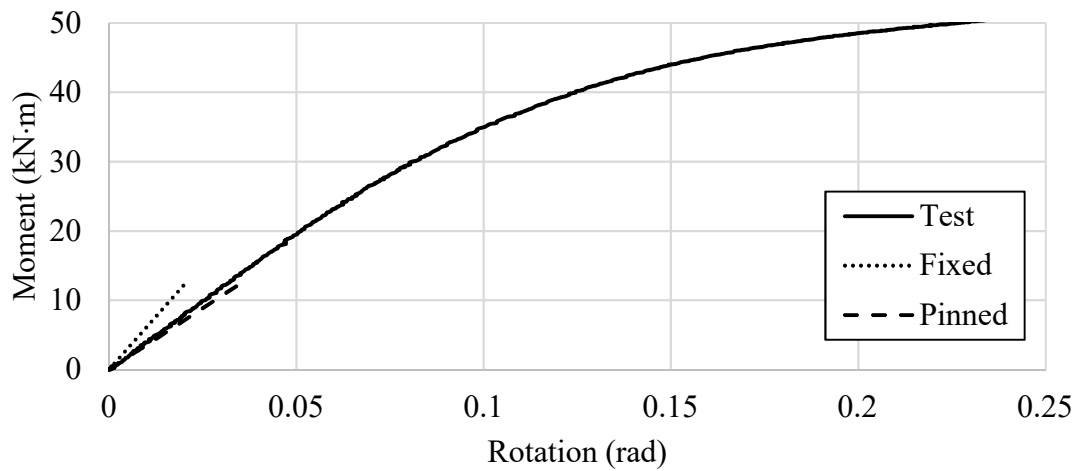
Figure 5.15: Evaluation of Torsional Boundary Conditions for W310×129 (50% Axial Load)
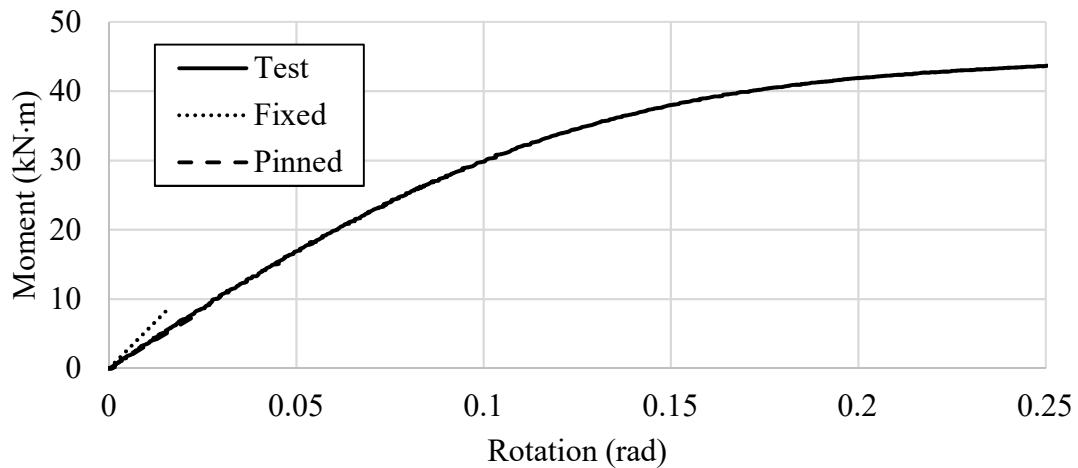
Figure 5.16: Evaluation of Torsional Boundary Conditions for W310×129 (75% Axial Load)
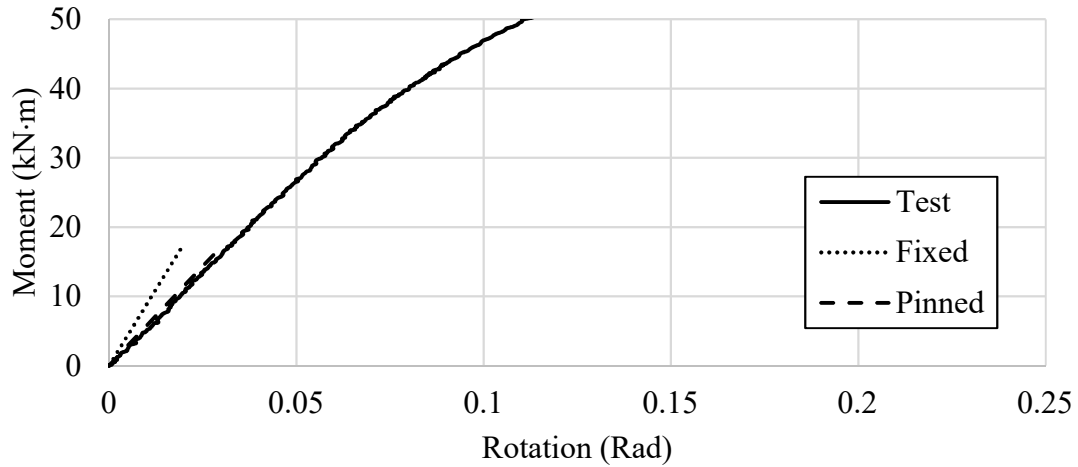
Figure 5.17: Evaluation of Torsional Boundary Conditions for W360×162 (25% Axial Load)
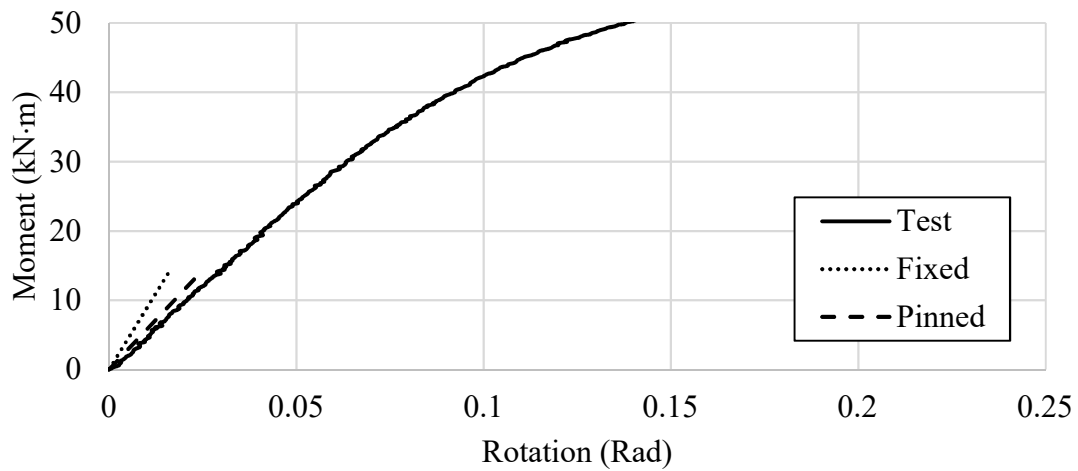
Figure 5.18: Evaluation of Torsional Boundary Conditions for W360×162 (50% Axial Load)
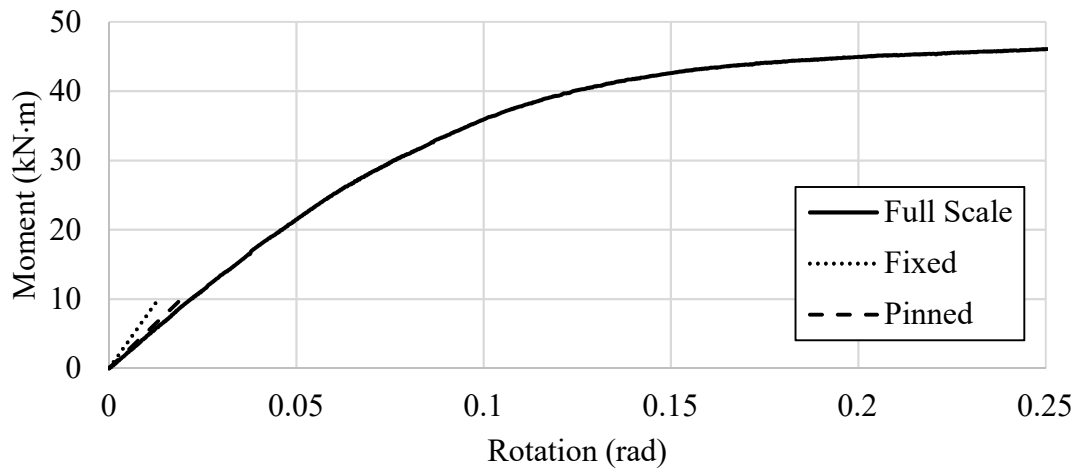
Figure 5.19: Evaluation of Torsional Boundary Conditions for W360×162 (75% Axial Load)

5.3 Comparison with Analytical Model of Gil et al. (2015)

Gil et al. (2015) created a design procedure using the component method to predict the strength and stiffness of wide-flange members subjected to torsion applied to one flange. A comparison between resisting components defined by Gil et al. (2015) and the current study, such as the column flange in torsion or the column web in bending, is inappropriate due to differences between the two studies in how these components are characterized. The current study characterizes the column behaviour by combining the torsional strength and stiffness of the flange into a single model that predicts column behaviour based on the bending strength of the web only. Gil et al. (2015) define these components independently and combine them with other resisting components present in the connection to obtain an overall joint behaviour. However, a comparison of the overall strength and elastic stiffness of the connection can be made for tests where yielding initiated at the toe of the fillet. Table 5-6 compares the strength and stiffness predictions for all unstiffened tests conducted by Gil and Goñi (2015). T-Stub03 was not included because the column web remained elastic throughout the test. The majority of yielding and rotation that occurred in this test was caused by distortion of the end plate and yielding of the loading beam, which is not being studied in the current research. The plastic moment capacity reported from the current study was obtained by applying a 1.5 shape factor to the yield moment prediction obtained using Equation 5-3.

Table 5-6: Strength and Stiffness Comparisons with Gil et al. (2015)

Test	Strength Prediction, M_p (kN·m)			Stiffness Prediction (kN·m/rad)			
	Test Result	Gil and Goñi (2015)	Current Study	Test Result	Gil and Goñi (2015)	Current Study (Fixed)	Current Study (Pinned)
T-Stub01	8.4	8.6	5.9	120	118	173	130
T-Stub04	8.0	-	5.9	115	-	173	130

The current study is conservative when predicting the strength of the connection for cases where the column web is the weakest component: T-Stub01 and T-Stub04. It should be noted that yield moments reported as "Test Result" in Table 5-6 were obtained from numerical simulations because strain gauges were not present at the toe of the fillet in the full-scale tests.

In all cases, the current study largely over-predicts the initial connection stiffness when assuming torsionally fixed boundary conditions. However, when assuming a torsionally pinned boundary

condition, the elastic stiffness prediction from the current study fits the test results quite well, which is likely closer to the true boundary condition that was achieved in the full-scale tests, as discussed in Section 5.2. The method used by Gil et al. (2015) assumes a torsionally fixed boundary condition and their results fit quite well; however, their design formulations are calibrated from a numerical model whose mesh may need further optimization to capture the behaviour of the wide-flange member accurately. The numerical model used in the parametric study by Gil et al. (2015) utilized solid elements with reduced integration. Elements through the web were around 4 mm in thickness, whereas the current study found that elements needed to be approximately 1–2 mm thick with full integration to avoid an over-prediction of strength and stiffness compared to full-scale test results.

The design methodology in the current study is conservative when predicting the strength of the joint and accurate when predicting the elastic stiffness assuming torsionally pinned boundary conditions for tests where the column is the governing component. The proposed design procedure has the advantage of being simple to apply, whereas the procedure outlined by Gil et al. (2015) requires considerable effort to characterize the strength and stiffness of each component.

6 Summary and Recommendations

6.1 Summary

The complex nature of industrial structural loading scenarios has led to load combinations that are not adequately addressed in current standards and design provisions. One example includes axially-loaded wide-flange members subjected to torsion through one flange. The application of torsional moment has typically led designers to default to a conservative solution by adding full-depth column web stiffeners to prevent any localized distortion of the cross-section, which adds both time and cost to the overall fabrication of the structure. Previous research has provided a method for predicting the strength and stiffness of the unstiffened column without considering the effect of axial load on the connection behaviour, which may be significant in a real structure. The current study has conducted both numerical simulations and full-scale tests to investigate this behaviour in the presence of axial load.

Ahmad et al. (2018) suggested that the rotation of an unstiffened wide-flange member subjected to torsion applied through one flange is a combination of uniform cross-sectional rotation and localized rotations due to flexing of the web. Milner and Rao (1978) and Yura (2001) proposed a method for predicting the localized web stiffness. A solution for the moment capacity of the member was initially proposed by Dowswell (2010), who used an effective width concept to predict the strength of the wide-flange member based on the bending strength of the web only. Ahmad et al. (2018) refined the effective width to be a function of the connection size and ratio of the major resisting components that are engaged to resist the applied torque. The addition of axial load was explored briefly by Ahmad et al. (2016), where the strength of the connection was determined through a von Misses stress interaction to account for the axial stress.

Numerical simulations were performed to identify key relationships such as Poisson ratio interactions that were not considered in previous research. Ten wide-flange shapes were tested under varying levels of axial load to better understand the overall behaviour. By investigating parameters including the effective width, bending stress at the web surface, and longitudinal stress at first yield, the current study identified that a considerable longitudinal stress develops at the surface of the web that was not considered previously. The effective width did not change significantly under varying levels of axial load, while a consistent reduction in yield moment was

observed as the compressive stress increased. Following the full-scale testing program, additional numerical simulations were conducted using measured material properties and variable torsional boundary conditions to compare with the results obtained from laboratory tests.

The full-scale testing program consisted of five standard sections from the *Handbook of Steel Construction* (CISC 2016), tested at 25, 50, and 75% of their nominal axial yielding capacity to make a total of 15 tests. The initial yield moment showed good agreement with predicted values that included the effect of Poisson's ratio interactions. Although the method of applying axial force necessarily imposed some warping restraint at the ends, the initial stiffness in nearly all test showed behaviour that was between torsionally fixed and torsionally pinned; this is because it is difficult to provide enough warping restraint to obtain torsionally fixed behaviour in real structures. Additionally, yielding of the flange tips when the compressive stress is large may cause softening in the torsional response of the member. Two cross-sections common to the current study and that of Ahmad et al. (2018) showed the addition of axial load increases the initial stiffness of the column up to the point where yielding of the flanges causes load shedding, which can lead to an initial stiffness even less than a member without axial load.

The design procedure suggested by Ahmad et al. (2018) was modified in the current study to better match the results obtained in the full-scale testing program. The elastic moment capacity equation was adapted to include the impact of Poisson's ratio interactions and an empirically derived reduction factor based on section depth. The modification based on section depth was embedded in the effective width, which is dependent on the major resisting components that resist the torsional moment. The revised elastic moment capacity equation showed close agreement with test values, resulting in a mean test-to-predicted ratio of 1.0, with a coefficient of variation equal to 0.09. The initial stiffness was studied using results from the current study and those of Ahmad et al (2018). Given the initial stiffness in nearly all tests resulted in a mean-test-to-predicted stiffness ratio equal to 1.11 when assuming torsionally pinned end restraints, for simplicity it is suggested that torsionally pinned boundary conditions be assumed for all design scenarios. This is reasonable given the challenges associated with ensuring reliable warping restraint in real structures. Findings from the current study agree with a recommendation by Ahmad et al. (2018), who suggest an upper limit to the maximum flange torsional stiffness component value (bt^3) that is permitted when evaluating the stiffness ratio, r_1. Additionally, the current research suggests a reduction in effective

width for a member loaded axially to a force greater than 50% of its nominal axial yielding capacity.

By providing designers with simple formulations that accurately predict the strength and stiffness of axial-loaded wide-flange members subjected to torsion through one flange, the use of unnecessary stiffeners in these type of loading scenarios can be eliminated. This will lead to more efficient structures that stand to provide considerable fabrication and construction cost savings.

6.2 Recommendations for Future Research

The current research has identified that residual stresses likely play a significant role in the stiffness response of members under high levels of axial load. Quantification of these stresses is difficult and they can vary significantly. Future research may strive to quantify these effects and incorporate them explicitly into the proposed design formulations.

Global buckling of the column is another aspect that has not been considered in the current research. Although column buckling was not observed during the full-scale testing program, there is surely a limit on the amount of cross-sectional distortion that can occur before the axial load carrying capacity of the member is compromised. Although this limit may not be of practical significance for most design scenarios, a method of predicting the buckling capacity of axially loaded members subjected to torsional moments would be beneficial to designers.

References

Ahmad, M., Driver, R. G., Callele, L., and Dowswell, B. (2016). "Behaviour and Design of Unstiffened Wide-Flange Members Subjected to Torsional Moment Through One Flange." *Rep. No. 307*, University of Alberta, Edmonton, AB.

Ahmad, M., Driver, R. G., Callele, L., and Dowswell, B. (2018). "Design of steel wide-flange members for torsion applied through one flange." *J. Const. Steel Res.*, 141, 50–62.

AISC. (2005). *Steel Construction Manual, 13th Edition*. Chicago, IL.

ASTM. (2014). *A370-14: Standard Test Methods and Definitions for Mechanical Testing of Steel Products*. ASTM International, West Conshohocken, PA.

ASTM. (2011). *A6/A6M–11: Standard Specification for General Requirements for Rolled Structural Steel Bars, Plates, Shapes, and Sheet Piling.* ASTM International, West Conshohocken, PA.

CISC. (2016). *Handbook of Steel Construction, 11th Edition*. Markham, ON.

CSA. (2014). *S16-14 Design of Steel Structures*. Canadian Standards Association, Mississauga, ON.

Dowswell, B. (2010). "Flexure of Webs Due to Out-of-Plane Moments Applied at the Flange." *Connection Design for Steel Structures*, Chapter 17 (1-3).

Gil, B., Bijlaard, F., and Bayo, E. (2015). "T-stub behavior under out-of-plane bending. II: Parametric study and analytical characterization." *Engineering Structures*, 98, 241–250.

Gil, B., and Goñi, R. (2015). "T-stub behaviour under out-of-plane bending. I: Experimental research and finite element modelling." *Engineering Structures*, 98, 230–240.

Kaufmann, E. J., Metrovich, B., Pense, A. W., and Fisher, J. W. (2001). "Effect of Manufacturing Process on K-Area Properties and Service Performance." *North American Steel Construction Conference*, Ft. Lauderdale, 17-1–17-24.

Milner, H.R., Rao, S. N. (1978). "Strength and Stiffness of Moment Resisting Beam-Purlin Connections." *Inst Eng Aust Civ Eng Trans*, CE 20(1), 37–42.

Milner, H. R. (1977a). "The Design of Simple Supported Beams Braced Against Twisting on the Tension Flange." *Inst Eng Aust Civ Eng Trans*, CE 19(1), 84–91.

Milner, H. R. (1977b). "Tests on Equal Flanged Beams Braced Against Twisting on the Tension Flange." *Inst Eng Aust Civ Eng Trans*, CE 19(1), 92–100.

Milner, H. R., and Rao, S. N. (1977). "The Twisting of Universal Beam Members by a Torsional Moment Applied to One Flange." *Sixth Australasian Conference on the Mechanics of Structures and Materials*, Christchurch, 293–298.

Yura, J. A. (2001). "Fundamentals of Beam Bracing." *AISC Eng. J.*, 38(1), 11–26.

Appendix A Fabrication Drawings

Test Specimens, Testing Apparatus, and Tension Coupon Locations
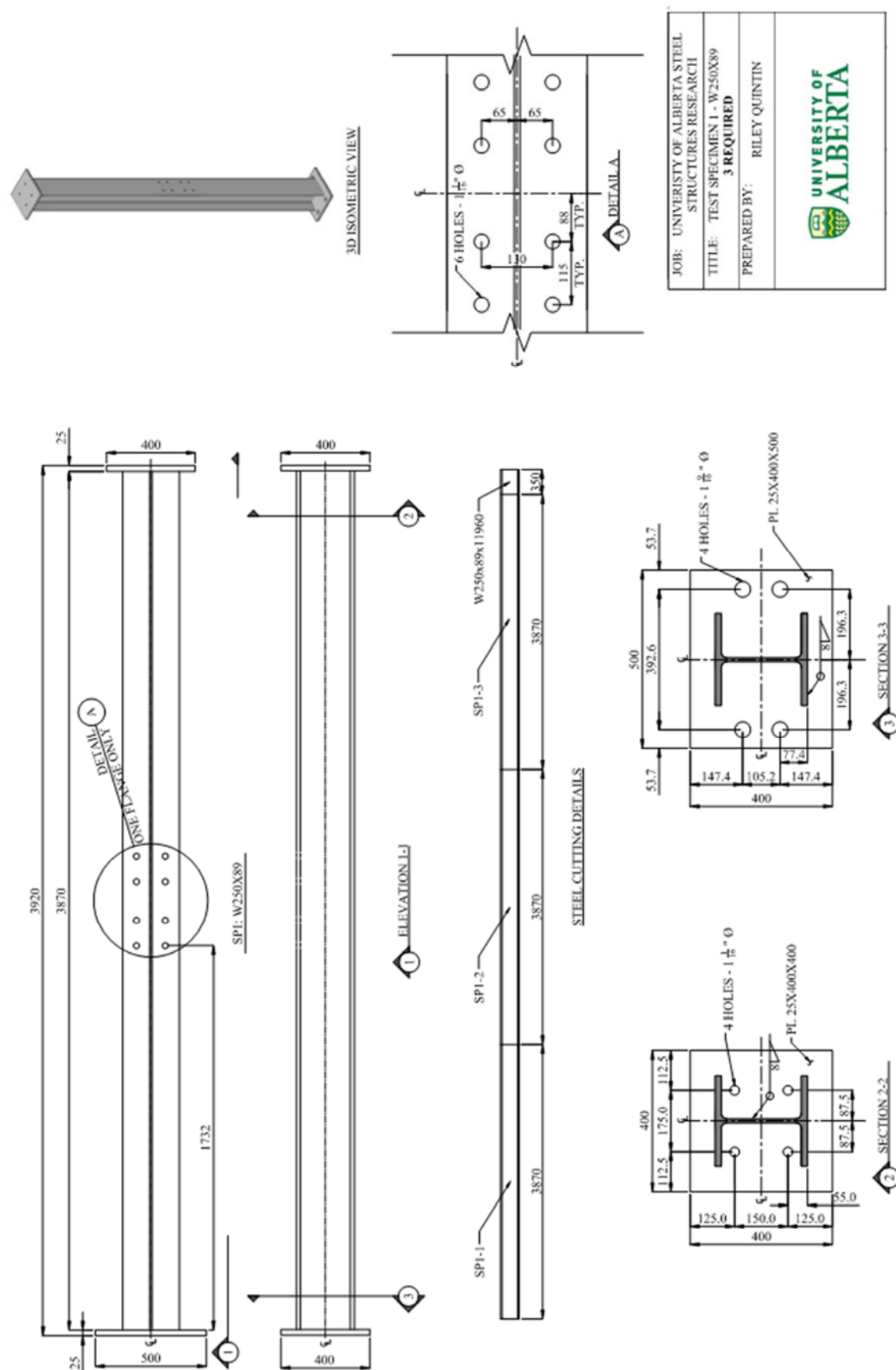
Figure A.1: Drawing SP1
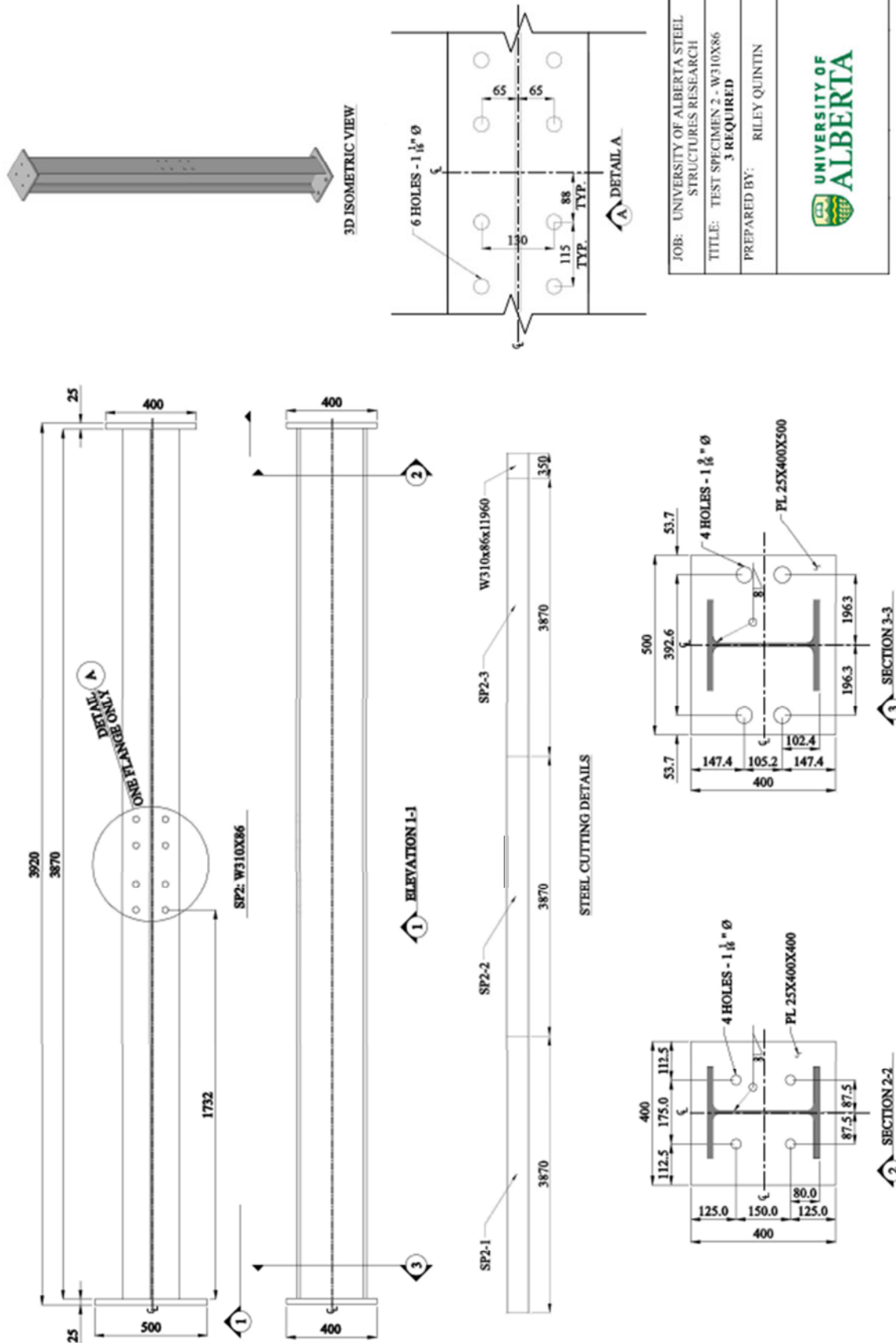
Figure A.2: Drawing SP2
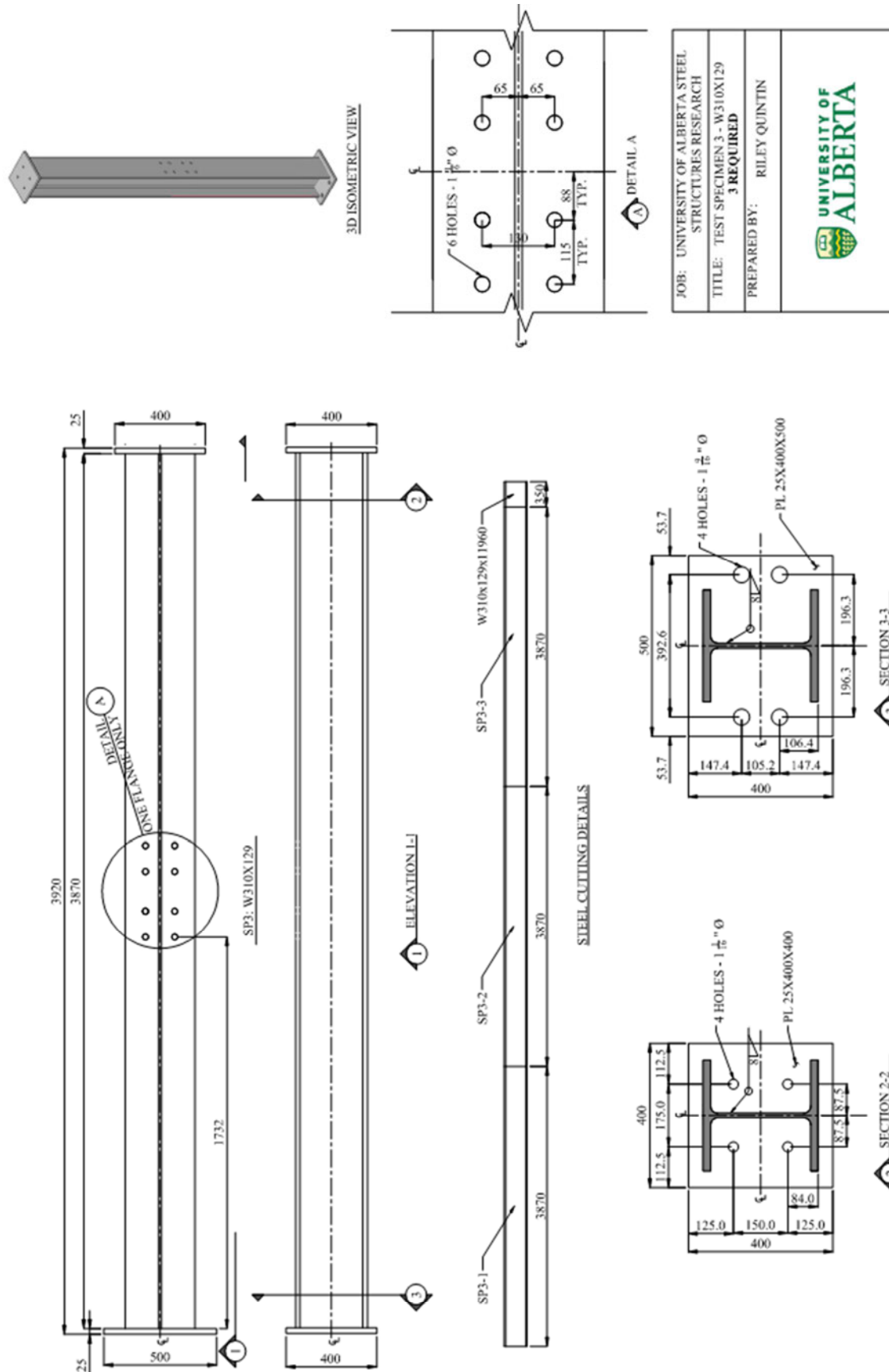
Figure A.3: Drawing SP3
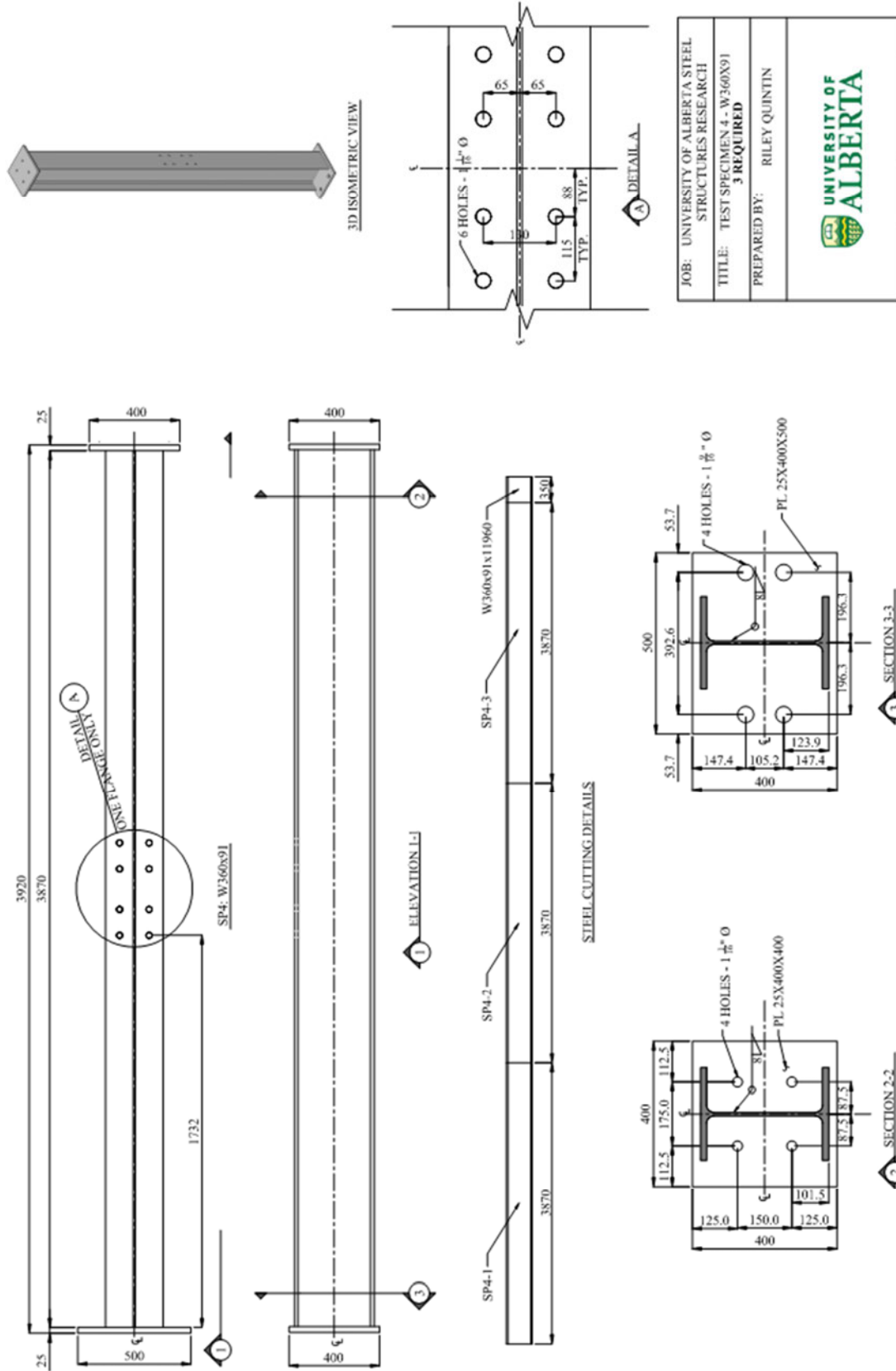
Figure A.4: Drawing SP4
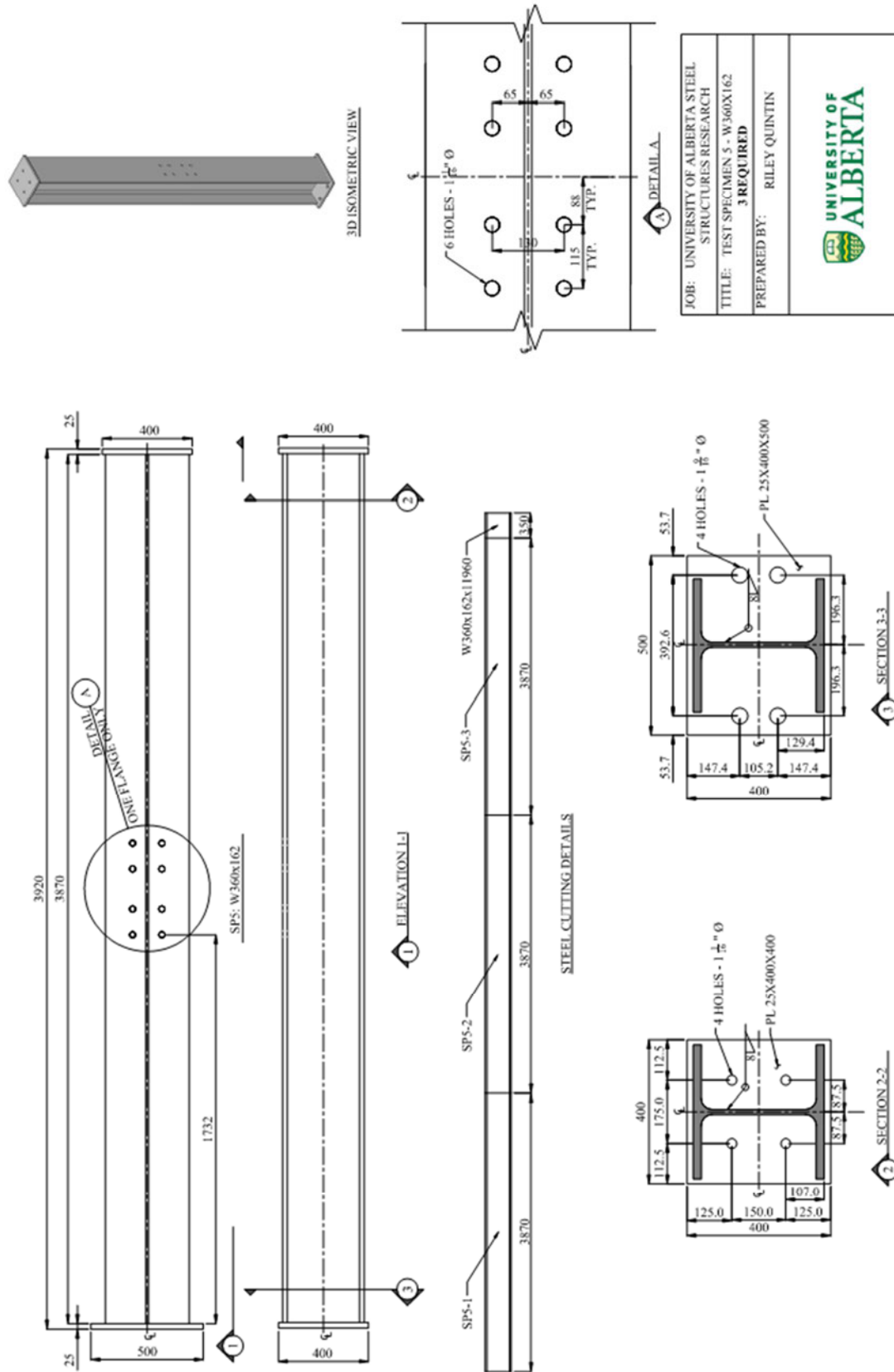
Figure A.5: Drawing SP5
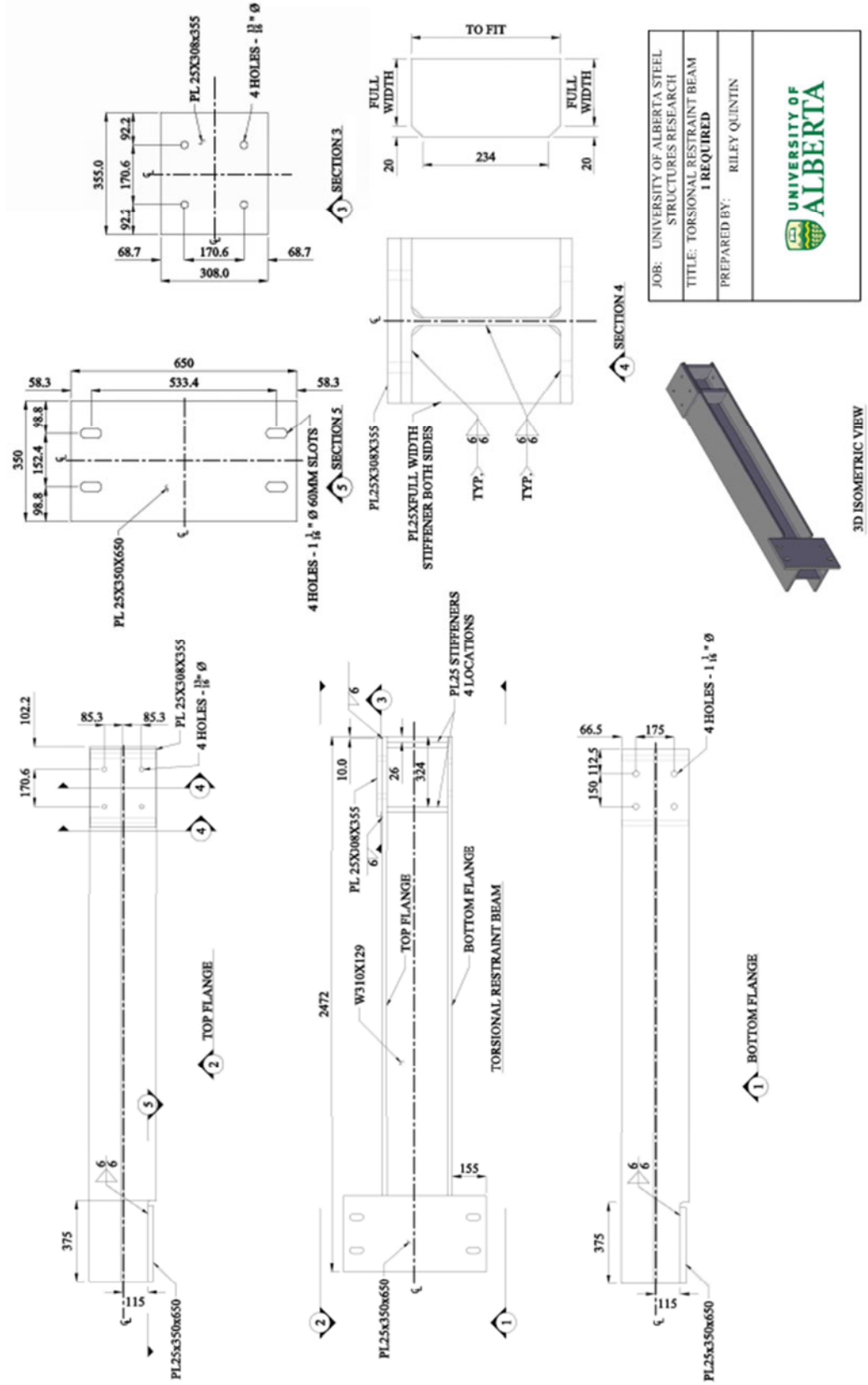
Figure A.6: Drawing Torsional Restraint Beam

Figure A.7: Drawing Actuator Connections

Figure A.8: Tension Coupon Cutting Locations

GENERAL NOTES:

1. UNLESS NOTED OTHERWISE, ALL DIMENSIONS ARE IN MM
2. DRAWINGS ARE TO BE PLOTTED ON 11X17 PAPER
3. ALL DIMENSIONS PROVIDED ARE AS PER ASTM A370-13A, SHEET-TYPE
4. THE REDUCED SECTIONS OF THE SPECIMEN SHOULD BE FREE OF COLD WORK, NOTCHES CHATTER MARKS, GROOVES, GOUGES BURRS, ROUGH SURFACES OR EDGES, OVERHEATING OR ANY OTHER CONDITION WHICH DELETERIOUSLY AFFECT THE PROPERTIES TO BE MEASURED.
5. WITHIN THE REDUCED SECTION OF RECTANGULAR SPECIMENS, EDGES OR CORNERS SHOULD NOT BE GROUND OR ABRADED.
6. THE RADII OF ALL FILLETS SHALL BE EQUAL TO EACH OTHER, AND THE CENTER OF CURVATURE OF THE TWO FILLETS AT A PARTICULAR END SHALL BE LOCATED ACROSS FROM EACH OTHER (ON A LINE PERPENDICULAR TO THE CENTERLINE).
7. THE ENDS OF THE SPECIMEN SHALL BE SYMMETRIC WITH THE CENTER LINE OF THE REDUCED SECTION.
8. ALL SPECIMENS SHALL BE WATER CUT JET OR MILLED (NO HEAT)
9. THICKNESS OF COUPON TO BE FULL THICKNESS OF MATERIAL PROVIDED.
10. COUPONS SHALL BE LABELED SUCH THAT THEY CAN BE MATCHED TO THE LOCATION FROM WHICH THEY WERE ORIGINALLY CUT.
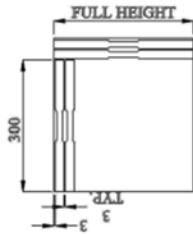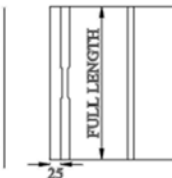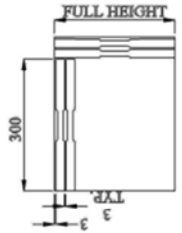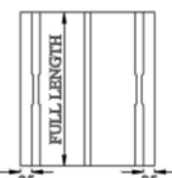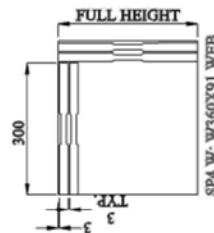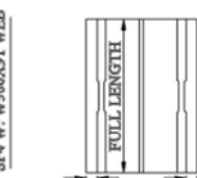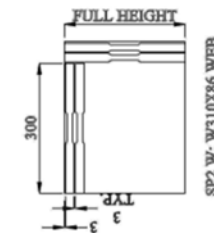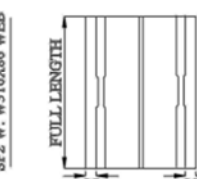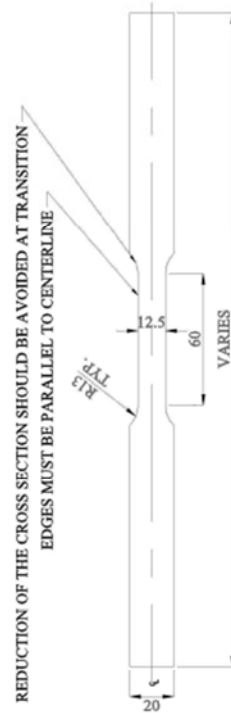
REDUCTION OF THE CROSS SECTION SHOULD BE AVOIDED AT TRANSITION
EDGES MUST BE PARALLEL TO CENTERLINE

R13 TYP.

12.5

60

VARIES

20

TENSION COUPON DETAILS (RELEVANT FOR ALL COUPONS)

JOB: UNIVERSITY OF ALBERTA STEEL STRUCTURES RESEARCH

TITLE: TENSION COUPON DETAILS

PREPARED BY: RILEY QUINTIN

UNIVERSITY OF ALBERTA

FULL HEIGHT
300
3 TYP
SP5 W: W360X162 WEB

FULL LENGTH
25   25
SP5 F: W360X162 FLANGE

FULL HEIGHT
300
3 TYP
SP3 W: W310X129 WEB

FULL LENGTH
25   25
SP3 F: W310X129 FLANGE

FULL HEIGHT
300
3 TYP
SP4 W: W360X91 WEB

FULL LENGTH
25   25
SP4 F: W360X91 FLANGE

FULL HEIGHT
300
3 TYP
SP1 W: W250X89 WEB

FULL LENGTH
25   25
SP1 F: W250X89 FLANGE

FULL HEIGHT
300
3 TYP
SP2 W: W310X86 WEB

FULL LENGTH
25   25
SP2 F: W310X86 FLANGE

Appendix B Full-Scale Test Results

Von Mises Stress from Strain Gauges and Ancillary Test Results

Figure B.1: Stress–Strain Curves for Coupons SP1

Figure B.2: Stress–Strain Curves for Coupons SP2
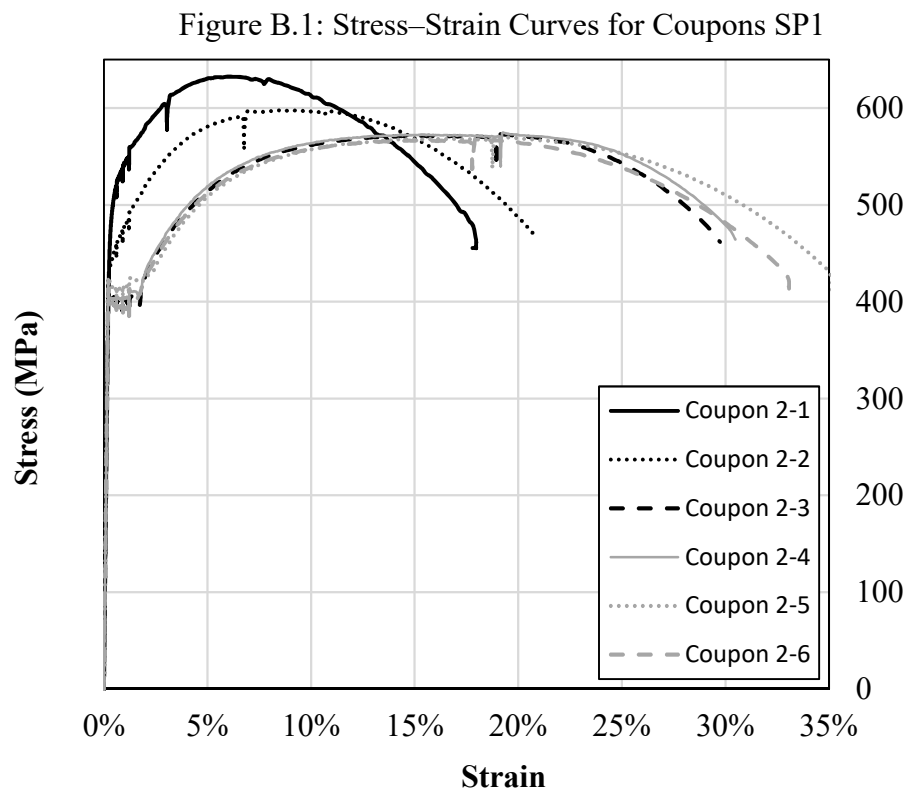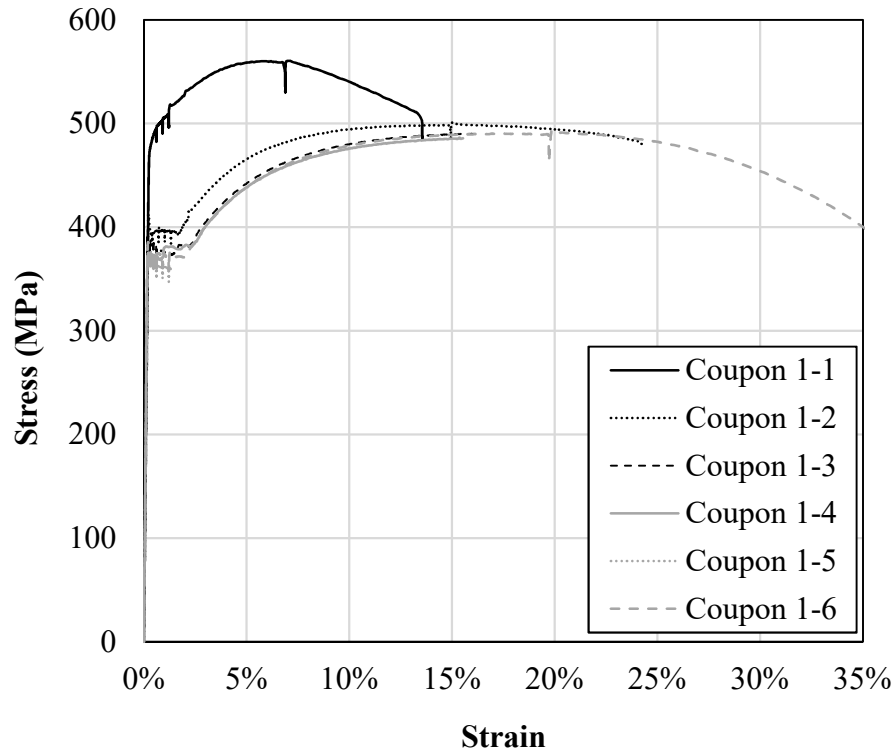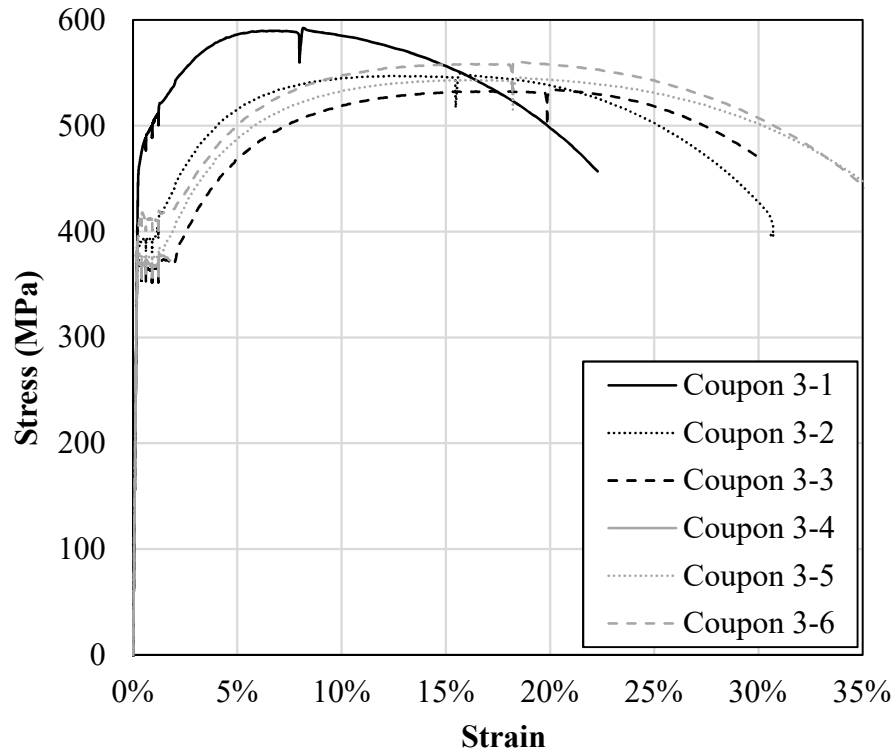
Figure B.3: Stress–Strain Curve for Coupons SP3
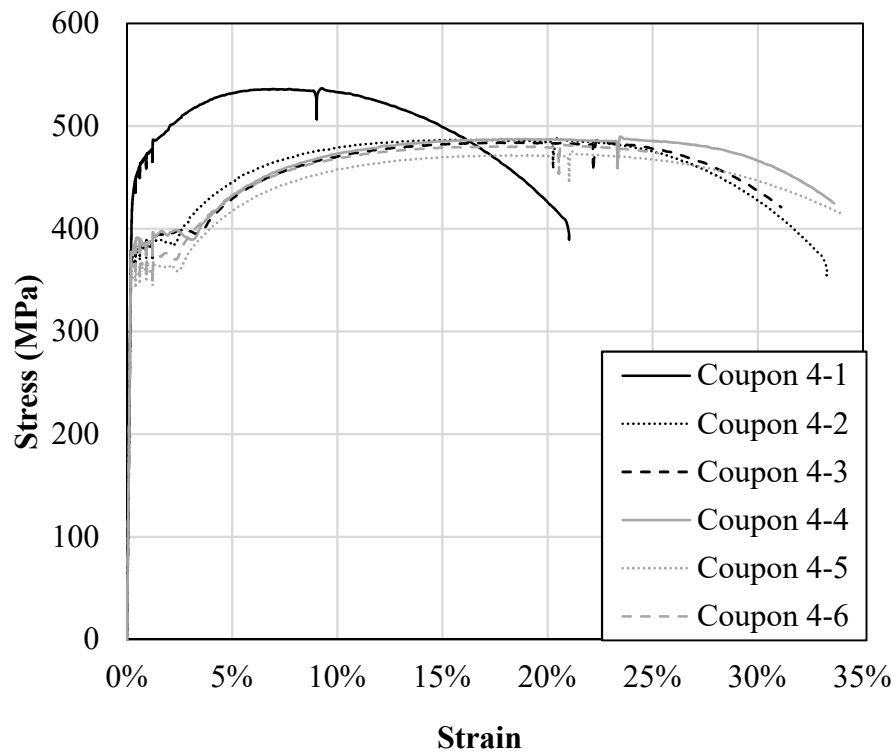
Figure B.4: Stress–Strain Curve for Coupons SP4
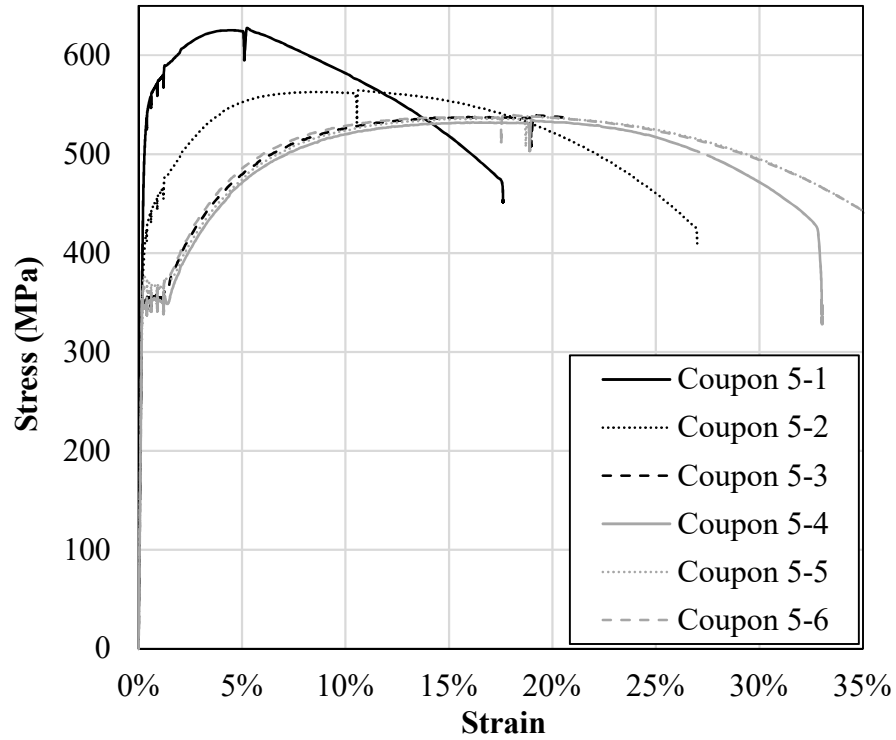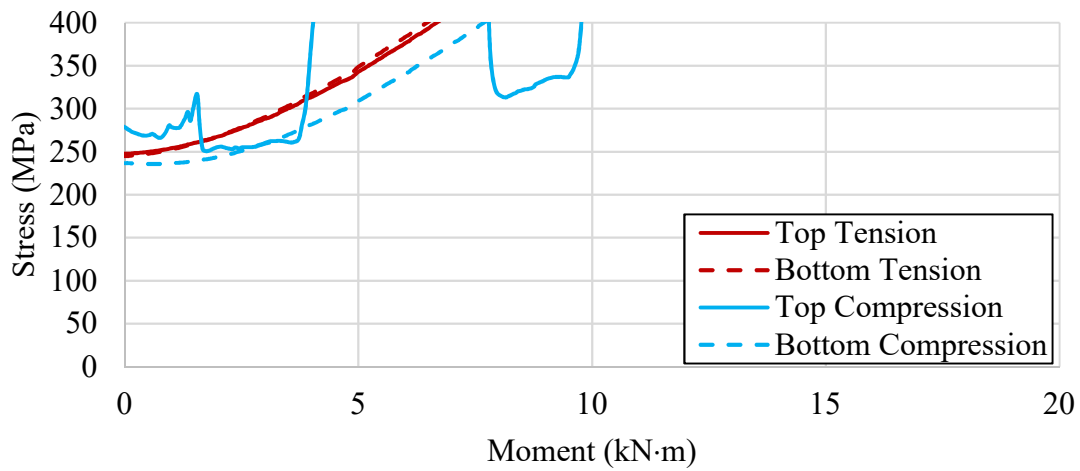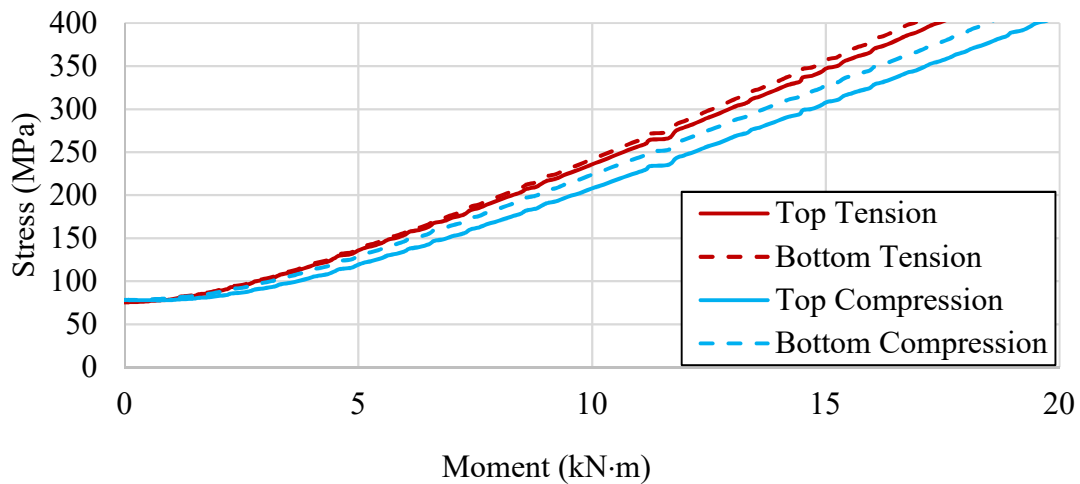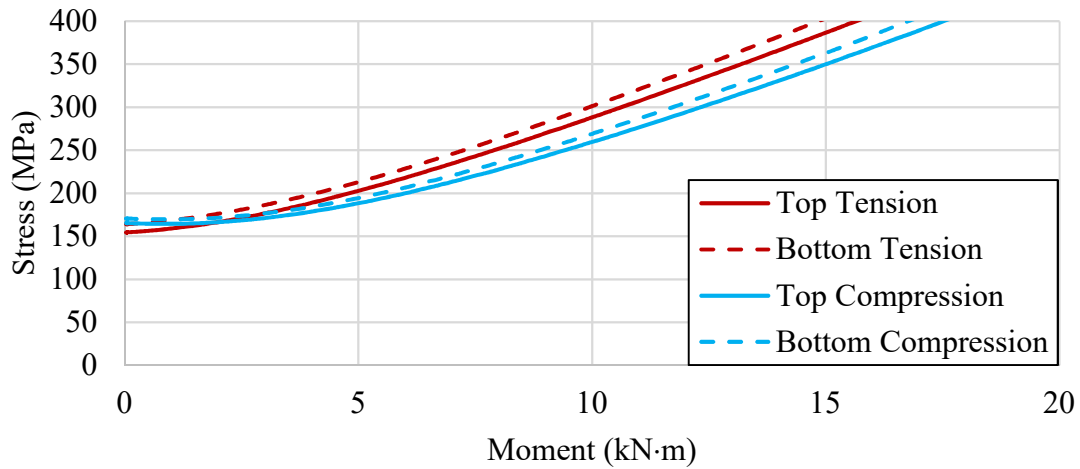
Figure B.5: Stress–Strain Curve for Coupons SP5
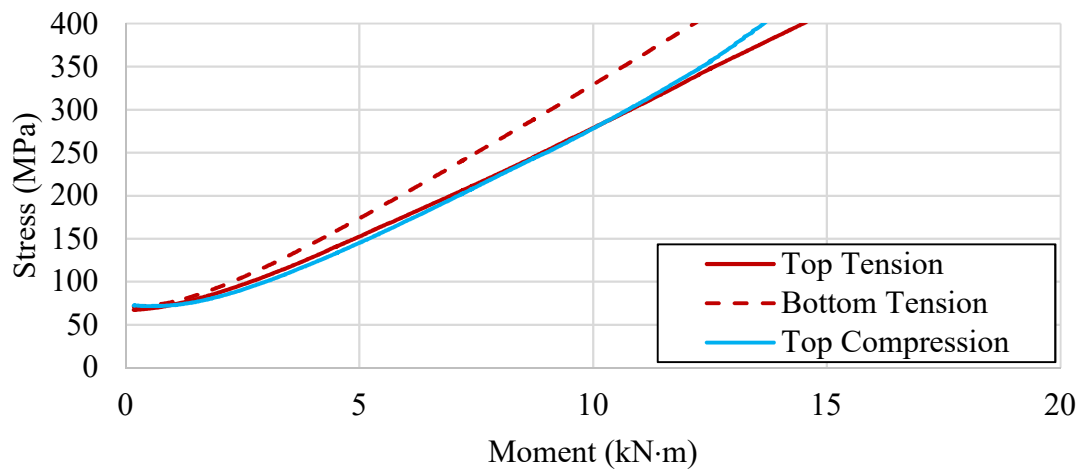
Figure B.6: von Mises Stress for Test SP1-1
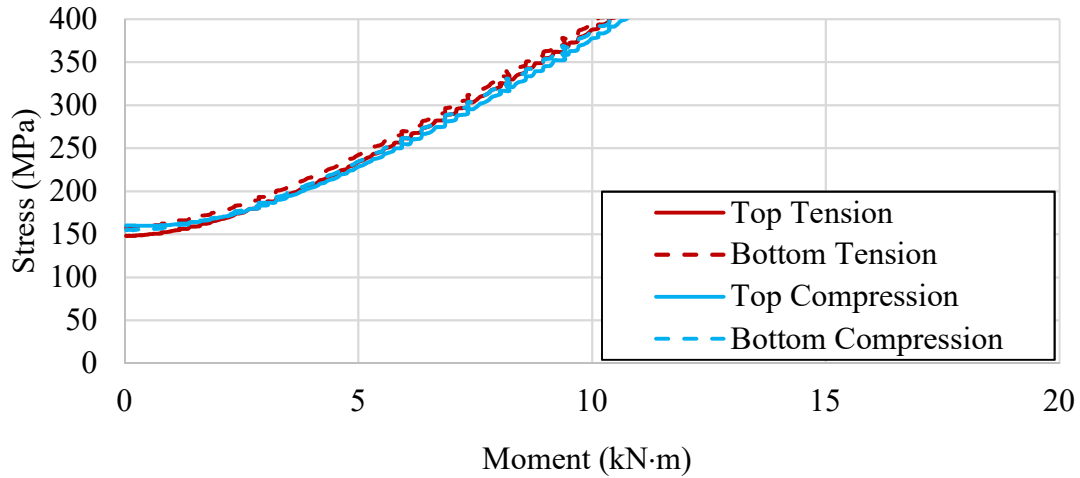
Figure B.7: von Mises Stress for Test SP1-2
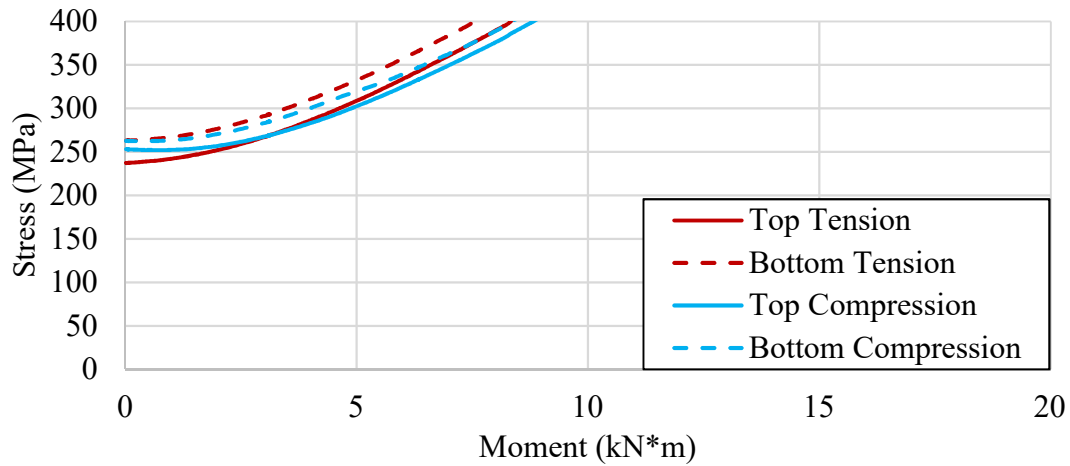
Figure B.8: von Mises Stress for Test SP1-3
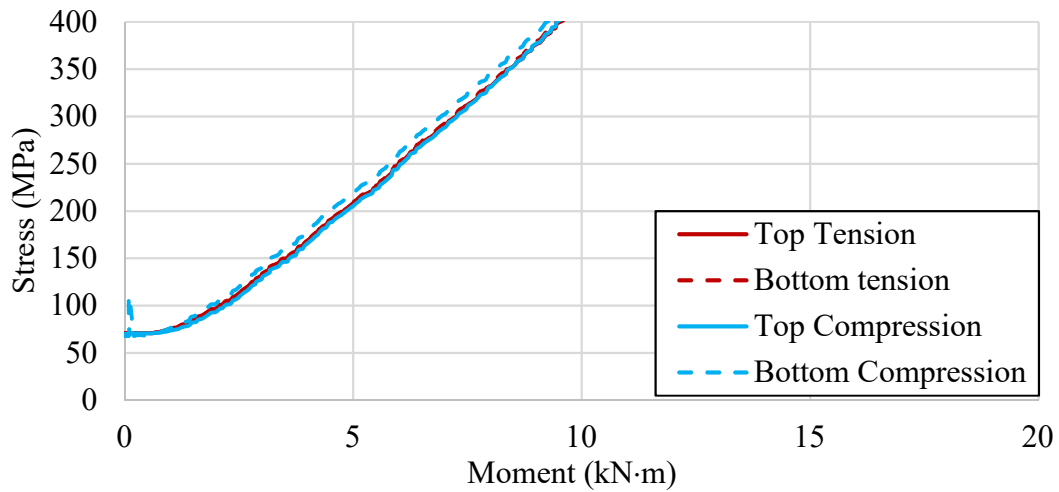
Figure B.9: von Mises Stress for Test SP2-1
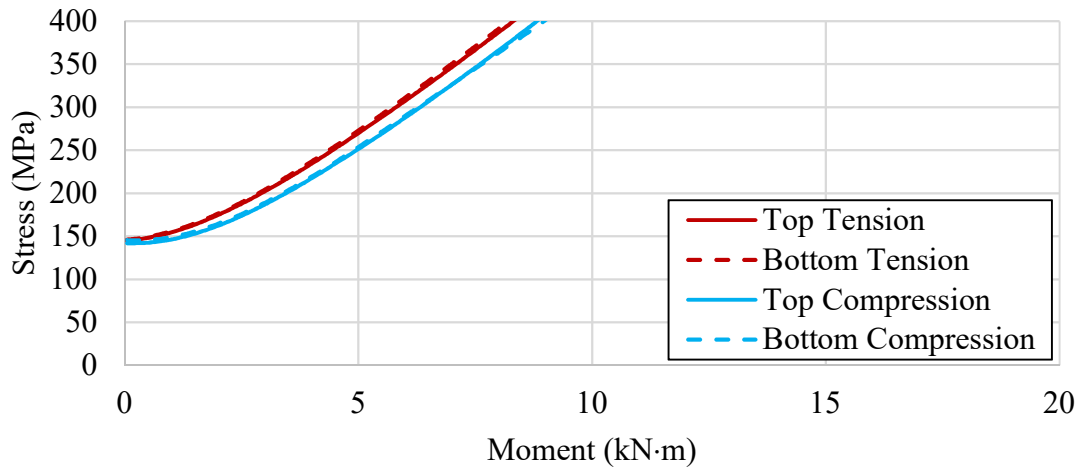
Figure B.10: von Mises Stress for Test SP2-2

Figure B.11: von Mises Stress for Test SP2-3

Figure B.12: von Mises Stress for Test SP3-1

Figure B.13: von Mises Stress for Test SP3-2
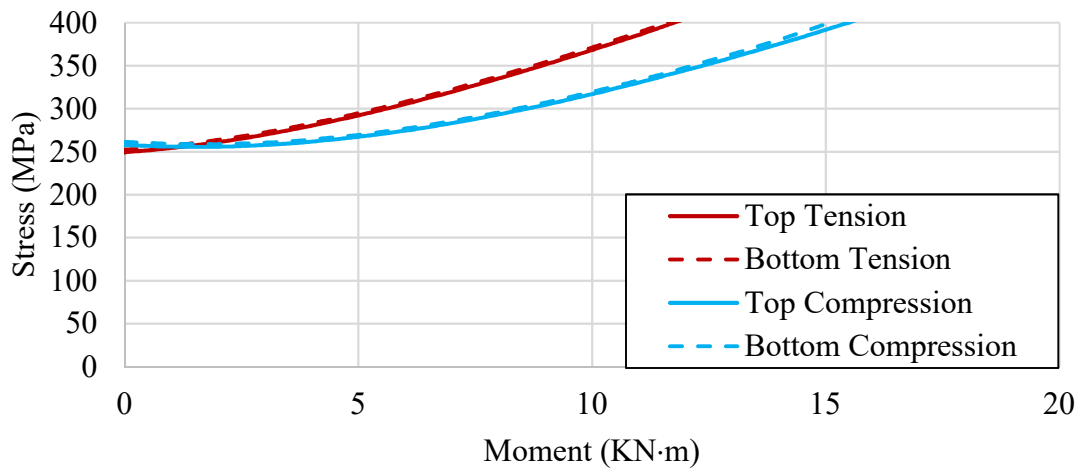
Figure B.14: von Mises Stress for Test SP3-3
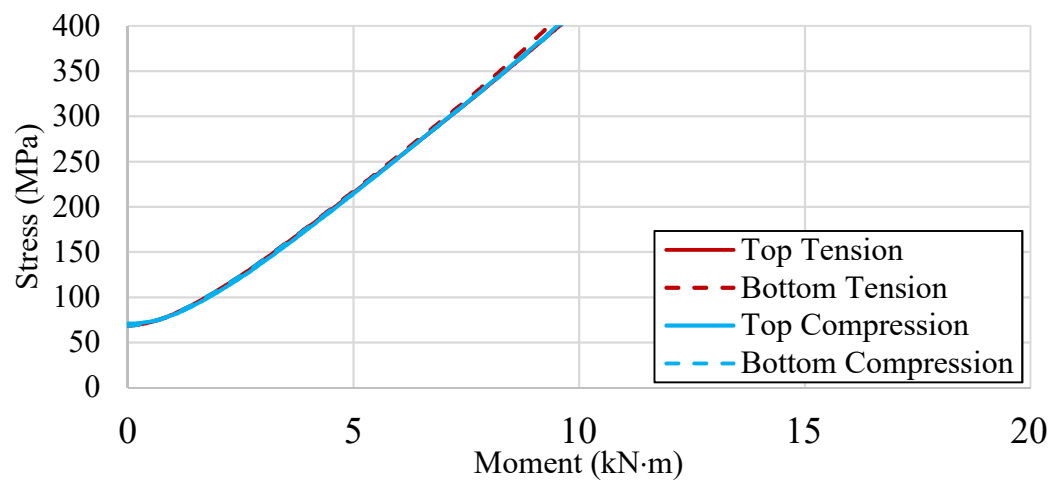
Figure B.15: von Mises Stress for Test SP4-1
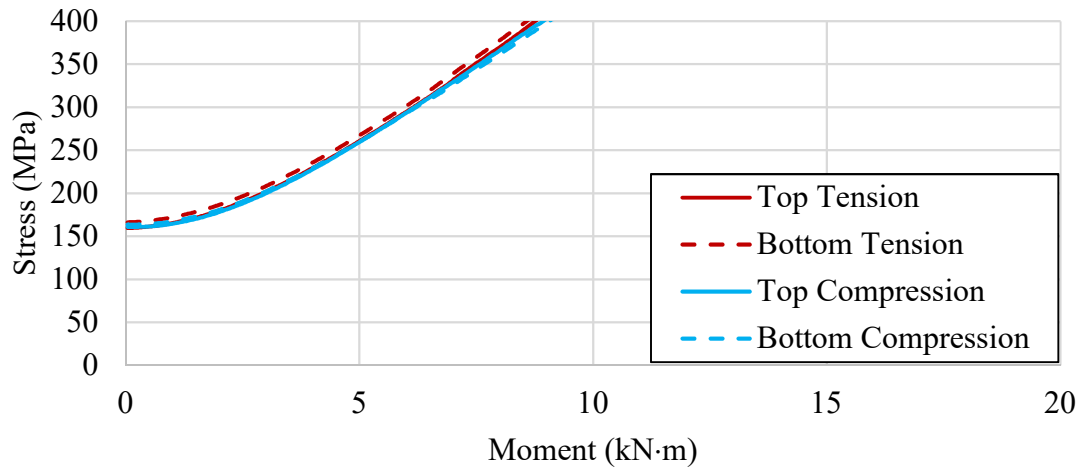
Figure B.16: von Mises Stress for Test SP4-2
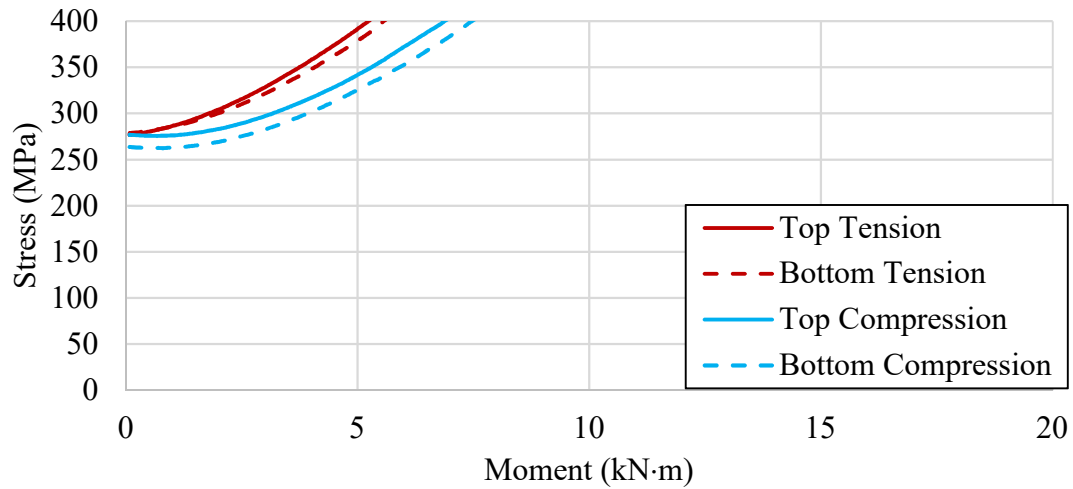
Figure B.17: von Mises Stress for Test SP4-3

Appendix C Parametric Comparisons
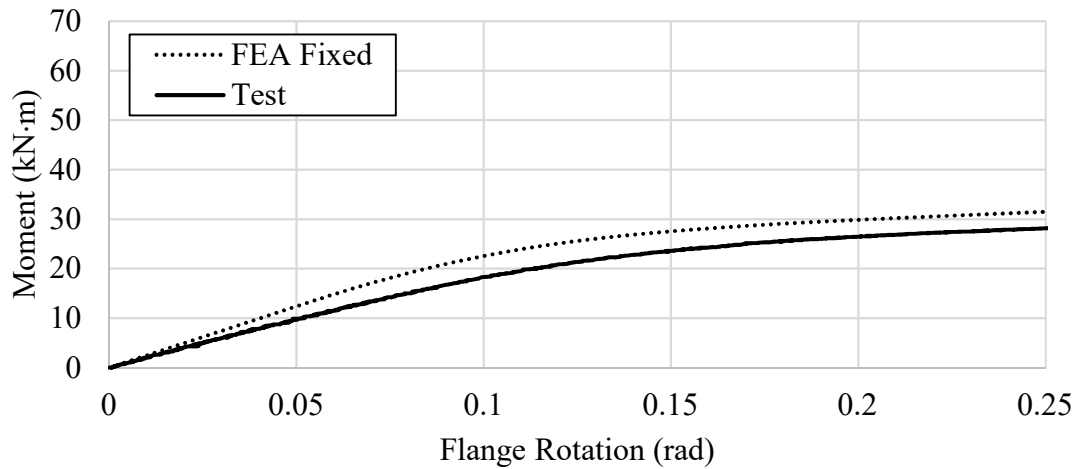
Figure C.1: Moment–Rotation Response for SP1-2
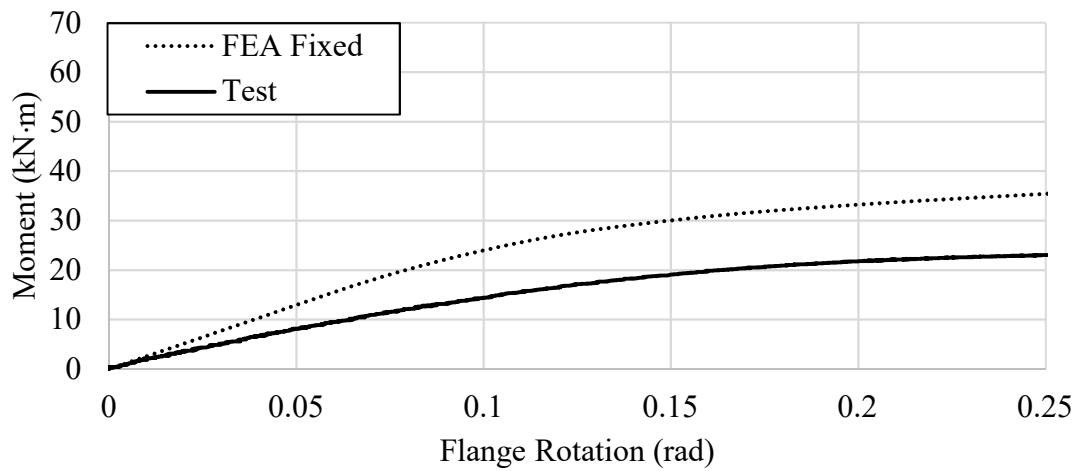
Figure C.2: Moment–Rotation Response for SP1-3
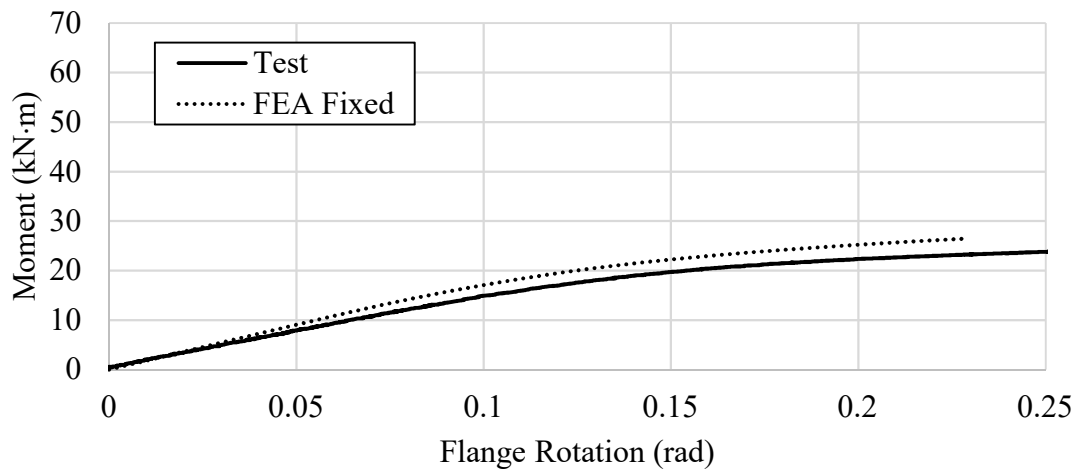
Figure C.3: Moment–Rotation Response for SP2-2
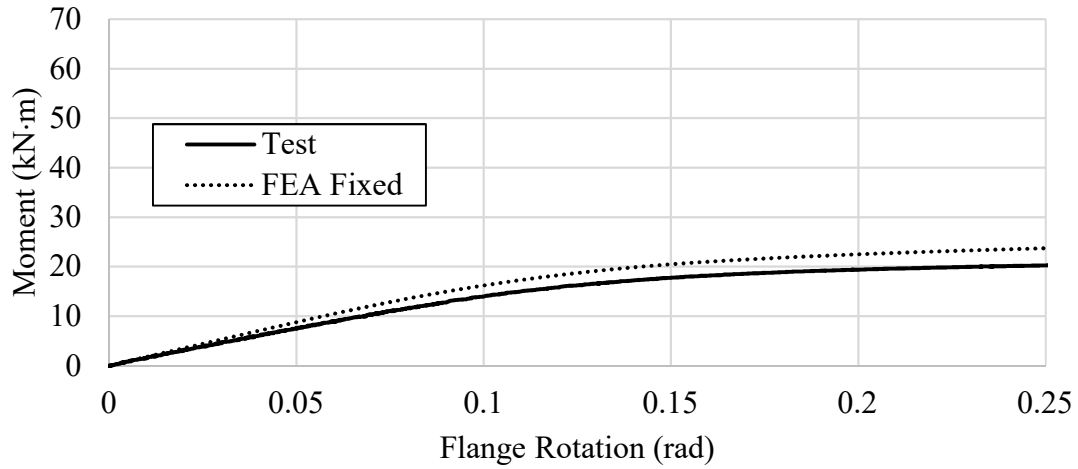
Figure C.4: Moment–Rotation Response for SP2-3
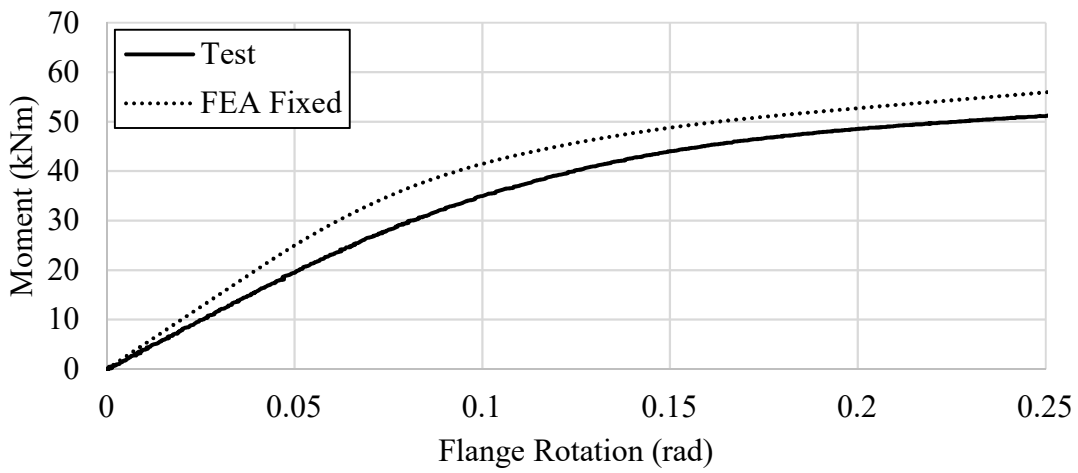
Figure C.5: Moment–Rotation Response for SP3-2
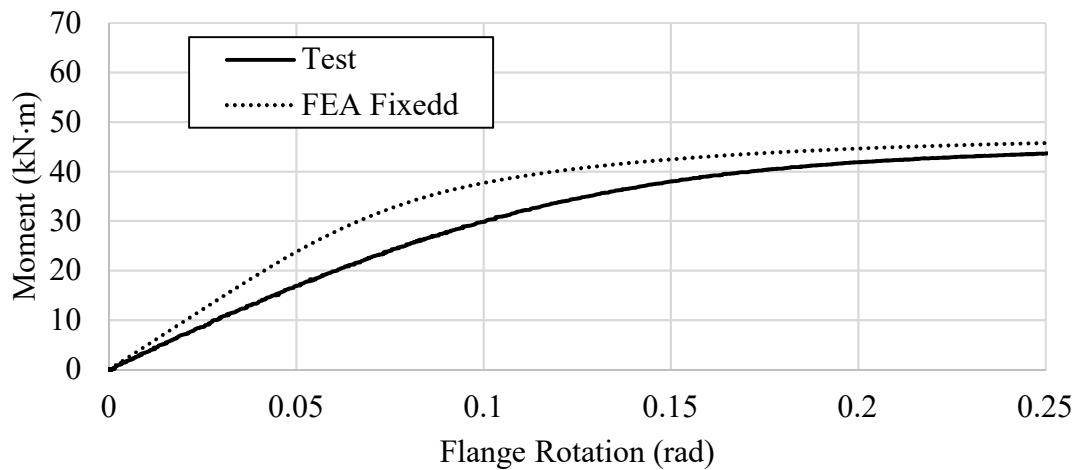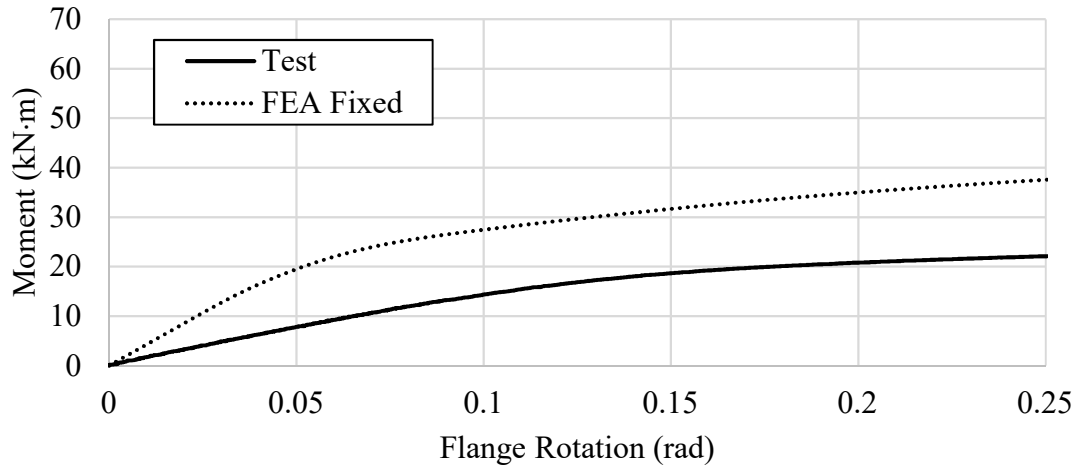

Figure C.6: Moment–Rotation Response for SP3-3

Figure C.7: Moment–Rotation Response for SP4-2

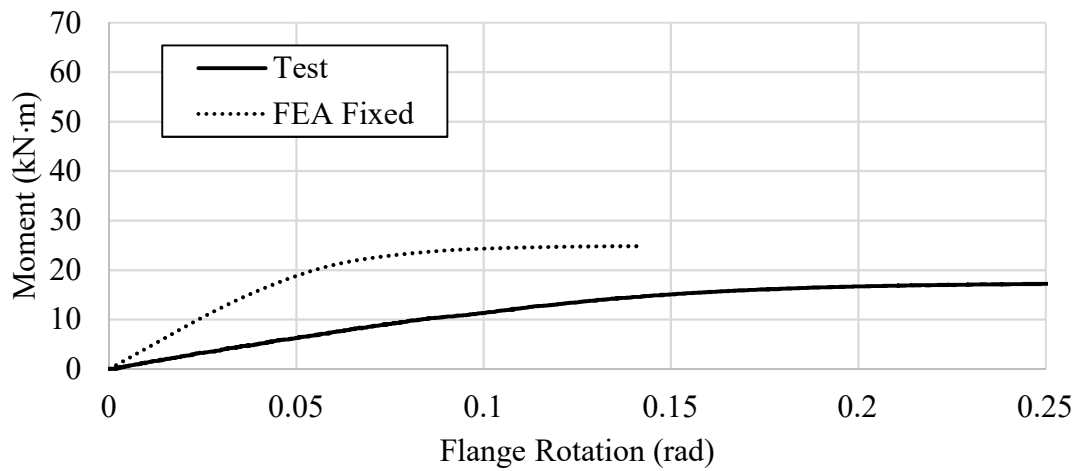

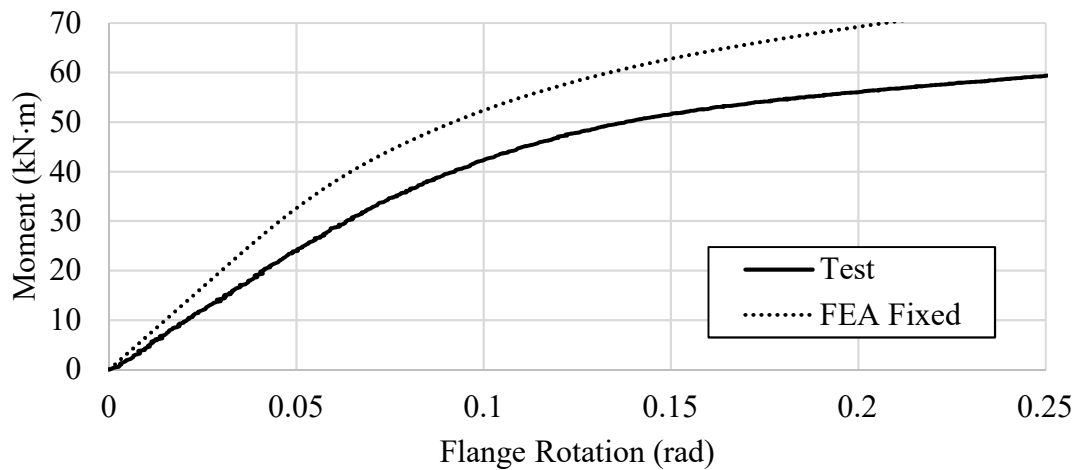Figure C.8: Moment–Rotation Response for SP4-3
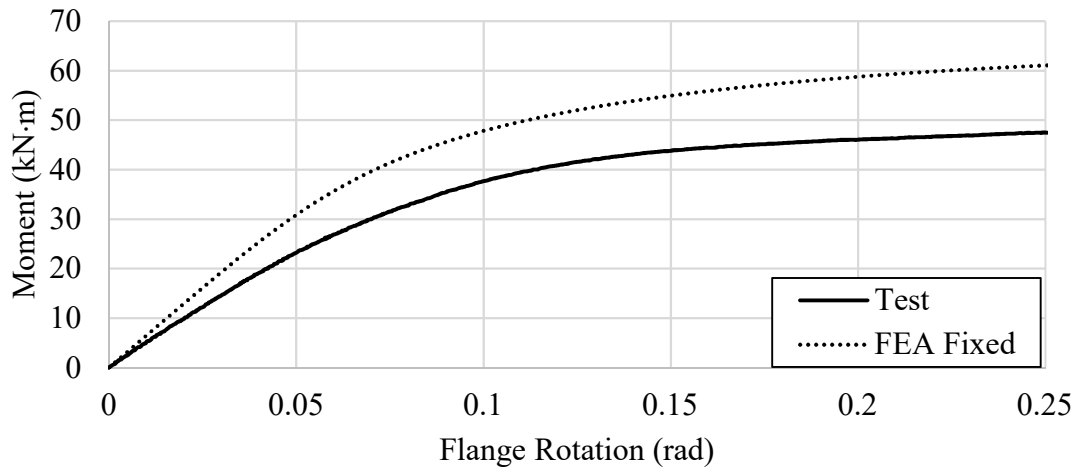

Figure C.9: Moment–Rotation Response for SP5-2

Figure C.10: Moment–Rotation Response for SP5-3